UNIVERSITÀ
DEGLI STUDI
FIRENZE

INTERNATIONAL DOCTORATE IN ATOMIC AND MOLECULAR PHOTONICS

CICLO XXXI
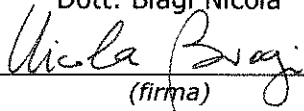
COORDINATORE Prof. Francesco Saverio Cataliotti

QUANTUM MANIPULATION OF MULTI-PHOTON STATES OF LIGHT
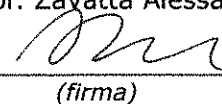
Settore Scientifico Disciplinare FIS/03
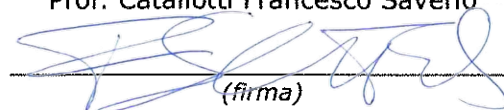
Dottorando
Dott. Biagi Nicola

(firma)

Tutore
Prof. Zavatta Alessandro

(firma)

Coordinatore
Prof. Cataliotti Francesco Saverio

(firma)

Anni 2015/2018

Contents

Introduction

Since the early times of Quantum Mechanics it was clear that this new theory represented a breaking-point with the past deterministic interpretation of the physics world. If, from one side, this theory was able to unify concepts that were considered antithetical before its introduction, e.g. the wave-particle duality of matter and light, on the other hand it destroyed many pillars of our classical interpretation of nature. The concept of measurement itself, which represents the main instrument for physicists to investigate the world, was completely revolutionized, going from a completely deterministic interpretation to a probabilistic one, intrinsic in Born's rule [1]. In this thesis, instead of dealing with different philosophical implications of Quantum Mechanics, I will present the opportunities it opens to develop new technologies. After countless observations, which have confirmed its validity, Quantum Mechanics has begun to enter our daily life. The laser, widely used in medicine and in many other fields, as well as the transistors that are the building blocks of smartphones and computers that we use daily, are just some examples of devices whose working principles can be explained only in terms of this theory. In recent years, it has been understood that the features of Quantum Mechanics can be used to overcome the limits imposed by the classical interpretation of nature, especially in the field of metrology, computation and communication. On the other hand, some operations easily implemented with classical systems are prohibited in the quantum domain, such as measuring a system without perturbing it or perfect cloning of units of information. The possible application of the so-called *quantum revolution* in technology is indeed a highly debated point, which is why basic research in the field of quantum mechanics is still necessary today.

Light is a very powerful tool to investigate the validity of the predictions of Quantum Mechanics. Thanks to devices and methods available today, scientists are now able to generate, manipulate and characterize the states of a light system at the quantum level, making *quantum state engineering* a promising field of investigation. In this context, the study of phenomena predicted by Quantum Mechanics can be carried out in

three steps: the preparation of a system in a particular initial state, mathematically described by a Hilbert space; its manipulation, for which the basic instruments are described in this thesis; and finally, its characterization. For the last point, the Homodyne Detection technique, described in Section 1.3.2, is a powerful tool. In the context of state manipulation, many works [2][3][4] have underlined the extremely interesting possibilities opened by the ability to experimentally deal with the fundamental operations of annihilation ($\hat{a}$) and creation ($\hat{a}^{\dagger}$) of single quanta of light. Over the years, more and more sophisticated techniques to implement quantum operations based on the experimental realization of the annihilation and creation operators have been developed. For example, by exploiting the concept of *quantum superposition*, it has been possible to experimentally test the commutation relations between these operators [5], which are at the origin of the quantum nature of light. Following the lines of this experiment, I present in Chapter 2 a technique able to emulate, on weak quantum states of light, the same transformation caused by a strong optical nonlinearity, the *Kerr effect*, which can not be obtained with the materials available today.

Any discussion about the revolutions introduced by Quantum Mechanics can not be concluded without talking of entanglement. This is one of the most controversial concepts introduced by this theory, on which the most brilliant minds of the last century have been debating for a long time. At the beginning of Chapter 3, a general review of this phenomenon is presented. Again, light is a perfect tool to investigate it. At the end of this thesis I will show how, by delocalizing the addition operation among different light systems, it is possible to generate entanglement among them even if they are initially in a macroscopic non-entangled state. This experiment represents a new tool to study, in the macroscopic domain, phenomena up to now confined in the microscopic regime. From this work we can also understand what are the limits of the available technologies to when we deal with quantum effects.

Chapter 1

Brief Introduction to Experimental Quantum Optics

The aim of this work is to study some fundamental aspects of Quantum Mechanics, and in this first chapter I will provide a description of the main building blocks using an experimental perspective. I will introduce various formalisms need to describe quantum operators, quantum states and quantum measurements.

1.1 Quantum Operators

Quantum mechanics is based on the concept that two systems can exchange only discrete quantities of energy. For example, an excited atom can jump to a lower energy state yielding a quantum of energy to the surrounding environment. From the mathematical point of view, the destruction and the generation of energy quanta are described by the $\hat{a}$ and the $\hat{a}^\dagger$ operators. Their action on a number state $(|n\rangle)$[1] is described by the relations:

$$
\begin{aligned}
\hat{a}\,|n\rangle &= \sqrt{n}\,|n-1\rangle \\
\hat{a}\,|0\rangle &= 0,
\end{aligned}
\tag{1.1}
$$

$$
\hat{a}^\dagger\,|n\rangle = \sqrt{n+1}\,|n+1\rangle
\tag{1.2}
$$

---

[1] The details of this kind of state are better explained in Section 1.2. Here it is sufficient to know that these vectors represent the eigenvectors of the hamiltonian describing the electromagnetic field quantized in vacuum [1].

and they obey the commutation rule:

$$\left[\hat{a}, \hat{a}^\dagger\right] = 1 \tag{1.3}$$

The relation (1.2) tells us that the creation operator $(\hat{a}^\dagger)$ acts on a system with no energy, the vacuum $(|0\rangle)$, creating a single quantum of energy in that system.

$$\hat{a}^\dagger |0\rangle = |1\rangle$$

For the destruction operator $(\hat{a})$ something similar is true. Its action on a system with exactly n quanta of excitation is to remove just one of them, leaving the system with $n-1$ energy quanta.

This PhD thesis is focused on the study of the quantum properties of light systems, therefore, I will refer to the operators $\hat{a}^\dagger$ and $\hat{a}$ as the creators and the annihilators of *photons*, the energy quanta of the electromagnetic field.

The product $\hat{a}^\dagger \hat{a}$ is another important operator that will be widely used in this work. It is called *number operator* $(\hat{n})$ and it has a crucial role in the quantization of the electromagnetic field. For example, the Hamiltonian that describes the energy of a quantized electromagnetic field in vacuum can be written in the form[1]

$$\hat{H}_{free}^{e.m.} = \hbar\omega\left(\hat{n} + \frac{1}{2}\right), \tag{1.4}$$

where the frequency $\frac{\omega}{2\pi}$ defines the oscillation frequency of the field. The role of $\hat{n}$ is to count the number of quantized excitations, each of energy $\hbar\omega$, of the electromagnetic field i.e. the *number of photons*. Applying $\hat{n}$ on an eigenvector of the hamiltonian (1.4) we have[2]:

$$\hat{n} |n\rangle = n |n\rangle . \tag{1.5}$$

Equation (1.5) tells us that this operator leaves the number state unchanged, giving us the number of photons (n) that characterize it. I will show in the next session that the knowledge of the photon number statistics of an optical state gives interesting information about it. From this point of view, it is important to notice that the operator $\hat{n}$ is hermitian, so it can be measured [6]. In Section 1.3 I will describe two detectors sensitive to the photon number carried by a state of light.

Other observables, very useful to characterize the quantum properties of a light state,

---

[2]That is the definition of the *number states*.

are the *quadratures of the electric field*, defined as a combination of the annihilation
and creation operators:

$$\hat{X}_{\theta_M} = \frac{\hat{a}\, e^{-i\theta_M} + \hat{a}^\dagger\, e^{i\theta_M}}{2}, \tag{1.6}$$

where θ_M is the measurement phase. Its meaning will be clarified in Section 1.3.2, where
I will give a detailed description of an instrument, the *Homodyne Detector*, capable to
measure the quadrature values of a quantum state of light for all the possible measure-
ment phases. Commonly, we call the quadrature measured at phase $\theta_M = 0$ as the $\hat{X}$
quadrature, while setting the phase equal to $\frac{\pi}{2}$ we measure the $\hat{Y}$ quadrature. This
convention is related to the mathematical form used to describe the monochromatic
electric field in terms of measurable operators

$$\hat{E}(\theta_M) = \left(\frac{1}{2}\hat{a}e^{-i\theta_M} + \frac{1}{2}\hat{a}^\dagger e^{i\theta_M} \right) = \left(\hat{X}\cos(\theta_M) + \hat{Y}\sin(\theta_M) \right), \tag{1.7}$$

where I used the convention $\sqrt{\frac{2\hbar\omega}{\varepsilon_0 V}} = 1$. In Section 1.4 I will describe an algorithm
capable to give a complete description of an optical state starting from the results of a
set of quadrature measurements performed on it, for different settings of θ_M.

1.2 Quantum States

In Section 1.1 an important concept starts to emerge. In quantum optics the role of the
operators is to perform an action onto a system. It doesn't matter if it is a measurement
or some other operation that manipulates a certain system, the operators contain the
"rules of the game": they specify the action, the results depending on the particular
state the system is in. In this section I will present a brief description of the main
optical states used in this work.

1.2.1 Number states

The *number states* (or *Fock States*) are defined as the eigenstates of the *number operator*
$\hat{n}$, as anticipated in Equation (1.5). They can be obtained by repeated application of
the creation operator on a system initially in the vacuum state.

$$|n\rangle = \frac{1}{\sqrt{n!}}\hat{a}_1^\dagger \otimes \hat{a}_2^\dagger \otimes \cdots \otimes \hat{a}_n^\dagger |0\rangle \tag{1.8}$$

As an immediate consequence of this definition, we have that there is no uncertainty on the number of photons in such a state, so:

$$\left(\Delta\hat{n}\right)^2 = \langle n|\,\hat{n}^2\,|n\rangle - \langle n|\,\hat{n}\,|n\rangle^2 = 0 \tag{1.9}$$

From Equation (1.4) it is also simple to understand their natural predisposition to describe fixed energy states of the electromagnetic field. Indeed, it is possible to prove that they are an orthonormal and complete base on which to describe the solutions of the Schrödinger equation for the electromagnetic field [1].

$$\langle n|m\rangle = \delta_{n,m} \rightarrow Orthonormality\ condition$$
$$\sum_{n=0}^{\infty} |n\rangle\,\langle n| = \hat{I} \rightarrow Completeness\ condition \tag{1.10}$$

Despite their easy mathematical description, they are non-trivial to produce in the laboratory. A lot of efforts have been spent on their generation in the past decades. The main procedures to produce them involve quantum dots[7][8], cold atoms [9][10], molecules [11][12], Nitrogen Vacancy Centers in diamonds [13][14] and nonlinear optical processes, such as *Parametric Down Conversion*, that will be described later in this work.

Let's focus now on the properties of this kind of states in relation to the electromagnetic field. Using the first part of Equation (1.7) and a few other relations presented in the previous section, it is possible to derive two important properties of measurements of electric field performed on a number state.

Their mean value is always zero

$$\langle n|\,\hat{E}(\theta_M)\,|n\rangle = 0, \tag{1.11}$$

and their variance grows as the photon number increases

$$\begin{aligned}
\left(\Delta\hat{E}(\theta_M)\right)^2 &= \langle n|\,\hat{E}^2(\theta_M)\,|n\rangle - \langle n|\,\hat{E}(\theta_M)\,|n\rangle^2 \\
&= \frac{1}{2}(n + \frac{1}{2}).
\end{aligned} \tag{1.12}$$

The mean value and the variance of the electric field for an n-photon Fock state do not depend on the phase at which the measurement is performed. This is the reason of the failure of any attempt to describe them in an effective noise theory. The measurement technique that I will describe in Section 1.3.2 allows to realize electric field measurements, therefore, in view of this, it is useful to show the probability distribution of

such measurements once performed on a given state. For the Fock state case, we can
calculate these quantities in terms of the measurable quadrature operators as:

$$
\begin{aligned}
P_n(X_{\theta_M}) = |\langle X_{\theta_M}|n\rangle|^2 &= \left|\left(\frac{2}{\pi}\right)^{\frac{1}{4}} e^{-in\theta_M} \frac{H_n(\sqrt{2}X_{\theta_M})}{\sqrt{2^n n!}} e^{-X_{\theta_M}^2}\right|^2 \\
&= \left(\frac{2}{\pi}\right)^{\frac{1}{2}} \frac{|H_n(\sqrt{2}X_{\theta_M})|^2}{2^n n!} e^{-2X_{\theta_M}^2},
\end{aligned}
\tag{1.13}
$$

where $\langle X_{\theta_M}|n\rangle$ are the wave functions for the quantum harmonic oscillator expressed
on the quadrature base, and $H_n(\sqrt{2}X_{\theta_M})$ are the Hermite polynomials. The quadrature
probability distributions for zero, one, and two-photon states are reported in Figure
1.1. From these plots it is evident that if we perform repeated quadrature measure-
ments on a Fock state, the outcome distribution will remain unchanged regardless the
measurement's reference phase.
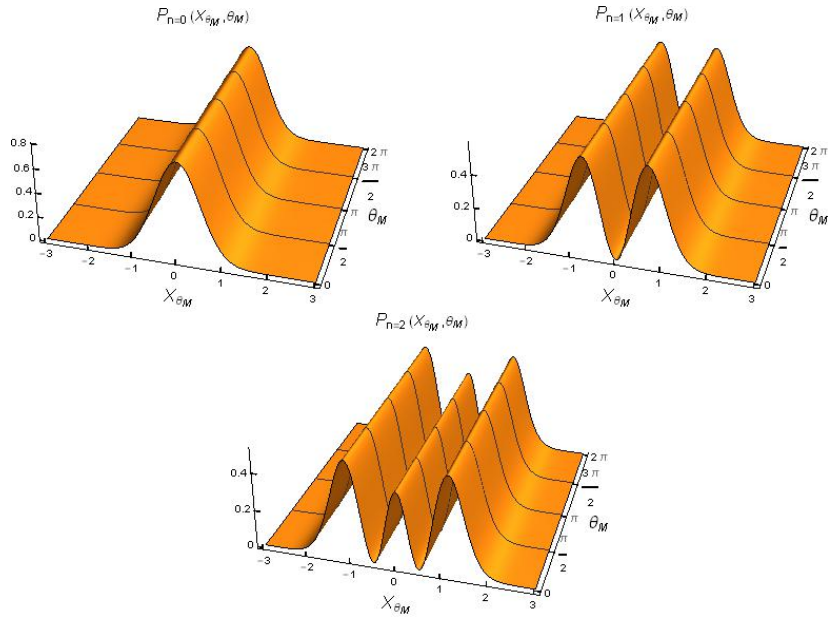
Figure 1.1: Probability distributions of the $\hat{X}_{\theta_M}$ quadrature for $|0\rangle$, $|1\rangle$ and $|2\rangle$ Fock
states, for different measurement phases θ_M. These probability distributions are in-
variant when changing θ_M.

Before describing another important class of states, let us focus our attention on a
particular number state, the *vacuum* state ($|0\rangle$). This is the minimum-energy state of
the electromagnetic field and, from Equation (1.4), we can see that this energy is larger
than zero. In quantum optics this is explained by considering the presence, everywhere
in the space, of a randomly fluctuating electric field [15]. We will see that, using an

homodyne detector, it is possible to measure also this field. Let us now look at what happens if we perform a simultaneous measurement of the two quadratures $\hat{X}$ and $\hat{Y}$ on the vacuum state. Because of the phase invariance of the quadrature distribution, the two measurements have the same uncertainty. From Equation (1.12) we can calculate the variance of the joint measurement as:

$$(\Delta \hat{X})^2 (\Delta \hat{Y})^2 = \frac{1}{16} \tag{1.14}$$

This is the minimum value allowed by the Heisenberg uncertainty principle, obtained by the standard procedure [16], considering that, for the commutator between $\hat{X}$ and $\hat{Y}$, stands

$$[\hat{X}, \hat{Y}] = \frac{i}{2}. \tag{1.15}$$

States that satisfy Equation (1.14) are called *minimum uncertainty states*.

1.2.2 Coherent states

This important class of states, introduced by Glauber in 1963 [17], is defined as the eigenstates of the annihilation operator:

$$\hat{a}\ket{\alpha} = \alpha \ket{\alpha} \qquad\qquad \alpha \in \mathbb{C} \qquad\qquad \alpha = |\alpha| e^{i\theta_{co}} \tag{1.16}$$

where the eighenvalue α is a complex number that defines the amplitude $|\alpha|$ and the phase θ_{co} of the state. They can be expressed in the number state base as:

$$\ket{\alpha} = e^{-\frac{1}{2}|\alpha|^2} \sum_{n=0}^{\infty} \frac{\alpha^n}{\sqrt{n!}} \ket{n}, \tag{1.17}$$

and recalling the expression of $\ket{n}$ (Equation (1.8)) as:

$$\ket{\alpha} = e^{-\frac{1}{2}|\alpha|^2} \sum_{n=0}^{\infty} \frac{(\alpha \hat{a}^\dagger)^n}{n!} \ket{0} = e^{(\alpha \hat{a}^\dagger - \frac{1}{2}|\alpha|^2)} \ket{0}$$
$$= e^{(\alpha \hat{a}^\dagger - \alpha^* \hat{a})} \ket{0} = \hat{D}(\alpha) \ket{0}, \tag{1.18}$$

where we have defined the *Displacement Operator* as[3] $\hat{D}(\alpha) = e^{(\alpha \hat{a}^\dagger - \alpha^* \hat{a})}$. A deeper understanding of the action represented by this operator can be obtained by studying

---

[3] In this equation we have used the relation $e^{\hat{A}} e^{\hat{B}} = e^{\hat{A} + \hat{B} + \frac{1}{2}[\hat{A};\hat{B}]}$, that is valid in this case because the equations $\left[\hat{A}; \left[\hat{A}; \hat{B}\right]\right] = 0$ and $\left[\hat{B}; \left[\hat{A}; \hat{B}\right]\right] = 0$ are satisfied for the coherent state case.

the properties of the electric field of a coherent state. For the mean value of $\hat{E}(\theta_M)$ we
have:

$$
\begin{aligned}
\langle\alpha|\,\hat{E}(\theta_M)\,|\alpha\rangle &= \langle\alpha|\,\hat{a}e^{-i\theta_M} + \hat{a}^\dagger e^{i\theta_M}\,|\alpha\rangle \\
&= |\alpha|\cos(\theta_M),
\end{aligned}
\tag{1.19}
$$

where θ_M is the phase of the measurement. The variance of this operator has an
interesting property too:

$$
\langle\alpha|\left(\Delta\hat{E}(\theta_M)\right)^2|\alpha\rangle = \frac{1}{4}.
\tag{1.20}
$$

From these relations we can say that, applying the displacement operator to the vacuum
state of the electric field, we will shift the mean value of the results of a quadrature
measurement from zero to $|\alpha|\cos(\theta_M)$, maintaining its variance unchanged. This fact
classifies the coherent states as minimum uncertainty states, as the vacuum state.
Unlike the number states, two different coherent states are, in general, not orthogonal:

$$
\begin{aligned}
\langle\alpha|\beta\rangle &= e^{-\frac{|\beta|^2+|\alpha|^2}{2}}\sum_{n,m}\frac{(\alpha^*)^m\beta^n}{\sqrt{m!n!}}\langle n|m\rangle \\
&= e^{-\frac{|\beta|^2+|\alpha|^2}{2}}\sum_{n}\frac{(\alpha^*\beta)^n}{n!} \\
&= e^{-\frac{|\alpha-\beta|^2}{2}}.
\end{aligned}
\tag{1.21}
$$

They can be considered orthogonal only in the limit $|\alpha-\beta|\to\infty$.

Coherent states are very useful in quantum optics because they are the best approx-
imation of the ideal light state generated by a well-stabilized laser. Indeed, they are
easy to produce and they will be widely used in this work. Also in this case, the prob-
ability distribution for an electric field measurement is an important quantity to keep
in mind:

$$
P_\alpha(X_{\theta_M}) = \sqrt{\frac{2}{\pi}}e^{-2[X_{\theta_M}-|\alpha|cos(\theta_M)]^2}.
\tag{1.22}
$$

From Figure 1.2 the dependence of the quadrature distributions on the phase of the
measurement performed to obtain it is evident.

It is also useful to recall the photon number properties of this kind of states:

$$
\langle\hat{n}\rangle = \langle\alpha|\,\hat{n}\,|\alpha\rangle = \langle\alpha|\,\hat{a}^\dagger\hat{a}\,|\alpha\rangle = |\alpha|^2,
\tag{1.23}
$$
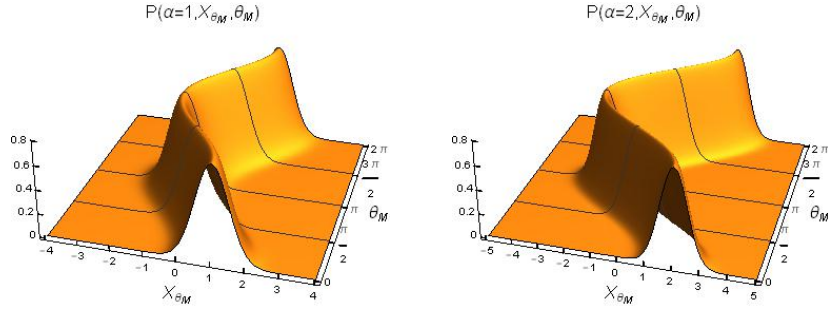
Figure 1.2: Probability distributions of the $\hat{X}_{\theta_M}$ quadrature for two different values of α and different measurement phases θ_M.

$$(\Delta\hat{n})^2 = \langle\alpha|\,\hat{n}^2\,|\alpha\rangle - \langle\alpha|\,\hat{n}\,|\alpha\rangle^2 = |\alpha|^2 = \langle\hat{n}\rangle. \tag{1.24}$$

Equations (1.23) and (1.24) are the first two moments of the photon number probability distribution for a coherent state, shown in Figure 1.3 for three values of α.
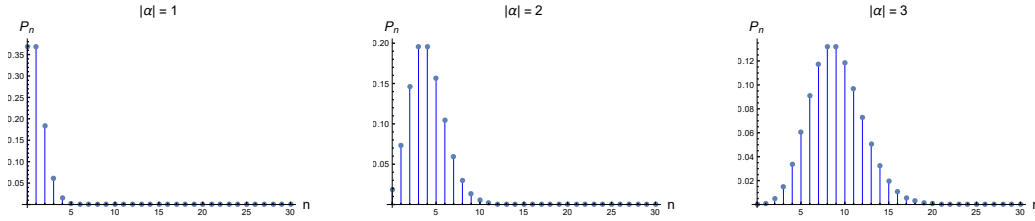
Figure 1.3: Photon number probability distributions for coherent states of different mean photon number ($\langle\hat{n}\rangle = |\alpha|^2$).

This is a peaked Poisson distribution for which the relative photon number (intensity) fluctuations decrease for increasing α

$$\frac{\Delta I}{\bar{I}} \propto \frac{\Delta\hat{n}}{\langle\hat{n}\rangle} = \frac{1}{\sqrt{\langle n\rangle}}. \tag{1.25}$$

This fact qualify the coherent states as "the most classical one among quantum states". Indeed, for a classical stable wave the intensity is a fixed quantity with no fluctuations, that is the limit case for coherent states of large α.

1.2.3 Pure States and Mixed States - The Density Operator Formalism

All classes of states described so far are called *pure states*. In general, a pure state can be written as the superposition of states that form a base of the electromagnetic radiation field ($\{|\psi_n\rangle\}$).

$$|\psi\rangle = |pure\ state\rangle = \sum_n c_n |\psi_n\rangle, \tag{1.26}$$

where c_n are complex amplitudes that define the probability to observe the state $|\psi_n\rangle$ ($p_n = |c_n|^2$), and also the relative phase of the component $|\psi_n\rangle$ respect to the overall phase of the superposition. However, not all the states of the electromagnetic field can be written as pure states. Imperfections in the generation apparatus, interactions with the external environment, or the will of the experimenter lead to a description of the light state only in terms of probability, where all the phase relations between the states are lost. This concept is introduced in quantum mechanics via the definition of the *density operator* ($\hat{\rho}$) and these states are called *statistical mixtures* [1]

$$\hat{\rho} = \sum_n p_n |\psi_n\rangle \langle\psi_n|. \tag{1.27}$$

Here p_n have a clear interpretation in term of probabilities, so we have:

$$\sum_n p_n = 1 \tag{1.28}$$

From the relation (1.28) we can see that, as a special case of this formalism, we can also describe the pure states. Indeed, if only one of the p_n (p_*) is different from zero, we have $p_* = 1$, so the resulting density matrix is

$$\hat{\rho}_* = |\psi_*\rangle \langle\psi_*|, \tag{1.29}$$

where $|\psi_*\rangle$ is a pure state of the base defined at the beginning of this section.
Describing the state of a system in terms of its density operator reveals its importance when we try to formalize the concept of expectation value of a measurement. In general, it is defined as the statistical mean of all the possible measurement outcomes. Let's say, for example, that the measurement is represented by the operator $\hat{O}$. The expectation value is:

$$\langle\hat{O}\rangle = \sum_n p_n \langle\psi_n| \hat{O} |\psi_n\rangle, \tag{1.30}$$

but if we introduce the generic complete base $\{|a_i\rangle\}^4$

$$
\begin{aligned}
\langle \hat{O} \rangle &= \sum_{n,i} p_n \langle \psi_n| \, \hat{O} \, |a_i\rangle \langle a_i|\psi_n\rangle = \\
&= \sum_{n,i} p_n \langle a_i|\psi_n\rangle \langle \psi_n| \, \hat{O} \, |a_i\rangle = \sum_i \langle a_i| \, \hat{\rho}\hat{O} \, |a_i\rangle = \\
&= Tr\left(\hat{\rho}\hat{O}\right),
\end{aligned}
\tag{1.31}
$$

that is equivalent to the Equation (1.30) but easier to manipulate in the case of a statistical mixture. If we calculate the expectation value of the identity operator ($\hat{I}$), we find the normalization condition of the density operator:

$$
Tr\left(\hat{\rho}\right) = \sum_{n,i} p_n \langle a_i|\psi_n\rangle\langle \psi_n|a_i\rangle = \sum_{n,i} p_n \langle \psi_n|a_i\rangle\langle a_i|\psi_n\rangle = \sum_n p_n = 1.
\tag{1.32}
$$

If this condition is not verified for a density operator it is not representing a physical system.

It is also important to notice that, recalling the form of the density operator in the case of a pure states (Equation (1.29)), we have:

$$
Tr\left(\hat{\rho}_{pure}^2\right) = Tr\left(\hat{\rho}_{pure}\right) = 1.
\tag{1.33}
$$

On the contrary, in the case of a mixed state, we have:

$$
\begin{aligned}
\hat{\rho}_{mix}^2 &= \sum_{n,m} p_n p_m |\psi_n\rangle \langle \psi_n|\psi_m\rangle \langle \psi_m| \ \Rightarrow \\
&\Rightarrow \ Tr\left(\hat{\rho}_{mix}^2\right) = \sum_{n,m,i} p_n p_m \langle a_i|\psi_n\rangle\langle \psi_n|\psi_m\rangle\langle \psi_m|a_i\rangle = \\
&= \sum_{n,m,i} p_n p_m \langle \psi_m|a_i\rangle\langle a_i|\psi_n\rangle\langle \psi_n|\psi_m\rangle = \sum_{n,m} p_n p_m \langle \psi_m|\psi_n\rangle\langle \psi_n|\psi_m\rangle = \\
&= \sum_{n,m} p_n p_m |\langle \psi_m|\psi_n\rangle|^2 = \sum_n p_n^2 \leq 1.
\end{aligned}
\tag{1.34}
$$

So $Tr(\hat{\rho}^2)$ can be defined as the *purity* of a state and used to discern a pure state from a statistical mixture. During this introduction to the density operator we made use of the base $\{|\psi_n\rangle\}$, over which $\hat{\rho}$ is diagonal[5], but, in general, it is not an orthonormal

---

[4] $\sum_i |a_i\rangle \langle a_i| = \hat{I}$

[5] Using this base indeed we have:

$$
\langle \psi_n| \, \hat{\rho} \, |\psi_n\rangle = p_n \quad \forall n
$$

$$
\langle \psi_n| \, \hat{\rho} \, |\psi_m\rangle = 0 \quad \forall n \neq m
$$

base. Switching to such a base ($\{|a_i\rangle\}$) the $\hat{\rho}$ operator has the form:

$$\hat{\rho} = \sum_n p_n \left|\psi_n\right\rangle \left\langle\psi_n\right| = \sum_{n,i,j} p_n \left|a_i\right\rangle \left\langle a_i|\psi_n\rangle\langle\psi_n|a_j\right\rangle \left\langle a_j\right| = \sum_{i,j} \rho_{ij} \left|a_i\right\rangle \left\langle a_j\right|$$

$$\rho_{ij} = \left\langle a_i\right| \hat{\rho} \left|a_j\right\rangle = \sum_{n,i,j} p_n \langle a_i|\psi_n\rangle\langle\psi_n|a_j\rangle, \tag{1.35}$$

where the diagonal elements ($\rho_{ii} = \sum_n p_n |\langle a_i|\psi_n\rangle|^2$) again tell us the probability to find the system in the base state $|a_i\rangle$. Instead, the off-diagonal elements are related to the correlations between the base states for the physical system represented by $\hat{\rho}$.

In conclusion, we can say that the *density operator* contains all the information about the state it represents. In the last section of this chapter I will show a technique to obtain the density matrix ρ_{ij} from a set of experimental measurements.

1.2.4 Distributed Modes - A more realistic formalism

The theory presented in the previous sections is the easiest way to explain the concepts of operator and state from the quantum optics point of view, but, in this form, it is often far from the real experimental situation. In several experiments the properties of the optical states are not simply described as in Section 1.2. Indeed, if we say that we have generated a single photon state, we are giving only a partial information. It could be very important to specify also the spectral band over which we have produced it, for example. Other important characteristics are its propagation direction, its temporal or spatial shape, polarization, and so on, depending on the type of experiment performed. All these features define the *mode* of the optical state. From a practical point of view it is useful to split the concept of optical mode into subsets, each of which refers to different features. In this thesis I will use the term *"spatial mode"* to indicate the spatial properties of an optical state, as well as *"spectral mode"*, *"temporal mode"*, etc. To mathematically formalize this concept we have to slightly modify some of the above definitions. The operator $\hat{a}^\dagger$ defined in Equation (1.2), for example, adds a single photon at a monochromatic frequency, with a single wave vector and so on. A more complete description of this operator is[6]:

$$\hat{a}^\dagger(\omega) = \int d\omega' \delta(\omega - \omega')\hat{a}^\dagger(\omega'), \tag{1.36}$$

where it is explicit that only one monochromatic frequency mode is involved. From this expression it is easy to generalize to an operator that generates single photons with

---

[6]For sake of simplicity I will consider only the spectral mode in the following explanation.

a wave-packet distribution of frequencies, as is very common for most of the devices used to produce them

$$\hat{a}_g^\dagger = \int d\omega g^*(\omega)\hat{a}^\dagger(\omega). \tag{1.37}$$

Here the notation is heavier than the one in Equation (1.2) but has to be interpreted as follows: $\hat{a}^\dagger(\omega)$ is the monochromatic creation operator already defined, $\hat{a}_g^\dagger$ is the operator that generates a single photon in a frequency wave-packet of shape defined by the complex mode function $g(\omega)$.

This formalism can alternatively be incorporated into the states instead of into the operators. For example, for the single photon state we will write

$$|1_g\rangle = \hat{a}_g^\dagger |0\rangle = \int d\omega g^*(\omega)\hat{a}^\dagger(\omega) |0\rangle = \int d\omega g^*(\omega) |1_\omega\rangle , \tag{1.38}$$

where the notation has the same meaning of Equation (1.37). This is useful for the calculations in which we don't want to introduce operators, but the mode properties have to be taken into consideration. For example, using this formalism, we can see that if two Fock states have equal number of photons, they can have a scalar product equal to zero if their modes (indicated here as spectral modes $g(\omega)$ and $f(\omega)$) are not matched to each other, in contrast with the definition (1.10).

$$\begin{aligned}
\langle 1_g | 1_f \rangle &= \int d\omega \langle 0| g(\omega)\hat{a}(\omega) \int d\omega' f^*(\omega')\hat{a}^\dagger(\omega') |0\rangle \\
&= \int d\omega d\omega' g(\omega) f^*(\omega') \langle 1_\omega | 1'_\omega \rangle \\
&= \int d\omega d\omega' g(\omega) f^*(\omega') \delta(\omega - \omega') \\
&= \int d\omega g(\omega) f^*(\omega).
\end{aligned} \tag{1.39}$$

This simple calculation is useful to understand the idea of the *mode overlap*, that will be further discussed in the context of homodyne detection.

The mode overlap can be used to take into account the frequency mismatch between two optical states, the spatial misalignment that frequently occurs while setting up an experiment, and other imperfections. In the rest of this work I will use the following convention for the normalization of the mode function $g(\omega)$:

$$\int d\omega |g(\omega)|^2 = 1, \tag{1.40}$$

in order to keep valid the commutation rule (1.3), as well as all the other relations regarding the number states.

We can use this formalism also for the coherent state case. The only change we have
to do is regarding the normalization of the mode profile:

$$\int d\omega |\alpha(\omega)|^2 = \langle \hat{n} \rangle, \tag{1.41}$$

where $\alpha(\omega)$ is the function describing the spectral mode occupied by the coherent state
and $\langle \hat{n} \rangle$ is its mean photon number. With this convention, the definition of coherent
state (Eq. (1.16)) is again valid:

$$\hat{a}(\omega) |\{\alpha\}\rangle = \alpha(\omega) |\{\alpha\}\rangle, \tag{1.42}$$

considering that the notation $|\{\alpha\}\rangle$ indicates a state distributed in the mode $\alpha(\omega)$. Or
alternatively,

$$\hat{a}_\alpha |\alpha\rangle = \alpha(\omega) |\alpha\rangle, \tag{1.43}$$

where we incorporated the mode properties in the annihilation operator instead of
into the state. The only change with respect to the theory presented in Section 1.2.2
regards the commutation rule between the creation and annihilation operator acting
on a coherent state:

$$\langle \alpha | \left[\hat{a}_\alpha, \hat{a}_\alpha^\dagger \right] |\alpha\rangle = \langle \{\alpha\} | \left[\hat{a}(\omega), \hat{a}^\dagger(\omega) \right] |\{\alpha\}\rangle = \langle \hat{n} \rangle. \tag{1.44}$$

This is a small price to pay because it leaves all the other coherent state relations
unchanged. The displacement operator in the distributed mode formalism has the
form:

$$\hat{D}(\{\alpha\}) = e^{\hat{a}_\alpha^\dagger - \hat{a}_\alpha}, \tag{1.45}$$

that acts on the vacuum generating a coherent state in the mode defined by $\alpha(\omega)$.
Also the relations regarding the electric field and the photon number operator remain
unchanged.

Summarizing, the distributed mode formalism is useful to take into account many
experimental aspects, but, if we are able to generate all the optical states in the same
mode, most of the results obtained in Section 1.1 and 1.2 remain valid[1].

1.3 Quantum Measurements

In this section I will link the observables, described from a theoretical point of view in
the first part of this work, to the real measuring devices used in the laboratory during
the experiments.

1.3.1   Photon Number Sensitive Detectors

As I showed in Section 1.2, the photon number distribution of an optical state can give us useful information to understand its nature. Currently, there is a class of detectors, called *photon number resolving* (PNR), able to detect the exact number of photons in an optical state. These detectors are commonly based on superconducting systems and thus require a complicate cooling apparatus. This technical difficulty makes the characterization of an optical state based on the photon number distribution not suitable for many experiments. A more "user-friendly" solution are the so called *single photon counting modules* (SPCM). They are devices capable to detect, with a given quantum efficiency η, the presence or the absence of photons, but not to discern their exact number. Practically, their output is the same (an electrical pulse or a "click") if one or n photons impact on the detector, however large n is, while no clicks are produced if 0 photons arrive on the detector. Due to this fact they are commonly called *on-off detectors*. This behavior can be mathematically formalized by two POVMs [18](Positive-Operator Valued Measure) $\hat{\Pi}_{on} = \hat{I} - |0\rangle\langle 0|$ and $\hat{\Pi}_{off} = \hat{I} - \hat{\Pi}_{on} = |0\rangle\langle 0|$, where $\hat{I}$ is the identity operator[19].

Using such a detector we can obtain the probability to observe more than one photon in a given optical state. By the definition of POVM, the probability to obtain a click from an on-off detector is $P_{click} = Tr\{\hat{\Pi}_{on}\hat{\rho}\}$, where $\hat{\rho}$ is the density operator describing the state we are measuring. Let's consider for example the state $\hat{\rho} = (a|0\rangle + b|1\rangle)(a^*\langle 0| + b^*\langle 1|)$, that is the superposition between the first two Fock states described in Section 1.2.1. The probability to observe a click is

$$
\begin{aligned}
P_{click} &= Tr\Big\{(\hat{I} - |0\rangle\langle 0|)(a|0\rangle + b|1\rangle)(a^*\langle 0| + b^*\langle 1|)\Big\} \\
&= \sum_{n=0}^{\infty} \langle n| \left(\hat{\rho} - |a|^2|0\rangle\langle 0| - ab^*|0\rangle\langle 1|\right) |n\rangle \\
&= |a|^2 + |b|^2 - |a|^2 = |b|^2,
\end{aligned}
\tag{1.46}
$$

that is the probability to observe the single photon component of the state used as example.

It should be emphasized that this type of detector can not be used to measure the photon number properties of an intense light beam, unless they are used in a multiplexed scheme. Since they are designed to detect the small amount of energy carried by a single photon, they have a high-gain amplification stage, which can be easily saturated (and even damaged) by a high-intensity light state.

1.3.2   Homodyne Detection

As already anticipated in the first Section, one of the most used techniques to obtain information about a quantum state of light is *Homodyne Detection* (HD). Using this technique it is possible to directly measure the electric field quadratures also for the very weak fields of a few-photon state. Unlike the device described in Section 1.3.1, this technique is sensitive to the phase of the optical state, so it is the perfect tool to investigate phase dependent quantum properties like *squeezing*, or to perform full reconstructions of the *density matrix* describing a quantum state [20]. In Figure 1.4 a scheme of this measurement apparatus is reported.
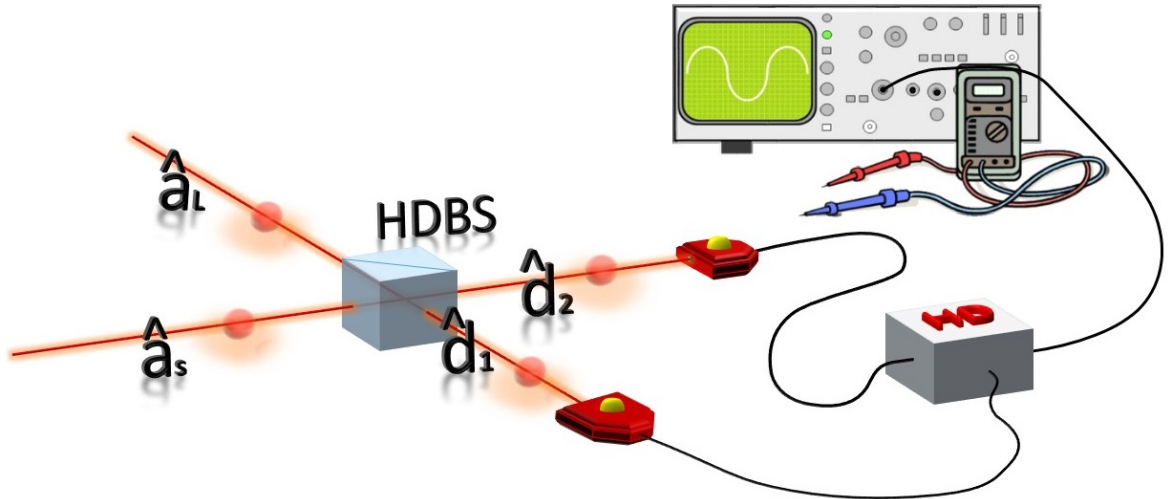

Figure 1.4: Schematic representation of the Homodyne Detection (HD) apparatus. The central element, denoted by the abbreviation HDBS, is a balanced beam-splitter, on which the reference beam called Local Oscillator ($\hat{a}_L$) is mixed with the unknown state ($\hat{a}_S$) under analysis. The outputs of this beam-splitter are detected by two photodiodes, then the difference between the two photocurrents is amplified and measured via an electronic system.

The state of the mode that we want to analyze, represented by the operator $\hat{a}_s$, is mixed in a *balanced* (50:50) beam-splitter with a strong coherent state, usually called *Local Oscillator* (LO). In this picture the LO beam is represented by the operator $\hat{a}_L$. The outputs of the beam-splitter are detected by two photodiodes, the difference between the two photocurrents is amplified and then measured. It is possible to show that the output of such a detector is proportional to the quadrature of the unknown quantum state of the signal mode, measured at the relative phase between the local oscillator

and the signal. Due to the central role played by the balanced beam splitter, I remind here the laws that describe its behaviour:

$$\hat{d}_1 = r \; \hat{a}_S + t \; \hat{a}_L$$
$$\hat{d}_2 = t \; \hat{a}_S + r \; \hat{a}_L. \tag{1.47}$$

For a 50:50 beam splitter the reflection and transmission coefficients can be written in the following form:

$$r = \frac{i}{\sqrt{2}} \qquad\qquad\qquad t = \frac{1}{\sqrt{2}}, \tag{1.48}$$

so the operator describing the Homodyne measure is:

$$\hat{H}_- \approx \hat{n}_2 - \hat{n}_1 = \hat{d}_2^\dagger \hat{d}_2 - \hat{d}_1^\dagger \hat{d}_1$$
$$= i\left[\hat{a}_S^\dagger \hat{a}_L - \hat{a}_L^\dagger \hat{a}_S\right]. \tag{1.49}$$

If we calculate the expectation value of this operator, considering a strong coherent state for the LO ($|\alpha_L\rangle$) and a generic state in the signal mode ($|\Psi_S\rangle$), we can see the link with the quadratures operator acting on the signal mode:

$$\langle\alpha_L, \Psi_S|\,\hat{H}_-\,|\Psi_S, \alpha_L\rangle = i\,\langle\alpha_L, \Psi_S|\,\left[\hat{a}_S^\dagger \hat{a}_L - \hat{a}_L^\dagger \hat{a}_S\right]|\Psi_S, \alpha_L\rangle$$
$$= 2\sqrt{n_L}\,\langle\Psi_S|\,\left[\frac{\hat{a}_S^\dagger e^{i(\theta_L + \frac{\pi}{2})} + \hat{a}_S e^{-i(\theta_L + \frac{\pi}{2})}}{2}\right]|\Psi_S\rangle \tag{1.50}$$
$$= 2\sqrt{n_L}\langle\hat{X}_S\rangle,$$

where we can recognize the definition of the quadrature operator acting on the signal ($\hat{X}_S$). The phase of the quadrature measurement (θ_M), defined in Equation 1.6, is strongly linked to the LO phase (θ_L), but, for a correct determination of this parameter, we have to take into account also the phase of the state on wich we are performing the measure. The quadrature value obtained with an Honodyne measurement is amplified by a factor ($\sqrt{n_L}$) proportional to the intensity (mean photon number) of the LO beam. As already mentioned, the concept of *mode* is of a great importance in the homodyne measurement. Thus, before going further with HD description, let us switch to the distributed mode formalism considering that the local oscillator is a strong coherent state $|\alpha_L\rangle$, occupying the mode $\alpha(\omega) = |\alpha(\omega)|e^{i\theta_L}$, and $|\psi_S\rangle$ is a generic quantum state distributed in the mode $\beta(\omega) = |\beta(\omega)|e^{i\theta_S}$, that in principle can be different from the LO one[7]. If we calculate the expectation value of the HD operator using this formalism,

---

[7]As in Section 1.2 I consider only the spectral mode of the optical states. A complete description of Homodyne measurement requires to take into account the whole mode function of both the LO and the unknown state $|\Psi_S\rangle$.

we have:

$$
\begin{aligned}
\langle \hat{H}_- \rangle &\approx \int d\omega \, \langle \psi_S | \, \langle \alpha_L | \, i \Big(\beta^*(\omega) \hat{a}_S^\dagger \alpha(\omega) \hat{a}_L - \alpha^*(\omega) \hat{a}_L^\dagger \beta(\omega) \hat{a}_S \Big) | \alpha_L \rangle \, | \psi_S \rangle \\
&= \int d\omega |\alpha_L(\omega)||\beta_S(\omega)| \, \langle \psi_S | \, \hat{a}_S^\dagger e^{i(\theta_L - \theta_S + \frac{\pi}{2})} + \hat{a}_S e^{-i(\theta_L - \theta_S + \frac{\pi}{2})} | \psi_S \rangle \\
&= 2\sqrt{n_L} \Big(\int d\omega |\tilde{\alpha}_L(\omega)||\beta_S(\omega)| \Big) \cdot \\
&\quad \cdot \langle \psi_S | \, \hat{X}_S \cos(\theta_L - \theta_S + \frac{\pi}{2}) + \hat{Y}_S \sin(\theta_L - \theta_S + \frac{\pi}{2}) | \psi_S \rangle \, .
\end{aligned}
\tag{1.51}
$$

In the last line I used the definition $\alpha(\omega) = \sqrt{n_L}\tilde{\alpha}(\omega)$, where $\alpha(\omega)$ is the coherent state mode profile defined in Equation (1.41), while $\tilde{\alpha}(\omega)$ is the profile normalized to 1. From Equation (1.51) the central role played by the local oscillator emerges. First of all, as already seen in Equation 1.50, the term $\sqrt{n_L}$ acts as an amplification factor. It is the square root of the local oscillator mean photon number, that, due to the large intensity of this beam, can amplify the small signal coming from the unknown quantum state $|\psi_S\rangle$ above the electronic noise of the measurement apparatus. The term $\int d\omega |\tilde{\alpha}_L(\omega)||\beta_S(\omega)|$ has a deep meaning too. It quantifies our ability to match the mode of the state that we want to measure to the mode of the LO, defining the so called *mode-matching efficiency*, $\eta_{mm} = (\int d\omega |\tilde{\alpha}_L(\omega)||\beta_S(\omega)|)^2$. A good mode matching is fundamental to perform homodyne detection, indeed, having fixed the mode of the local oscillator, if the state that we want to characterize is not in the same mode, this integral may drop to zero, despite the effect of the amplification. Practically, the local oscillator acts as a filter, defining the mode over which the homodyne measurement is performed. From Equation 1.51 we have also a precise definition of the measurement phase θ_M introduced in Equation (1.6): apart from the constant term $\frac{\pi}{2}$, this parameter is fixed by the relative phase between the LO and the state we are measuring, $\theta_M = \theta_L - \theta_S + \frac{\pi}{2}$. We can redefine the homodyne operator as:

$$
\begin{aligned}
\hat{H}_-(\theta_M) &\approx 2\sqrt{n_L}\sqrt{\eta_{mm}} \Big(\hat{X}_S \cos(\theta_L - \theta_S + \frac{\pi}{2}) + \hat{Y}_S \sin(\theta_L - \theta_S + \frac{\pi}{2}) \Big) \\
&= 2\sqrt{n_L} \hat{X}_S^{\tilde{\alpha}}(\theta_M),
\end{aligned}
\tag{1.52}
$$

where the operator $\hat{X}_S^{\tilde{\alpha}}(\theta_M)$ is the distributed mode version of the operator defined in Equation (1.6), that describes a quadrature measurement acting on the unknown quantum state $|\psi_S\rangle$, performed in the mode $\tilde{\alpha}$, at the measurement phase $\theta_M = \theta_L - \theta_S + \frac{\pi}{2}$.

Losses

The approximation symbol used in the Equation (1.52) reminds us that another step has to be done to keep into consideration all the technical details of this measurement. In the previous discussion an implicit assumption has been done: the two photodiodes are considered as perfect. In the real world, just a portion of the impinging photons are converted into electrons detectable via the acquisition system. This portion is usually quantified via the *quantum efficiency* η_{ph} parameter, that is usually given by the photodiodes manufacturers. A model that describes this phenomena makes use of an unbalanced beam splitter as shown in Figure 1.5.
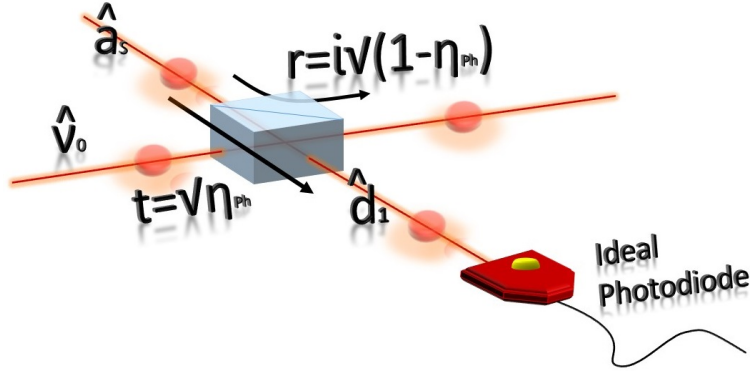
Figure 1.5: Graphical representation of the *loss beam-splitter model* used to take into account the non-unitary detection efficiency of a photodiode (η_{ph}). The signal under test ($\hat{a}_S$) is mixed with a portion of vacuum ($\hat{\nu}_0$) proportional to η_{ph}.

This model gives us the possibility to keep considering ideal detectors at the cost of placing, in front of them, a beam-splitter that mixes the state that we want to measure ($\hat{a}_S$) with a portion of vacuum ($\hat{\nu}_0$) proportional to the quantum efficiency of the detector. Introducing this model, the homodyne apparatus appears as shown in Figure 1.6.

Figure 1.6: Same apparatus of Figure 1.4 in which we implemented the *loss beam-splitter model* to consider the effect of non-perfect photodiodes.

We can now calculate the operator describing the homodyne measurement using the relations:
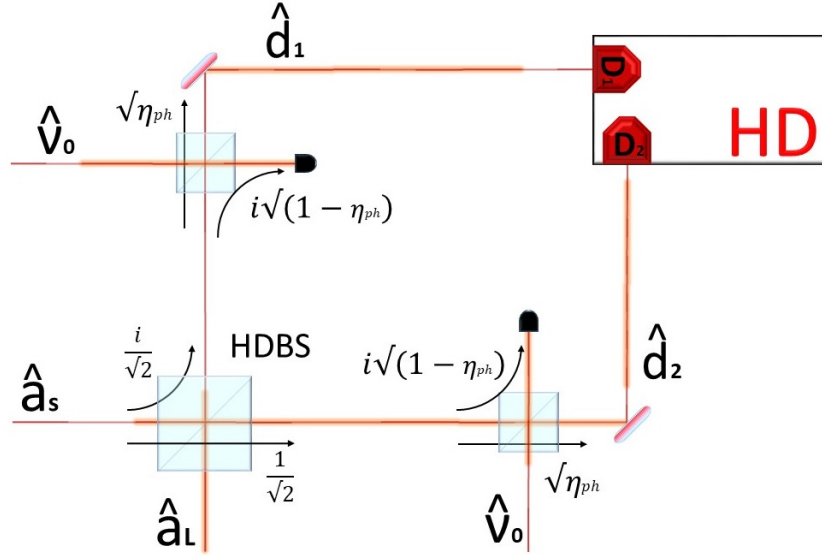
$$
\begin{aligned}
\hat{d}_1 &= \sqrt{\frac{\eta_{ph}}{2}}(i\hat{a}_S^\beta + \hat{a}_L^\alpha) + i\sqrt{1-\eta_{ph}}\,\hat{\nu}_0 \\
\hat{d}_2 &= \sqrt{\frac{\eta_{ph}}{2}}(\hat{a}_S^\beta + i\hat{a}_L^\alpha) + i\sqrt{1-\eta_{ph}}\,\hat{\nu}_0,
\end{aligned}
\tag{1.53}
$$

where $\hat{a}_S^\beta$ is the operator representing the signal state in the mode $\beta(\omega)$, $\hat{a}_L^\alpha$ represents the local oscillator beam in the mode $\alpha(\omega)$ and $\hat{\nu}_0$ is the operator acting on the vacuum mode added to consider the losses,

$$
\begin{aligned}
\hat{H}_-(\eta_{ph}, \eta_{mm}, \theta_M) &= \hat{d}_2^\dagger \hat{d}_2 - \hat{d}_1^\dagger \hat{d}_1 \\
&= i\eta_{ph}\left(\hat{a}_S^{\dagger\beta}\hat{a}_L^\alpha - \hat{a}_L^{\dagger\alpha}\hat{a}_S^\beta\right) + \\
&\quad + i\sqrt{\frac{\eta_{ph}(1-\eta_{ph})}{2}}\left((i+1)(\hat{a}_S^{\dagger\beta} - \hat{a}_L^{\dagger\alpha})\hat{\nu}_0 - (i-1)(\hat{a}_S^\beta - \hat{a}_L^\alpha)\hat{\nu}_0^\dagger\right).
\end{aligned}
\tag{1.54}
$$

The expectation value of this operator, calculated on the same signal and local oscillator state used in the ideal description made before, clarifies the effect of non-perfect photodiodes. Unlike the approximate version, in this case we also have to consider the

vacuum state on which the $\hat{\nu}_0$ operator acts, to find the correct expectation value:

$$
\begin{aligned}
\langle 0, \psi_S, \alpha_L | \, \hat{H}_-(\eta_{ph}, \eta_{mm}, \theta_M) \, | \alpha_L, \psi_S, 0 \rangle = \\
= i\eta_{ph} \int d\omega \, \langle \psi_S, \alpha_L | \, \beta^*(\omega)\hat{a}_S^\dagger \alpha(\omega)\hat{a}_L - \alpha^*(\omega)\hat{a}_L^\dagger \beta(\omega)\hat{a}_S \, | \alpha_L, \psi_S \rangle = \\
= 2\sqrt{n_L \eta_{ph}}\sqrt{\eta_{ph}\eta_{mm}} \, \langle \psi_S | \, \hat{X}_S \cos(\theta_L - \theta_S + \frac{\pi}{2}) + \hat{Y}_S \sin(\theta_L - \theta_S + \frac{\pi}{2}) \, | \psi_S \rangle \\
= 2\sqrt{n_L \eta_{ph}} \, \langle \psi_S | \, \hat{X}_S^{\tilde{\alpha}}(\theta_M) \, | \psi_S \rangle \,,
\end{aligned}
\tag{1.55}
$$

where $\hat{X}_S^{\tilde{\alpha}}(\theta_M)$ has the same meaning explained for Equation (1.52), incorporating also the effect of non-ideal photodiodes. In this calculation the second term of Equation (1.54) drops to zero due to the relations $\langle 0 | \hat{\nu}_0 | 0 \rangle = \langle 0 | \hat{\nu}_0^\dagger | 0 \rangle = 0$. From Equation (1.55) we see that non-ideal photodiodes acts in the same way of a non-perfect mode-matching, reducing both the signal and the LO amplitude. Starting from this point we can operatively summarize all the unavoidable losses in the experiment with an overall *detection efficiency* η_{det}. This factor will take into account, along with the mode matching and the photodiode efficiency, also the *electronic noise* due to an imperfect amplification and subtraction of the electronic signals (η_{el})[21] and *optical losses* caused by the unavoidable imperfections of the optical devices (η_{op})

$$
\eta_{det} = \eta_{mm} \cdot \eta_{ph} \cdot \eta_{el} \cdot \eta_{op}.
\tag{1.56}
$$

Going further in the HD description we can calculate the variance of the $\hat{H}_-$ operator to show that it is related to the electric field quadrature variance of the unknown state. For the sake of simplicity let's perform this calculation considering, as the unknown state, a Fock state in the mode $\beta(\omega)$, $|\psi_S\rangle = |n_S\rangle$

$$
\begin{aligned}
\left(\Delta \hat{H}_- \right)^2 = \langle 0, n_S, \alpha_L | \, \hat{H}_-^2 \, | \alpha_L, n_S, 0 \rangle - \langle 0, n_S, \alpha_L | \, \hat{H}_- \, | \alpha_L, n_S, 0 \rangle^2 \\
= 4n_L \eta_{ph}^2 \, \langle n_S | \, \frac{1}{2}(\eta_{mm} \hat{n}_S + \frac{1}{2}) \, | n_S \rangle + n_L \eta_{ph}(1 - \eta_{ph}).
\end{aligned}
\tag{1.57}
$$

The first term of Equation (1.57) is the variance of the electric field measured on a Fock state (see Eq. (1.12)), incorporating also the effect of a non perfect mode-matching. In the ideal case of perfect photodiodes and perfect mode-matching, the variance of the HD signal is exactly the variance of the electric field carried by the state we are measuring. If instead, we totally fail to mode-match the local oscillator to the signal mode ($\eta_{mm} = 0$), we have:

$$
\left(\Delta \hat{H}_- \right)^2_{shot} = n_L \eta_{ph},
\tag{1.58}
$$

that is the variance of the vacuum or the *shot noise* level of the detector. As we already saw in the ideal version of the HD described at the beginning of this section, the local oscillator can amplify also the lowest optical signal above the electric noise of the detector. This relation is often used to identify the linear region of an homodyne detector. The unbalancing of the homodyne beam-splitter, saturation of the photodiodes or differences between them can cause a distortion of the signal and so a deviation from the linearity predicted by Equation (1.58).

As last step in the description of Homodyne Detection technique I want to introduce a graphical tool useful to represent the results of a HD measurement, usually called *phasor diagram*. It consists of a 2D chart in which the two axes represent the real and imaginary components of the electric field ($\hat{X}$ and $\hat{Y}$) carried by the state. We already defined these quantities in Section 1.1 starting from the general definition of the quadrature operator

$$
\begin{aligned}
\hat{X}_{\theta_M} &= \frac{\hat{a}\, e^{-i\theta_M} + \hat{a}^\dagger\, e^{i\theta_M}}{2} \\
&= \frac{\hat{a}^\dagger + \hat{a}}{2}\cos(\theta_M) + i\frac{\hat{a}^\dagger - \hat{a}}{2}\sin(\theta_M) \\
&= \hat{X}\cos(\theta_M) + \hat{Y}\sin(\theta_M).
\end{aligned}
\tag{1.59}
$$

For example, an Homodyne measurement, performed at a local oscillator phase of θ_{LO} on a single mode coherent state of amplitude $|\alpha|$ and phase θ_α will be represented by the phasor diagram in Figure 1.7.
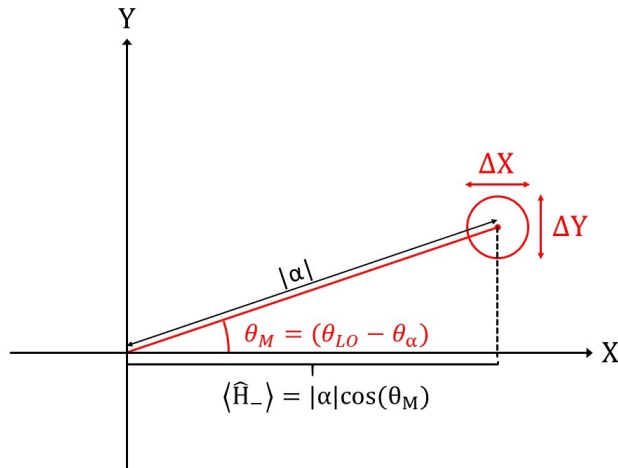

Figure 1.7: Phasor diagram representing an homodyne measurement performed on a coherent state.

The red line of length $|\alpha|$ represents the amplitude of the electric field of the coherent

state, while the circle centered at its extremity takes in account the unavoidable uncertainty of each quadrature measurement due to the Heisenberg uncertainty principle. By changing the measurement angle, the expectation value of the Homodyne measurement changes according to Equation (1.19) and it is represented by the projection of the red line on the X axes in the phasor diagram.

1.4   State Tomography

In this chapter we saw that different states have different properties (for example, the photon number and electric field distribution) and also that these properties can be collected in the density operator $\hat{\rho}$, which fully describes a quantum system. In the next two chapters, I will show different techniques to manipulate optical quantum states. I will explore a method to emulate strong nonlinear effects at the single photon level, or how to generate entanglement between macroscopic states. To get the proper conclusions from these experiments a complete characterization of the final states is needed. A procedure that allows one to know all the information about a system, without using a priori knowledge about it, is usually called *quantum state tomography*. In many cases, this procedure allows us to know the density matrix elements of the generated state expressed in a given basis[8]. As already seen in the previous section, homodyne detection is a powerful tool to measure the amplitude of the electric field carried by a quantum state, for different phases. In this section I will explain the procedure used during this work to reconstruct the density operator describing a given state from a set of homodyne measurements.

Maximum Likelihood Algorithm

This technique is based on the maximization of a functional widely used in mathematical statistic, called *Likelihood* ($\mathcal{L}$). $\mathcal{L}$ represents the expected probability of observing a given set of values $\{y_i\}$ as a consequence of a measurement on a system described by the density operator $\hat{\rho}$. Therefore, this procedure can be splitted into two distinct steps: the first is the collection of a proper data set, while the second is the maximization of $\mathcal{L}$ over all the possible $\hat{\rho}$. The set $\{y_i\}$ must be carefully selected because not all the observables give the complete information about the system. For example,

---

[8]To analyze the results of our experiments, we always express the reconstructed density matrices using the Fock basis.

measuring only the position of a particle in a harmonic potential is not sufficient to
determine its wave function, it will also be necessary to measure its momentum. To
fully characterize the states I will discuss in the rest of this work, I will use a set of
quadrature operators $\hat{X}_i(\theta_M)$, each measured for different values of θ_M.

For the second step, we make use of the work of Hradil et al. [22]. They demon-
strated, using variational methods, that the maximum value of the likelihood can be
found by solving the non linear system:

$$\hat{R}(\hat{\rho}, \boldsymbol{y})\hat{\rho}\hat{R}(\hat{\rho}, \boldsymbol{y}) = \hat{\rho}, \tag{1.60}$$

where

$$\hat{R}(\hat{\rho}, \boldsymbol{y}) = \sum_i f_i \frac{|y_i\rangle \langle y_i|}{\langle y_i| \hat{\rho} |y_i\rangle}, \tag{1.61}$$

and f_i is the frequency of the measured value y_i.
Assuming the initial condition $\hat{\rho}^{(0)} = \mathcal{N}\hat{I}$, where $\mathcal{N}$ is a normalization factor, the
system (1.60) can be iteratively solved according to the equation

$$\hat{R}(\hat{\rho}^{(n)}, \boldsymbol{y})\hat{\rho}^{(n)}\hat{R}(\hat{\rho}^{(n)}, \boldsymbol{y}) = \hat{\rho}^{(n+1)}. \tag{1.62}$$

Before entering into the details of this calculation, it is useful to better specify our data
set:

$$\{y_i\} = \{x_i(\theta_j), \theta_j\}, \tag{1.63}$$

that takes into account the fact that the same value of x_i can be measured for different
choices of θ. The POVM operators describing the measurements performed to obtain
the above data set have the form:

$$|y_i\rangle \langle y_i| = |x_i(\theta_j), \theta_j\rangle \langle x_i(\theta_j), \theta_j|. \tag{1.64}$$

To implement the abstract algorithm of Equation (1.62) it is necessary to project it
on a properly chosen basis and give a specific form to the operators $\hat{R}(\hat{\rho}^{(n)}, \boldsymbol{y})$ and $\hat{\rho}$.
Describing the *number states* I said that, in many cases, this is the simplest base to
perform calculation. This is one of those cases. Indeed, we have:

$$\begin{aligned}
\rho_{m,n}^{(n+1)} &= \langle m| \hat{R}(\hat{\rho}^{(n)}, \boldsymbol{y})\hat{\rho}^{(n)} \hat{R}(\hat{\rho}^{(n)}, \boldsymbol{y}) |n\rangle \\
&= \sum_{k,l} \langle m| \hat{R}(\hat{\rho}^{(n)}, \boldsymbol{y}) |k\rangle \, \rho_{k,l}^{(n)} \, \langle l| \hat{R}(\hat{\rho}^{(n)}, \boldsymbol{y}) |n\rangle \\
&= \sum_{k,l} R_{m,k}(\hat{\rho}^{(n)}, \boldsymbol{y})\rho_{k,l}^{(n)} R_{l,n}(\hat{\rho}^{(n)}, \boldsymbol{y}),
\end{aligned} \tag{1.65}$$

where $\rho_{m,n}^{(n+1)}$ is the matrix element of the density operator at the iteration $n+1$, the matrix element $R_{m,k}(\hat{\rho}^{(n)}, \boldsymbol{y})$ has now the form:

$$
\begin{aligned}
R_{m,k}(\hat{\rho}^{(n)}, \boldsymbol{y}) &= \langle m | \hat{R}(\hat{\rho}^{(n)}, \boldsymbol{y}) | k \rangle \\
&= \sum_{i,j} f_{i,j} \frac{\langle m | x_i(\theta_j), \theta_j \rangle \langle x_i(\theta_j), \theta_j | k \rangle}{\langle x_i(\theta_j), \theta_j | \hat{\rho}^{(n)} | x_i(\theta_j), \theta_j \rangle} \\
&= \sum_{i,j} f_{i,j} \frac{\langle m | x_i(\theta_j), \theta_j \rangle \langle x_i(\theta_j), \theta_j | k \rangle}{Pr^{(n)}(x_i(\theta_j), \theta_j)},
\end{aligned}
\tag{1.66}
$$

with $Pr^{(n)}(x_i(\theta_j), \theta_j)$ the probability to observe the quadrature x_i at the angle θ_j calculated from the density matrix at the nth iteration

$$
Pr^{(n)}(x_i(\theta_j), \theta_j) = \sum_{t,s} \langle x_i(\theta_j), \theta_j | t \rangle \rho_{t,s}^{(n)} \langle s | x_i(\theta_j), \theta_j \rangle.
\tag{1.67}
$$

Using these ingredients, and reminding that the projection of the quadrature eigenstates on the number states is:

$$
\langle n | x_i(\theta_j), \theta_j \rangle = e^{in\theta} \left(\frac{2}{\pi} \right)^{\frac{1}{4}} \frac{H_n(\sqrt{2}x)}{\sqrt{2^n n!}} e^{-x^2},
\tag{1.68}
$$

solving the system (1.62) is just a matter of computation, apart from an unavoidable assumption. To calculate the series (1.65), (1.66) and (1.67) they have to be truncated to a finite number of terms. This means that a proper assumption must be introduced to limit the Fock space[9]. Even if it is possible to do this without using any hypothesis on the state under analysis, in many experiments a certain amount of a priori knowledge is always present. The intensity of the measured state, some phase relation or the number of involved modes can help in this operation, thus simplifying the calculations. Another interesting feature of the *maximum likelihood algorithm* is the possibility to include the effects of non-unitary detection efficiency adopting the model of the *lossy beam-splitter* introduced for the homodyne detection. We have to reconsider the ingredients of the algorithm as transformed by an η transmissivity beam-splitter [23]. This adjustment allows the reconstruction of what has been really experimentally generated without considering the deterioration due to a non-perfect observation.

---

[9]It is the mathematical space on which the number states are described.

Chapter 2

Single-Mode State Manipulation

In the previous chapter, I described the features of the main quantum optics operators. Among these operators the most fundamental two are, of course, $\hat{a}$ and $\hat{a}^\dagger$. They have been analyzed in detail, considering also their *distributed mode* version to give a description more suitable for their practical realization. In this chapter I will discuss the techniques used during my PhD to experimentally implement the annihilation and the creation operators and superpositions of those on the same mode. Both of them share a fundamental aspect: they are based on a probabilistic approach. In contrast to an *on-demand* realization in which the wanted operation is realized at a specific moment, decided by the experimenter, in the probabilistic implementation the operation is randomly applied to the input state. Due to the ignorance about the application or not of the operation, this approach seems more suitable to produce, not the wanted operation $(\hat{O})$, but a mixture between it and the identity operator $(\hat{I})$, which is the mathematical way to say that "nothing happened". To overcome this problem, in the probabilistic implementation we make use of a second mode, usually called *ancillary mode*. Making a properly chosen measurement on the ancillary mode, it is possible to *herald*[1] the successful application of the operator $\hat{O}$, erasing the contribution of $\hat{I}$. So we can represent the tools used to experimentally realize $\hat{a}$ and $\hat{a}^\dagger$ as a machine with two inputs and two outputs. Two of them, labeled with 1, will be used to describe the *signal* before and after the operation, while the other two (labeled with a 2) will describe the ancillary mode. We can mathematically formalize this idea using two

---

[1] We usually refer to this type of approach as *heralded (or conditional) implementation* or *measurement induced* operation.

unitary operators with the form

$$\hat{U}_{\{sub,add\}} = e^{i\gamma \hat{J}(\hat{a}_1,\hat{a}_2,\hat{a}_1^\dagger,\hat{a}_2^\dagger)}, \tag{2.1}$$

where $\hat{J}(\hat{a}_1,\hat{a}_2,\hat{a}_1^\dagger,\hat{a}_2^\dagger)$ is the hermitian operator that generates the wanted transformation. For the annihilation case we should use

$$\hat{J}_{sub}(\hat{a}_1,\hat{a}_2,\hat{a}_1^\dagger,\hat{a}_2^\dagger) = \hat{a}_1\hat{a}_2^\dagger + \hat{a}_1^\dagger\hat{a}_2, \tag{2.2}$$

while in the addition case

$$\hat{J}_{add}(\hat{a}_1,\hat{a}_2,\hat{a}_1^\dagger,\hat{a}_2^\dagger) = \hat{a}_1^\dagger\hat{a}_2^\dagger + \hat{a}_1\hat{a}_2. \tag{2.3}$$

The operator (2.1) can be the starting point to implement the creation and the annihilation operators only in the case of a very low success probability. Indeed (2.1) leads to the desired operator only at the first order of approximation respect to the parameter γ, that, at this abstract level of description, can be only linked to the strength of the coupling between the modes 1 and 2. As I said, this probabilistic approach can not works if the ancillary mode is not properly detected[2]. So we have to consider as fundamental part of the machine used to realized a desired operation also the heralding system that measures the mode 2. To better understand this method let's focus on the annihilation operator case, considering that at this general level the same considerations stand for the creation operator. Taking $\gamma \approx 0$ we can write:

$$\begin{aligned}\hat{U}_{sub}|\psi\rangle_1|0\rangle_2 &= \mathcal{N}\{\left[\hat{I} + i\gamma\left(\hat{a}_1\hat{a}_2^\dagger + \hat{a}_1^\dagger\hat{a}_2\right) + \mathcal{O}(\gamma^2)\right]|\psi\rangle_1|0\rangle_2\} \\ &\approx \mathcal{N}\{|\psi\rangle_1|0\rangle_2 + i\gamma\hat{a}_1|\psi\rangle_1|1\rangle_2\},\end{aligned} \tag{2.4}$$

that represents, for the signal mode, the superposition between the initial state and the same state after the application of the annihilation operator, with probability γ^2. Looking at the whole state of Equation (2.4), composed by the signal and the ancillary modes, we can see that, when the $\hat{a}_1$ operator acts on the input state, there is a single photon in the mode 2, while for the unmodified part this mode remains in the vacuum state. So the detection of a single photon in the mode 2 will let us know when the operation has been performed. If we place an SPCM along the ancilla path, we can remove the unmodified component by observing the signal mode only in coincidence with a click from the detector[3],

$$\mathcal{N}\{|\psi\rangle_1|0\rangle_2 + i\gamma\hat{a}_1|\psi\rangle_1|1\rangle_2\} \xrightarrow[\hat{I}_2 - |0\rangle_2\langle 0|]{heralding} i\gamma\hat{a}_1|\psi\rangle_1. \tag{2.5}$$

---

[2]This can be easily understood thinking to the fact that the operator 2.1 is unitary, while the operators that we want to implement ($\hat{a}$ and $\hat{a}^\dagger$) are not.

[3]See Section 1.3.1 for more details.

It doesn't matter how small the success probability is, every time the operation is performed it is announced by the detection of a single photon in the ancillary mode. Of course, neglecting the higher order terms in the expansion of $\hat{U}_{sub}$ (Eq. (2.4)) leads to unavoidable errors. The faithful implementation of the annihilation operator using this technique requires that the probability (γ^4) to perform the operation $(\hat{a}_1)^2 \, |\psi\rangle_1$ is negligible respect to γ^2. Thus, it is clear that the γ parameter must be chosen as the best compromise between this request and the necessity to keep experimentally acceptable success probabilities.

2.1 Experimental Realization of Single Photon Subtraction

The single photon subtraction operation has been fundamental for the realization of important experiments during the years, like Schrodinger's cat state generation [24], enhanced quantum metrology [25] and fundamental tests [26][5]. The idea at the base of its implementation is simple: the subtraction of a single photon from a traveling optical state can be seen as a controlled loss. In this scenario, the $\hat{a}$ operator can be realized using a low-reflectivity beam-splitter. Indeed, the operator that obeys the relations (1.47) has exactly the form that we are looking for

$$\hat{U}_{sub} = \hat{U}_{BS} = e^{i\gamma(\hat{a}_1\hat{a}_2^\dagger + \hat{a}_1^\dagger\hat{a}_2)}. \tag{2.6}$$

It is possible to better see it if we look at what happens injecting a single photon in an arm of a beam-splitter as described by the relation used in the previous chapter,

compared to the application of the operator $\hat{U}_{BS}$ on the same state:

Chapter 1 Description

$$|1\rangle_1 |0\rangle_2 = \hat{a}_1^\dagger |0\rangle_1 |0\rangle_2 \xrightarrow[Equations\,(1.47)]{BS} \left(t\hat{a}_1^\dagger + r\hat{a}_2^\dagger\right) |0\rangle_1 |0\rangle_2$$

$$= t |1\rangle_1 |0\rangle_2 + r |0\rangle_1 |1\rangle_2 .$$

Application of $\hat{U}_{BS}$

$$\hat{U}_{BS} |1\rangle_1 |0\rangle_2 = \hat{U}_{BS} \hat{a}_1^\dagger |0\rangle_1 |0\rangle_2$$

$$= \hat{U}_{BS} \hat{a}_1^\dagger \hat{U}_{BS}^\dagger \hat{U}_{BS} |0\rangle_1 |0\rangle_2$$

$$= \left(\hat{a}_1^\dagger \cos(\gamma) + i\hat{a}_2^\dagger \sin(\gamma)\right) |0\rangle_1 |0\rangle_2$$

$$= \cos(\gamma) |1\rangle_1 |0\rangle_2 + i \sin(\gamma) |0\rangle_1 |1\rangle_2 ,$$

where I used the property of $\hat{U}_{BS}$ to be unitary ($\hat{U}_{BS}\hat{U}_{BS}^\dagger = 1$), and the relation $\hat{U}_{BS} |0\rangle_1 |0\rangle_2 = |0\rangle_1 |0\rangle_2$, that means that a two mode vacuum state remains unchanged after passing through a beam-splitter. From these relations we can see that, if we consider $t = \cos(\gamma)$ and $r = i\sin(\gamma)$, the operator $\hat{U}_{BS}$ actually describes the behavior of a beam-splitter. They are also telling us that, if we look at the signal mode after the beam-splitter, in most cases, with the probability $\cos^2(\gamma)$, the injected state remains unchanged[4], while, with the probability $\sin^2(\gamma)$, a photon is removed from the signal mode with the generation of a photon in the ancillary one. At this point, the strong link between the physical meaning of the parameter γ and the strategy used to practically implement the desired operation ($\hat{a}$) is more clear. In the experimental implementation of the annihilation operator using a low-reflectivity beam-splitter we have $\gamma = \arccos(t)$, that shows the link between the abstract γ and the more practical reflectivity of the beam-splitter (t). This implementation of the $\hat{a}$ operator has been used in many interesting works until now [2]. In Figure 2.1 a schematic picture of the setup used to realize this idea is reported.

In this representation we used the two spatial modes of the beam-splitter, one for the *signal* and the other for the *ancilla*, but, from the experimental point of view, it could not be the best choice. Indeed it implies that the two optical states travel along different paths, suffering from different losses and phase fluctuations. In some cases, a better way to realize the $\hat{a}$ operator is making use of the polarization degrees of freedom

---

[4]You have to remember that, for a low-reflectivity beam-splitter γ is small, so $\cos^2(\gamma) \approx 1$.
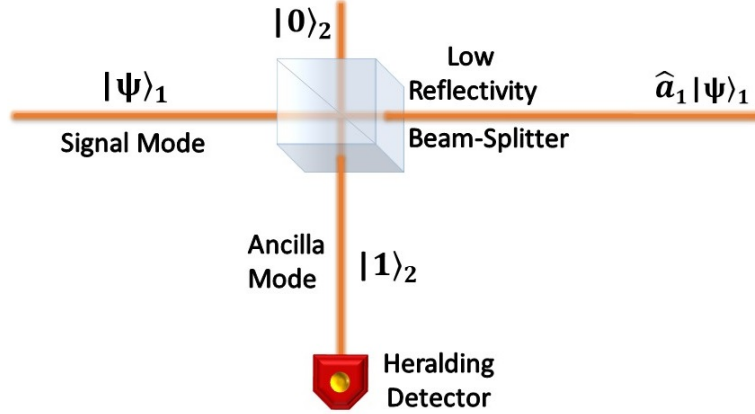
Figure 2.1: Schematic view of the heralded single photon subtraction scheme.

of the light states, with the help of a few polarization sensitive devices. In this type of implementation, the role of the spatial modes is now played by the two orthogonal polarization components of the traveling wave, that we will call *horizontal* and *vertical*. For example, we could consider the signal mode as the portion of an optical beam with horizontal polarization, while the vertically polarized part as the ancilla mode. To obtain the same effects seen using the spatial degrees of freedom, we need an optical device that mixes the two modes, like the beam-splitter. Its analog for the polarization encoding is the *half-wave-plate* (HWP). This optical device is a foil of a birefringent material cut with a proper thickness such that a delay of π is inferred between the *extraordinary* (*ordinary*) and *ordinary* (*extraordinary*) polarization components, for a fixed wavelength. This means that a linear polarization going through the plate will be rotated of an angle γ when the ordinary axis of the birefringent crystal is rotated of an angle $\frac{\gamma}{2}$ with respect to the input polarization direction[5]. Such a device is the analogous of a beam-splitter, indeed its input/output relations have the form:

$$\begin{pmatrix} \hat{a}_H^{out} \\ \hat{a}_V^{out} \end{pmatrix} = \begin{pmatrix} c_{HH} & c_{HV} \\ c_{VH} & c_{VV} \end{pmatrix} \begin{pmatrix} \hat{a}_H^{in} \\ \hat{a}_V^{in} \end{pmatrix}, \tag{2.7}$$

that, considering $c_{HH} = c_{VV} = \cos(\gamma)$ and $c_{HV} = c_{VH} = i\sin(\gamma)$, with the particle number conservation law $\hat{n}_H^{in} + \hat{n}_V^{in} = \hat{n}_H^{out} + \hat{n}_V^{out}$, are formally identical to the beam-splitter ones. In this case, the small success probability, required to consider valid the relation (2.4), can be obtained with small rotations of the signal mode polarization with respect to the ordinary axis of the HWP [27]. For example, by setting this angle

---

[5]Look at Appendix A for the details about the birefringence effect.

to 5 degrees, from the Malus' law we find a success probability of $\approx 3\%$, which is the one typically used for most of our experimental implementations. In these conditions, a photon from the polarization mode of the signal is transferred to the one of the ancilla. However, both the modes share the same spatio-temporal profile, experiencing the same drifts or vibrations of any optical element, enabling for a particularly stable and compensation free implementation of $\hat{a}$. The last step, also required in the polarization based realization of $\hat{a}$, is the detection of the ancillary photon. To do this, we need to spatially separate the two polarization modes. This can be achieved by using another birefringent device, a *polarizing beam-splitter* (PBS). This device can be considered as a normal beam-splitter despite the fact that the transmission and reflection coefficients depend on the polarization of the incoming beam. Using a PBS it is possible to totally transmit a polarization component, i.e. the horizontal polarization with respect to the PBS axes, while the other one is totally reflected. In this way, the two modes travel separately only at the end of the experimental scheme, the signal towards the characterization apparatus and the ancilla toward the heralding detector. As remarked in the previous chapter, to allow the treatment of the annihilation operator in the single mode picture we have to perform the operation in the same mode of the signal. To achieve this condition, the SPCM used to herald the operation has been coupled to the target beam by means of a single mode fiber. The spatial propagation mode of the fiber has thus been matched to the spatial mode of the target state by using a system composed of two lenses, resulting in an efficiency of $\approx 80\%$ of fiber-coupled photons. In Figure 2.2 is reported a schematic view of the setup just described.
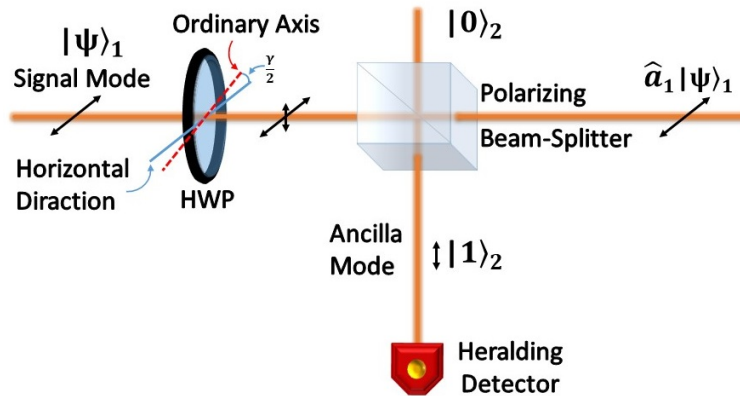

Figure 2.2: Schematic view of the heralded single photon subtraction scheme based on the polarization degrees of freedom of the light.

For all the experiments described in this work I used a mode-locked Ti:sapphire laser emitting $1.5\,ps$ long pulses at $786\,nm$, with a repetition rate of $80\,MHz$. Considering also that the SPCM used for the heralding has a detection efficiency of $\approx 60\%$, we can expect a success rate for the annihilation operation of $\approx LaserRepetionRate \cdot SubtractionProbability \cdot FiberCouplingEfficiency \cdot SPCMEfficiency \approx 1.1MHz$, if at list one photon per pulse is present at the input.

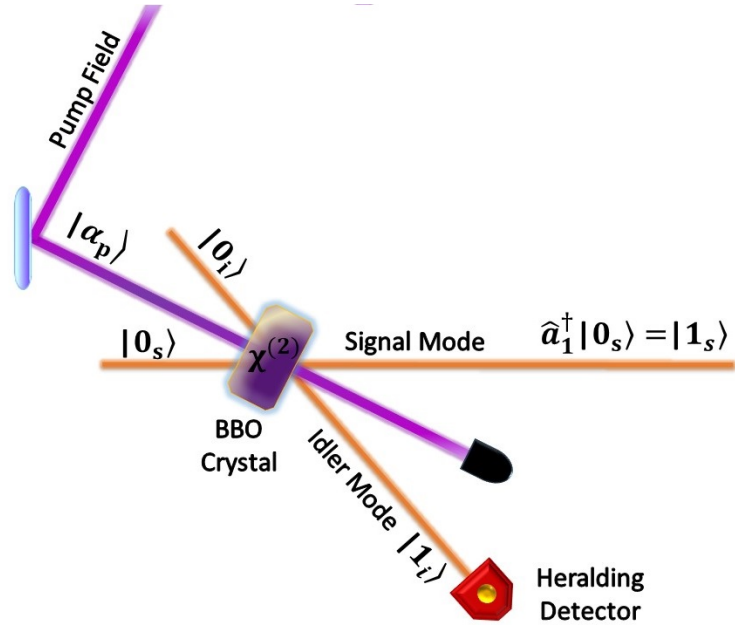## 2.2   Experimental Realization of Single Photon Addition

Figure 2.3: Schematic view of the heralded single photon addition scheme.

The generation of single photons, that in other words is the application of the $\hat{a}^{\dagger}$ operator to the vacuum state, is an "hot topic" in the quantum experimental world. As already anticipated during the description of the *number states*, a well known process to achieve this purpose is *Parametric Down Conversion* (PDC) [2]. Thanks to this process, it is possible to add a single photon in an arbitrary mode, both to the vacuum state, and so we will talk about *Spontaneous Parametric Down Conversion*, or to an arbitrary state (*Stimulated Parametric Down Conversion*). The core of each PDC-based implementation of the $\hat{a}^{\dagger}$ operator is a nonlinear optical medium. It should

have a second order nonlinear coefficient ($\chi^{(2)}$) different from zero. If we inject in such a material an intense laser beam, called *pump*, there is a non-zero probability that a photon of this beam is annihilated by the interaction with the atoms of the medium. This interaction is not resonant with any atomic level, so the pump photon is annihilated by exciting a very short-lived virtual atomic state with the simultaneous emission of two single photons at lower energy, usually called *signal* and *idler*. One of them, usually the signal one, will be the photon added to the target state, while the other will be detected, heralding the success of the operation, as shown in the schematic setup of Figure 2.3. For all the experiments described in this thesis we used a 3-mm long bulk $\beta-$barium borate (BBO) crystal as nonlinear medium. For a better understanding of the PDC process let's start from the light-matter interaction hamiltonian

$$\hat{H} = \int_V \hat{P}(\mathbf{r}, t) \cdot \hat{E}(\mathbf{r}, t) d\mathbf{r}, \tag{2.8}$$

where $\hat{P}(\mathbf{r}, t)$ describes the polarization of the medium and V is the crystal volume. The l-th polarization component of this operator can be written as a series of electric field operators as

$$\hat{P}_l(\mathbf{r}, t) = \chi_{lm}^{(1)}(\mathbf{r}) \hat{E}_m(\mathbf{r}, t) + \chi_{lmn}^{(2)}(\mathbf{r}) \hat{E}_m(\mathbf{r}, t) \hat{E}_n(\mathbf{r}, t) + ... \tag{2.9}$$

where the indices l, m, n run over the two polarization components and the summation on the repeated indices is assumed. $\chi_{lm}^{(1)}$ is the lm component of the linear susceptibility tensor while $\chi_{lmn}^{(2)}$ is its second order nonlinear term. The $\hat{E}(\mathbf{r}, t)$ operator of Equation (2.8) is the electric field representing the pump for the nonlinear process, and has the form

$$\hat{E}_l(\mathbf{r}, t) = \int \left(\hat{a}_l(\mathbf{k}, \omega) e^{-i(\mathbf{k} \cdot \mathbf{r} - \omega t)} + \hat{a}_l^\dagger(\mathbf{k}, \omega) e^{i(\mathbf{k} \cdot \mathbf{r} - \omega t)} \right) d\mathbf{k} d\omega = \hat{E}_l^{(+)}(\mathbf{r}, t) + \hat{E}_l^{(-)}(\mathbf{r}, t). \tag{2.10}$$

Since we are interested in the first order nonlinear process, we will consider only the first nonlinear term in the polarization decomposition. Among all the possible nonlinear processes we want to describe the one in which a pump photon is annihilated with the consequent generation of two lower-energy photons. So, inserting the right terms of the expressions (2.9) and (2.10) in the Equation (2.8), we find the interaction hamiltonian

$$\hat{H}_{PDC} = \int_V \chi^{(2)}_{lmn}(\mathbf{r}) \hat{E}^{(+)}_l(\mathbf{r}_p, t_p) \hat{E}^{(-)}_m(\mathbf{r}_s, t_s) \hat{E}^{(-)}_n(\mathbf{r}_i, t_i) d\mathbf{r}$$

$$= \int_V \chi^{(2)}_{lmn}(\mathbf{r}) \hat{a}_l(\mathbf{k}_p, \omega_p) \hat{a}^\dagger_m(\mathbf{k}_s, \omega_s) \hat{a}^\dagger_n(\mathbf{k}_i, \omega_i) \cdot \tag{2.11}$$

$$\cdot\, e^{-i[(\mathbf{k}_p - \mathbf{k}_s - \mathbf{k}_i)\cdot\mathbf{r} - (\omega_p - \omega_s - \omega_i)t]} d\mathbf{k}_p d\omega_p d\mathbf{k}_s d\omega_s d\mathbf{k}_i d\omega_i d\mathbf{r},$$

The indices p, s and i indicate that the relative operators act on the pump, signal and idler modes respectively. This hamiltonian governs the temporal evolution of the three involved modes according to the Schrödinger equation

$$i\hbar \frac{d}{dt} |\Psi(t)\rangle = \hat{H}_{PDC}(t) |\Psi(t)\rangle. \tag{2.12}$$

Considering that this evolution can be described also in terms of the unitary operator $\hat{U}_{PDC}(t)$ according to the equation

$$|\Psi(t)\rangle = \hat{U}_{PDC}(t) |\Psi(0)\rangle, \tag{2.13}$$

we can put the Equation (2.13) in the (2.12) and solving for $\hat{U}_{PDC}(t)$. The solution is

$$\hat{U}_{PDC}(t) = e^{-i \int_{-\infty}^t \hat{H}_{PDC}(t')dt'}, \tag{2.14}$$

that, apart from the integral required to define the shape of the mode, has the right form to describe the creation operator, according to the Equation $(2.1)^6$. As we did for the annihilation operator we have to expand the operator $\hat{U}_{PDC}(t)$ as a series of powers, but in this case we will do it respect to $\chi^{(2)}_{lmn}$. These parameters are of the order $10^{-11} \div 10^{-8}$ so we can stop the expantion at the first order of approximation. This assertion is confirmed by the experimental data. Considering the same apparatus parameters used at the end of the previous section, whit $100\,mW$ of pump power at $393\,nm$ of wavelength, we have

$$\frac{P_p}{h\nu_p} = \frac{0.1\,W}{6.6 \cdot 10^{-34}\,J \cdot s \cdot 7.5 \cdot 10^{14}\,s^{-1}} \approx 2 \cdot 10^{17} s^{-1} \tag{2.15}$$

injected photons per second in the nonlinear crystal. An averaged value for the idler count rate measured with our setup is $\approx 2000\,cps$. So we can estimate the success single photon addition probability as

$$\frac{2000\,s^{-1}}{2 \cdot 10^{17}\,s^{-1}} \approx 10^{-14}, \tag{2.16}$$

---

^{6}To clarify the notation, the signal mode, indicated with the label 1 in Equation (2.1), is here labeled with an s, while the ancillary mode (2) will be the idler mode (i).

where we are not considering the optical losses along the signal path. This number means that we generate, on average, a signal/idler photon pair every 10^{14} pump photons that traveled in the crystal. This data has to be compared with the probability to perform a double addition $(\hat{a}^\dagger)^2$, that is of the order 10^{-28} for each pump photon. So we can use the approximated version

$$\hat{U}_{PDC}(t) \approx \hat{I} - i \int_{-\infty}^{t} \hat{H}_{PDC}(t')dt', \tag{2.17}$$

instead of the Equation (2.14). To go further in the study of the Parametric Down Conversion process we have to define the initial state of the three involved modes, represented in the previous equations by $|\Psi(0)\rangle$. Generally the pump beam is a strong laser beam, so it can be considered as a coherent state with a very large mean photon number $(|\{\alpha\}\rangle_p)$ occupying the mode $\alpha_l(\mathbf{k}_p, \omega_p)$. For sake of simplicity we can start considering the signal and the idler in the vacuum state before the nonlinear crystal. So the initial state before the PDC is

$$|\Psi(0)\rangle = |\{\alpha\}\rangle_p |0\rangle_s |0\rangle_i. \tag{2.18}$$

We can now study the so-called *phase-matching conditions* that have to be satisfied to perform an efficient PDC. Applying the operator (2.17) to the state (2.18) we can obtain a preliminary expression of the PDC output state

$$\begin{aligned}
|\Psi(t)\rangle &= \hat{U}_{PDC}(t) |\Psi(0)\rangle \\
&= |\Psi(0)\rangle - i \int_{-\infty}^{t} \hat{H}_{PDC}(t') dt' |\Psi(0)\rangle \\
&= |\Psi(0)\rangle - i \int \int_{-\infty}^{t} \chi_{lmn}^{(2)}(\mathbf{r}) e^{-i(\Delta\mathbf{k}\cdot\mathbf{r} - \Delta\omega t')} \alpha_l(\mathbf{k}_p, \omega_p) \cdot \\
&\quad \cdot \hat{a}_m^\dagger(\mathbf{k}_s, \omega_s) \hat{a}_n^\dagger(\mathbf{k}_i, \omega_i) |\alpha\rangle_p |0\rangle_s |0\rangle_i \, d\mathbf{k}_p d\omega_p d\mathbf{k}_s d\omega_s d\mathbf{k}_i d\omega_i dt' d\mathbf{r},
\end{aligned} \tag{2.19}$$

where $\Delta\mathbf{k} = \mathbf{k}_p - \mathbf{k}_s - \mathbf{k}_i$ and $\Delta\omega = \omega_p - \omega_s - \omega_i$. Considering that we are not interested in the description of the signal state during the interaction inside the crystal, and also that $\hat{H}_{PDC}(t')$ is zero before and after the interaction, we can extend the time integral to $+\infty$,

$$\int_{-\infty}^{+\infty} e^{i\Delta\omega t'} dt' = \delta(\omega_p - \omega_s - \omega_i). \tag{2.20}$$

Equation (2.20) is the first phase matching condition. It is the energy conservation law that defines the relation between the pump and the signal/idler photons frequency.

Regarding the spatial integral, considering the $\chi_{lmn}^{(2)}$ susceptibility constant over the crystal volume is a reasonable assumption. So it can be solved as follows

$$
\begin{aligned}
K(\Delta\mathbf{k}) &= \int_V e^{-i\Delta\mathbf{k}\cdot\mathbf{r}}d\mathbf{r} \\
&= \int_{-\frac{L_x}{2}}^{+\frac{L_x}{2}} e^{-i\Delta k_x x}dx \int_{-\frac{L_y}{2}}^{+\frac{L_y}{2}} e^{-i\Delta k_y y}dy \int_{-\frac{L_z}{2}}^{+\frac{L_z}{2}} e^{-i\Delta k_z z}dz \\
&= 8\frac{\sin(\frac{\Delta k_x L_x}{2})}{\Delta k_x}\frac{\sin(\frac{\Delta k_y L_y}{2})}{\Delta k_y}\frac{\sin(\frac{\Delta k_z L_z}{2})}{\Delta k_z}.
\end{aligned}
\tag{2.21}
$$

This term defines the *spatial bandwidth* of the crystal. Indeed, it can be considered as a sort of spatial filter that allows the generation of the signal and idler photons only for specific combinations of the wave vectors. Equation (2.21) has a maximum for

$$
\mathbf{k}_p - \mathbf{k}_s - \mathbf{k}_i = 0,
\tag{2.22}
$$

that is the second phase matching condition and tells us that if we observe an idler photon along the direction $\mathbf{k}_i$, given the pump direction $\mathbf{k}_p$, we have the maximum probability to find the signal photon with $\mathbf{k}_s = \mathbf{k}_p - \mathbf{k}_i$. The width of the $\mathbf{k}_s$ distribution is smaller as the crystal is longer, becoming the usual momentum conservation law in the limit of infinite crystals. We can now rewrite the PDC output state in the simplified form

$$
\begin{aligned}
|\Psi(t)\rangle &= |\Psi(0)\rangle - \int \phi_{lmn}(\mathbf{k}_s,\omega_s,\mathbf{k}_i,\omega_i)\hat{a}_m^\dagger(\mathbf{k}_s,\omega_s)\hat{a}_n^\dagger(\mathbf{k}_i,\omega_i)|\alpha\rangle_p|0\rangle_s|0\rangle_i\,d\mathbf{k}_s d\omega_s d\mathbf{k}_i d\omega_i \\
&= |\Psi(0)\rangle - \int \phi_{lmn}(\mathbf{k}_s,\omega_s,\mathbf{k}_i,\omega_i)d\mathbf{k}_s d\omega_s d\mathbf{k}_i d\omega_i\,|\alpha\rangle_p|1_{\mathbf{k}_s,\omega_s}\rangle_s|1_{\mathbf{k}_i,\omega_i}\rangle_i,
\end{aligned}
\tag{2.23}
$$

where we defined the shape of the output modes of the spontaneous parametric down conversion process as

$$
\phi_{lmn}(\mathbf{k}_s,\omega_s,\mathbf{k}_i,\omega_i) = i\chi_{lmn}^{(2)}\int \alpha_l(\mathbf{k}_p,\omega_s+\omega_i)K(\Delta\mathbf{k})\,d\mathbf{k}_p.
\tag{2.24}
$$

We have to notice that this profile is the convolution between the pump profile and the crystal band. We have to be careful in the interpretation of $\phi_{lmn}(\mathbf{k}_s,\omega_s,\mathbf{k}_i,\omega_i)$ as mode profile of the signal and idler photons. They are a pair of quantum correlated (*entangled*) photons, so their individual properties are not well defined until one of them is detected, only at that time the mode distribution of the other one will be well defined[7].

---

[7]See Chapter 3 for more details about entangled systems.

We are now able to define the detection part needed to implement the heralded version of the addition operator. As for the $\hat{a}$ implementation, also to realize the $\hat{a}^\dagger$ operator we are using a probabilistic approach. The PDC process has a small success probability because of the small susceptivity coefficient, so, also in this case we need to perform a detection operation on the ancillary mode to herald the operation. A big challenge of each experiment involving the implementation of $\hat{a}^\dagger$ is to perform the addition of a single photon on a single target mode. This can be done accurately tailoring the measurement performed on the idler photon. A theoretical recipe to do this has been developed by Ou in 1997 [28] and Aichele and al.[29]. They agree in saying that a narrowband spatio-spectral filter should be placed in the heralding channel to produce high purity transform-limited single photons in the signal one. According to this suggestions we can define the heralding measurement operator as

$$\hat{\rho}_f = \int d\mathbf{k}_f d\omega_f \Gamma(\mathbf{k}_f, \omega_f) \left|1_{\mathbf{k}_f, \omega_f}\right\rangle \left\langle 1_{\mathbf{k}_f, \omega_f}\right|, \tag{2.25}$$

where $\Gamma(\mathbf{k}_f, \omega_f)$ is the band of the filter centered at the frequency ω_f and around the wave vector $\mathbf{k}_f$[8].

Defining the density operator of the biphoton state as $\hat{\rho}_{PDC} = \left|\Psi(t)\right\rangle \left\langle \Psi(t)\right|$ we can

---

[8]Respect to the SPCM description made in Section 1.3.1 we are now considering that the probability to generate Fock states with $n > 1$ is negligible in the PDC process. In this case we can restrict the description of the operator representing the SPCM to an Hilbert space of dimension 2. So we have

$$\begin{aligned}
\hat{\Pi}_{on} &= \hat{I}_{2\times 2} - \left|0\right\rangle \left\langle 0\right| \\
&= \left|0\right\rangle \left\langle 0\right| + \left|1\right\rangle \left\langle 1\right| - \left|0\right\rangle \left\langle 0\right| \\
&= \left|1\right\rangle \left\langle 1\right| \approx \hat{\rho}_f,
\end{aligned} \tag{2.26}$$

apart from the integral defining the action of the spatial and spectral filters.

mathematically formalize the heralding measurement as

$$
\begin{aligned}
\hat{\rho}_s &= Tr_i\Big\{\int d\mathbf{k}_f\, d\omega_f\, |1_{\mathbf{k}_f,\omega_f}\rangle\, \langle 1_{\mathbf{k}_f,\omega_f}|\, \Gamma(\mathbf{k}_f,\omega_f)\, |\Psi(t)\rangle\, \langle\Psi(t)|\Big\} \\
&= \sum_n \int d\mathbf{k}_f\, d\omega_f\, d\mathbf{k}_t\, d\omega_t\, \Gamma(\mathbf{k}_f,\omega_f) \langle n_{\mathbf{k}_t,\omega_t}|1_{\mathbf{k}_f,\omega_f}\rangle\langle 1_{\mathbf{k}_f,\omega_f}|\Psi(t)\rangle\langle\Psi(t)|n_{\mathbf{k}_t,\omega_t}\rangle \\
&= \int d\mathbf{k}_f\, d\omega_f\, \Gamma(\mathbf{k}_f,\omega_f)\langle 1_{\mathbf{k}_f,\omega_f}|\Psi(t)\rangle\langle\Psi(t)|1_{\mathbf{k}_f,\omega_f}\rangle \\
&= \int d\mathbf{k}_f\, d\omega_f\, d\mathbf{k}_s\, d\omega_s\, d\mathbf{k}_i\, d\omega_i\, d\mathbf{k}_{s'}\, d\omega_{s'}\, d\mathbf{k}_{i'}\, d\omega_{i'}\, \Gamma(\mathbf{k}_f,\omega_f)\cdot \\
&\quad \cdot \phi^*_{lmn}(\mathbf{k}_s,\omega_s,\mathbf{k}_i,\omega_i)\phi_{lmn}(\mathbf{k}_{s'},\omega_{s'},\mathbf{k}_{i'},\omega_{i'})\, |1_{\mathbf{k}_s,\omega_s}\rangle\, \langle 1_{\mathbf{k}_{s'},\omega_{s'}}|\, \cdot \\
&\quad \cdot \langle 1_{\mathbf{k}_f,\omega_f}|1_{\mathbf{k}_i,\omega_i}\rangle\langle 1_{\mathbf{k}_{i'},\omega_{i'}}|1_{\mathbf{k}_f,\omega_f}\rangle \\
&= \int d\mathbf{k}_f\, d\omega_f\, d\mathbf{k}_s\, d\omega_s\, d\mathbf{k}_{s'}\, d\omega_{s'}\, \Gamma(\mathbf{k}_f,\omega_f)\cdot \\
&\quad \cdot \phi^*_{lmn}(\mathbf{k}_s,\omega_s,\mathbf{k}_f,\omega_f)\phi_{lmn}(\mathbf{k}_{s'},\omega_{s'},\mathbf{k}_f,\omega_f)\, |1_{\mathbf{k}_s,\omega_s}\rangle\, \langle 1_{\mathbf{k}_{s'},\omega_{s'}}| \\
&= \int d\mathbf{k}_f\, d\omega_f\, d\mathbf{k}_s\, d\omega_s\, \Gamma(\mathbf{k}_f,\omega_f)|\phi_{lmn}(\mathbf{k}_s,\omega_s,\mathbf{k}_f,\omega_f)|^2\, |1_{\mathbf{k}_s,\omega_s}\rangle\, \langle 1_{\mathbf{k}_s,\omega_s}| \\
&= \int d\mathbf{k}_s\, d\omega_s\, \Phi(\mathbf{k}_s,\omega_s)\, |1_{\mathbf{k}_s,\omega_s}\rangle\, \langle 1_{\mathbf{k}_s,\omega_s}|\,,
\end{aligned}
\tag{2.27}
$$

where Tr_i denotes the trace over the degrees of freedom of the idler photon. In the second to last step of Equation (2.27) we made use of the phase matching conditions to evaluate the integrals over $d\mathbf{k}_{s'}$ and $d\omega_{s'}$, while in the last one we introduced the profile of the photon added in the signal channel

$$
\Phi(\mathbf{k}_s,\omega_s) = \int d\mathbf{k}_f\, d\omega_f\, \Gamma(\mathbf{k}_f,\omega_f)|\phi_{lmn}(\mathbf{k}_s,\omega_s,\mathbf{k}_f,\omega_f)|^2.
\tag{2.28}
$$

Actually, Aichele and al. showed that under reasonable hypotheses, like ignoring diffraction, spatial or temporal walkoff (by using a sufficiently short crystal) and considering gaussian collimated beams, in real scenarios it is sufficient to filter the idler detection much narrower than the pump spatial and spectral width to achieve highly pure addition operations. We can define the purity parameter for time and spatial degrees of freedom as

$$
\mathcal{P} = Tr\{\hat{\rho}_s^2\} = \mathcal{P}_{temp} \cdot \mathcal{P}_{spa},
\tag{2.29}
$$

where

$$
\mathcal{P}_{temp}(\mu_t) = \frac{1}{\sqrt{1+2\mu_t^2}}
\tag{2.30}
$$

$$
\mathcal{P}_{spa}(\mu_s) = \frac{1}{1+2\mu_s^2}.
\tag{2.31}
$$

Equations (2.31) and (2.30) summarize the Aichele' idea asserting that the temporal (spatial) purity of the added single photon depends only on the ratio $\mu_t = \sigma_\omega^f / \sigma_\omega^p$ ($\mu_s = \sigma_{\mathbf{k}}^f / \sigma_{\mathbf{k}}^p$) between the frequency (wave vector) distribution width of the heralding filter and the one of the pump. In the limit case of delta shaped filters with $\omega_f = \frac{\omega_p}{2}$ and $\mathbf{k}_f = \mathbf{k}_p - \mathbf{k}_s$ we obtain

$$
\begin{aligned}
\Phi(\mathbf{k}_s, \omega_s) &= \int d\mathbf{k}_f \, d\omega_f \delta(\mathbf{k}_f - \mathbf{k}_p + \mathbf{k}_s)\delta(\omega_f - \frac{\omega_p}{2})|\phi_{lmn}(\mathbf{k}_s, \omega_s, \mathbf{k}_f, \omega_f)|^2 \\
&= |\chi_{lmn}^{(2)} \alpha_l(\mathbf{k}_p - \mathbf{k}_f, \frac{\omega_p}{2})|^2,
\end{aligned}
\tag{2.32}
$$

that means that we have to prepare the pump field in a pure mode to obtain the added photon in an equally shaped pure mode, centered at the frequency $\frac{\omega_p}{2}$ along the direction conjugated to $\mathbf{k}_f$ according to the momentum conservation law. At this point of the analysis of the single photon addition technique we can define the *generation efficiency* parameter η_{gen}. In analogy with the detection efficiency definition, this parameter quantifies our ability to add just a single photon to a specific mode. It is clear that it is strongly linked to the spatial and temporal purity of the photon emitted by the PDC process. Other factors that degrade the addition operation are the dark counts of the heralding detector[9] and the double addition on the same mode[10]. The overall generation efficiency is defined as

$$
\eta_{gen} = \mathcal{P}_{temp} \cdot \mathcal{P}_{spa} \cdot \eta_{dark}.
\tag{2.33}
$$

In our setup the pump field is prepared as a gaussian beam with a spectral width of $\approx 0.9\,nm$ and a waist of $200\,\mu m$ by means of spatial filtering composed by a pin-hole of $35\,\mu m$ of aperture and two lenses of $75\,mm$ and $100\,mm$ of focal length. For the heralding part we used as spectral filter an ethalon cavity of width $0.1\,nm$, and for the spatial filtering a single mode fiber capable to select a propagation mode with a beam waist of $\approx 530\,\mu m$. The resulting *generation efficiency* is, considering also the small contribution of the dark counts ($\eta_{dark} = 0.99$), $\eta_{gen} \simeq 0.92$.

In order to give a full description of this technique, we need also to consider the polarization degrees of freedom. There are three possible configuration for the pump (l), signal (m) and idler (n) polarizations. We call the process *type I parametric down conversion* when $l \neq m = n$, that means that the signal and idler have the same

---

[9]When a false click come from the heralding detector we are applying on the signal mode the *identity* operator $\hat{I}$ instead of $\hat{a}^\dagger$.

[10]This contribution can be neglected in all our experimental realizations as seen before.

polarization, orthogonal to the pump, *type II parametric down conversion* if $l = m \neq n$ or $l = n \neq m$ and *type 0 parametric down conversion* the last case in which the three fields are equally polarized ($l = m = n$). The general expression for the phase matching condition can be expressed in the form [30]:

$$n_l(\omega_s + \omega_i)(\omega_s + \omega_i)\frac{\mathbf{k}_p}{|\mathbf{k}_p|} = n_m(\omega_s)\omega_s\frac{\mathbf{k}_s}{|\mathbf{k}_s|} + n_n(\omega_i)\omega_i\frac{\mathbf{k}_i}{|\mathbf{k}_i|}. \tag{2.34}$$

Before going further in this analysis we have to notice that the BBO crystal, in which the PDC process occurs, is an uniaxial birefringent medium. Referring to Figure A.1 and restricting to the degenerate process, for which $\omega_s = \omega_i = \frac{\omega_p}{2}$, we can, for example, study the *type 0* case. Equation (2.34) for *type 0* PDC has the form:

$$2n_{e,o}(\omega_p)\frac{\mathbf{k}_p}{|\mathbf{k}_p|} = n_{e,o}(\frac{\omega_p}{2})\frac{\mathbf{k}_s}{|\mathbf{k}_s|} + n_{e,o}(\frac{\omega_p}{2})\frac{\mathbf{k}_i}{|\mathbf{k}_i|}, \tag{2.35}$$

where the three modes (p, s and i) feel the same refractive index[11]. For common crystals $n(\omega)$ is an increasing function of ω, so Equation (2.35) has no solutions without a careful engineering of the refractive index [31][32]. In our experimental setup we exploited *type I parametric down conversion*, in the degenerate case, where $\omega_s = \omega_i$. Considering $\mathbf{k}_p$ directed along the y-axes of Figure A.1, the phase matching conditions for this case are

$$2n_{e,o}(\omega_p) = n_{o,e}(\frac{\omega_p}{2})\Big(\frac{k_s^y}{|\mathbf{k}_s|} + \frac{k_i^y}{|\mathbf{k}_i|}\Big)$$
$$\frac{k_s^{x,z}}{|\mathbf{k}_s|} + \frac{k_i^{x,z}}{|\mathbf{k}_i|} = 0. \tag{2.36}$$

Now the pump feels a refractive index different from that of the signal and the idler ($n_e(\omega) \neq n_o(\omega)$), so the first equation can be solved. The x, z part of Equation (2.36) tells us that the *signal* and *idler* photons are emitted along a cone.

Addition of a Single Photon to an Arbitrary Input State

We restricted the previous analysis to the case of vacuum as initial state of the signal mode (Eq. (2.18)). With the right precautions, the generalization to the case of single photon addition to an arbitrary signal state ($|\Psi_{\mathbf{k}_s,\omega_s}\rangle$) is quite straight forward. The only one request is to use as seed an arbitrary state mode matched with the signal

---

[11]We can consider the wave vector of the pump field aligned along the y axis of Figure A.1. If its polarization lies on the z axis all the fields will feel the extraordinary refractive index (n_e), otherwise, if it is aligned along the x axis they feel n_o.

mode. In this way, the detection of an idler photon will herald the presence of the state in Equation (2.37) in the signal mode

$$\hat{\rho}_s = \int d\mathbf{k}_s d\omega_s \Phi(\mathbf{k}_s, \omega_s) \hat{a}_m^\dagger(\mathbf{k}_s, \omega_s) |\Psi_{\mathbf{k}_s,\omega_s}\rangle \langle\Psi_{\mathbf{k}_s,\omega_s}| \hat{a}_m(\mathbf{k}_s, \omega_s), \qquad (2.37)$$

where $|\Psi_{\mathbf{k}_s,\omega_s}\rangle$ is a generic initial state of the signal mode.

In the particular case of using a coherent state as initial signal state, this request can be relaxed. Indeed, we have only to take care that it occupy a spatial and spectral mode broader than the Local Oscillator one. This is justified by the fact that we will always analyze the results of our experiments using a homodyne detector. Indeed, according to the results of Section 1.3.2, the Local Oscillator acts like a filter, making the detector blind to the portion of the signal out of its mode. So, if we match the mode of the LO to the one over which we perform the addition, we can neglect the remaining part of the initial signal state simply considering an initial state of reduced amplitude.

2.3 Experimental Superposition of Single Photon Quantum Operations

From a general point of view, all the experiments that will be discussed in this thesis will aim to demonstrate some fundamental aspects of quantum mechanics. One of its pillar is the superposition principle. Due to this, an atom, for example, can be in an excited state or in the ground state at the same time. Transposing this concept to the macroscopic world would lead to the famous Schrödinger's cat paradox [33], that makes the microscopic world apparently so different from the one in which we live. The ability to experimentally deal with the quantum superposition is challenging. Along the years various techniques to implement superpositions of heralded quantum operators has been used to demonstrate fundamental relations like the quantum commutation rules [5]. The experimental implementation of the operator superposition is based on a simple idea. Let's consider the operator $\hat{A}_{1,2}$ acting on the mode 1, heralded by the presence of a single photon in the mode 2. Similarly the operator $\hat{B}_{1,3}$ acts on the same mode and has the heralding photon in the mode 3. If we trigger an homodyne measurement performed on the mode 1 on a coincidence between the clicks in mode 2 and 3, we will see the action of the sequence $\hat{A}_{1,2}\hat{B}_{1,3}$. If instead we want to study the effect of the superposition between these two operators $(\hat{A}_{1,2} + \hat{B}_{1,3})$, we have to trigger the homodyne detection on a signal that erases the information about what

operator acted. To do this we have to make the two heralding photons interfere in a beam-splitter after an accurate matching of the two paths 1 and 2, and then we have to use one of the two output of the BS as heralding. If we can neglect the probability to simultaneously perform the two operations, such a trigger heralds the operation $(c_1 \hat{A}_{1,2} + c_2 e^{i\varphi} \hat{B}_{1,3})$, as it is shown in Figure 2.4.
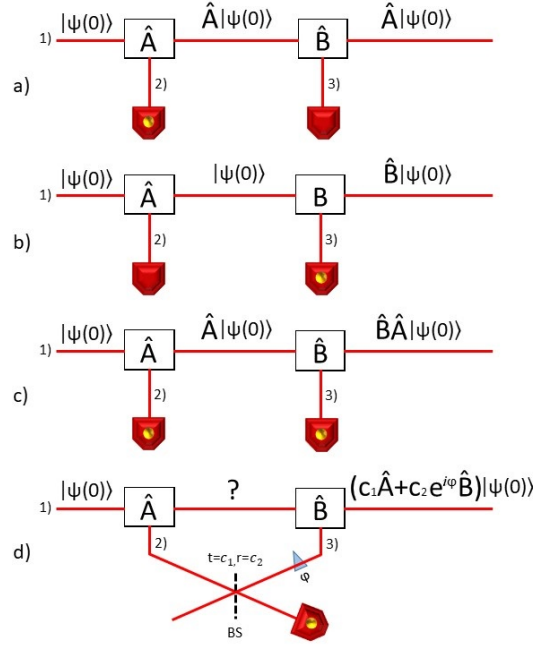

Figure 2.4: a) If we perform an homodyne measurement to characterize the mode 1 when we see a click only in the trigger detector placed along the path of mode 2, we will see the effects of the application of the operator $\hat{A}_{1,2}$. Similarly, the scheme b) shows the effects on the initial state when we see a click only in the detector on mode 3. Case c) shows that if we trigger the homodyne detection on the coincidence between the two heralding events we are applying to the mode 1 the sequence of the two operators, $\hat{A}_{1,2}\hat{B}_{1,3}$. The last part of this figure d) is the setup needed to implement the superposition between the two operators. The two heralding modes are mixed in a beam-splitter after a careful compensation of their relative phase. Considering negligible the probability to perform simultaneously the two operations compared to just one of them, we can see a click in the detector when the heralding modes are in the state $|1\rangle_2 |0\rangle_3$ or $|0\rangle_2 |1\rangle_3$, with no possibility to distinguish the two cases. This indistinguishability projects the operator acting on the mode 1 on the superposition $(c_1 \hat{A}_{1,2} + c_2 e^{i\varphi} \hat{B}_{1,3})$.

The ratio between the weights c_1 and c_2 can be controlled varying the transmission (reflection) coefficient of the beam-splitter. The setup showed in Figure 2.4 d) is the basic scheme used to implement the superposition between heralded operators. We can then slightly modify it to implement more complicated and interesting operations. For the realization of the experiment that I will discuss in the last part of this chapter we used this idea to implement the superposition between different sequences of the operators $\hat{a}$ and $\hat{a}^\dagger$. Exploiting the polarization degrees of freedom for the realization of the annihilation operator and a PDC crystal for the creation one, we can implement the operator $(c_1 \hat{a} \hat{a}^\dagger + c_2 e^{i\varphi} \hat{a}^\dagger \hat{a})$, as shown in Figure 2.5.
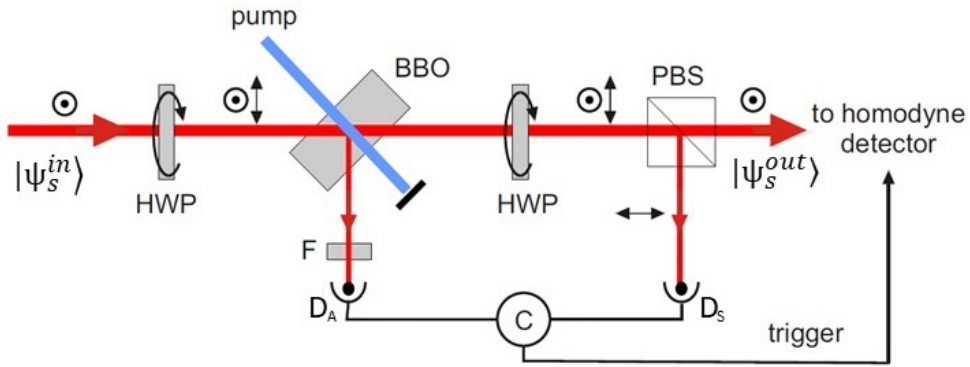

Figure 2.5: From the left to the right we have the initial signal state in the vertical polarization mode. The first HWP rotates a single photon from the signal to the horizontal polarization mode, performing the first subtraction with a given, low, probability. Later, considering type I PDC, only the vertical component of the signal interacts in the BBO crystal with the horizontal polarized pump. A click in the addition detector D_A heralds the generation of a single photon in the signal mode. The second HWP acts as the first one. Due to the low success probability for the subtraction operation we can neglect the case in which we have two single photons in the vertical polarization mode of the signal. Therefore the PBS separates the two polarizations sending the subtraction heralding photon to the second detector D_S and erasing the information about which HWP acted. Acquiring the homodyne signal only when we see the coincidence between the two detector events ensures to characterize the state after the application of the desired superposition of operators.

In this setup, the polarizing beam-splitter (PBS) removes a single photon from the spatial mode in which the signal travels, giving us no information about the time at which it has been subtracted from the polarization mode of the signal, before or after

the addition operation. The coincidence of a click from the two detectors (D_A and D_S) does not allow one to distinguish what sequence has been performed, $\hat{a}\hat{a}^\dagger$ or $\hat{a}^\dagger\hat{a}$. Mathematically, this scheme is described by the sequential application of an unitary low reflectivity beam-splitter transformation (Eq. (2.6)), followed by the unitary PDC operator (Eq. (2.14)) and again another low reflectivity beam-splitter, in the usual low probability regime.

$$\begin{aligned}
\hat{U}_{sub}(\gamma_3)\hat{U}_{add}(\gamma_2)\hat{U}_{sub}(\gamma_1) &= e^{i\gamma_3(\hat{a}_1\hat{a}_4^\dagger+\hat{a}_1^\dagger\hat{a}_4)}e^{i\gamma_2(\hat{a}_1^\dagger\hat{a}_3^\dagger+\hat{a}_1\hat{a}_3)}e^{i\gamma_1(\hat{a}_1\hat{a}_2^\dagger+\hat{a}_1^\dagger\hat{a}_2)} \\
&\approx \left[\hat{I}+i\gamma_3(\hat{a}_1\hat{a}_4^\dagger+\hat{a}_1^\dagger\hat{a}_4)\right]\cdot \\
&\quad\cdot\left[\hat{I}+i\gamma_2(\hat{a}_1^\dagger\hat{a}_3^\dagger+\hat{a}_1\hat{a}_3)\right]\cdot \\
&\quad\cdot\left[\hat{I}+i\gamma_1(\hat{a}_1\hat{a}_2^\dagger+\hat{a}_1^\dagger\hat{a}_2)\right].
\end{aligned} \tag{2.38}$$

Here the subscript 1 indicates an operator acting on the signal mode, while 2, 3 and 4 represent the ancilla mode of the first subtraction, of the addition and the second single photon subtraction in this order. γ_1, γ_2 and γ_3 are their success probability as discussed in the previous sections. Neglecting the terms representing the simultaneous application of the three operations ($\hat{a}\hat{a}^\dagger\hat{a}$) and considering that the three ancillary mode are initially in the vacuum state, we can infer the form of the operator describing the action performed on the signal state when we see a coincidence between the triggers of Figure 2.5.

$$\begin{aligned}
|\Psi^{out}\rangle &= \hat{U}_{sub}(\gamma_3)\hat{U}_{add}(\gamma_2)\hat{U}_{sub}(\gamma_1)|\psi_s^{in}\rangle_1|0\rangle_2|0\rangle_3|0\rangle_4 \\
&\approx \left[\hat{I}+i\gamma_1\hat{a}_1\hat{a}_2^\dagger+i\gamma_2\hat{a}_1^\dagger\hat{a}_3^\dagger+i\gamma_3\hat{a}_1\hat{a}_4^\dagger-\gamma_1\gamma_2\hat{a}_1\hat{a}_1^\dagger\hat{a}_2^\dagger\hat{a}_3^\dagger+\right. \\
&\quad\left.-\gamma_1\gamma_3\hat{a}_1\hat{a}_1\hat{a}_2^\dagger\hat{a}_4^\dagger-\gamma_2\gamma_3\hat{a}_1^\dagger\hat{a}_1\hat{a}_3^\dagger\hat{a}_4^\dagger\right]|\psi_s^{in}\rangle_1|0\rangle_2|0\rangle_3|0\rangle_4 \\
&= |\psi_s^{in}\rangle_1|0\rangle_2|0\rangle_3|0\rangle_4+i\gamma_1\hat{a}_1|\psi_s^{in}\rangle_1|1\rangle_2|0\rangle_3|0\rangle_4+i\gamma_2\hat{a}_1^\dagger|\psi_s^{in}\rangle_1|0\rangle_2|1\rangle_3|0\rangle_4+ \\
&\quad+i\gamma_3\hat{a}_1|\psi_s^{in}\rangle_1|0\rangle_2|0\rangle_3|1\rangle_4-\gamma_1\gamma_2\hat{a}_1\hat{a}_1^\dagger|\psi_s^{in}\rangle_1|1\rangle_2|1\rangle_3|0\rangle_4+ \\
&\quad-\gamma_1\gamma_3\hat{a}_1\hat{a}_1|\psi_s^{in}\rangle_1|1\rangle_2|0\rangle_3|1\rangle_4-\gamma_2\gamma_3\hat{a}_1^\dagger\hat{a}_1|\psi_s^{in}\rangle_1|0\rangle_2|1\rangle_3|1\rangle_4.
\end{aligned} \tag{2.39}$$

The POVM describing the trigger apparatus is $\hat{\Pi}=|1\rangle_3\langle1|\otimes(|1\rangle_2\langle1|+|1\rangle_4\langle1|)$. We can obtain the density operator describing the state after the transformation tracing out the ancillary modes:

$$\begin{aligned}
\hat{\rho}^{out} &= Tr_{2,3,4}\left[\hat{\Pi}|\Psi^{out}\rangle\langle\Psi^{out}|\right] \\
&= (\gamma_1\gamma_2\hat{a}_1\hat{a}_1^\dagger+\gamma_1\gamma_3\hat{a}_1^\dagger\hat{a}_1)|\psi_s^{in}\rangle\langle\psi_s^{in}|(\gamma_1\gamma_2\hat{a}_1^\dagger\hat{a}_1+\gamma_1\gamma_3\hat{a}_1\hat{a}_1^\dagger).
\end{aligned} \tag{2.40}$$

The operator applied to the initial state is therefore

$$\hat{O}_{sup} = \mathcal{N}\left(\hat{a}_1\hat{a}_1^\dagger + \frac{\gamma_3}{\gamma_2}\hat{a}_1^\dagger\hat{a}_1\right), \tag{2.41}$$

where $\mathcal{N}$ is a normalization factor. From Equation (2.41) it is clear that the relative success probability of the two sequences of operations ($\hat{a}\hat{a}^\dagger$ or $\hat{a}^\dagger\hat{a}$) can be arbitrary set by acting on the rotation of the two HWPs.

2.4 Measurement-induced strong Kerr nonlinearity for weak quantum states of light

In this section, I will show an experiment in which, using the basic ingredients described in the previous sections, we are able to emulate the effect of a strong Kerr nonlinearity on weak quantum states of light [34].

Strong nonlinearity at the single photon level represents a crucial enabling tool for optical quantum technologies, forming the basis of innumerable photonic devices. Unfortunately, its use in quantum optics and optical quantum information processing often requires strong nonlinear coupling between single photons, that it is hard to obtain experimentally. This is because the typical nonlinearities of common non-resonant optical media are many orders of magnitude weaker than what is required for these applications. Among all the possible nonlinear interactions, Kerr effect is a fundamental one, which leads to dependence of the refractive index on the intensity of light that propagates through the nonlinear medium, enabling e.g. for the realization of important logical gates for quantum computing [35][36]. Despite its theoretical interest, the large amount of experimental problems strongly limited its use. Moreover, during the years, several works pointed out that the very nature of light-matter interaction may prevent achievement of a sufficiently strong Kerr nonlinearity for weak quantum optical fields [37][38]. To overcome this problem, specially tailored media with enhanced nonlinearities, such as clouds of ultra-cold atoms, have been studied [39][40]. Despite the interesting results, this kind of approach remains extremely complex and challenging. In 2001, Knill, Laflamme, and Milburn showed, in their landmark paper, that effective nonlinear interactions at the single-photon level can be implemented with the use of optical interference, single photon detection and auxiliary single photons [41]. In this approach, the single photon detection provides the desired nonlinearity. The resulting linear optical quantum gates are generally probabilistic, as implied by the fact that they

are driven by quantum measurements, but their success probability can be boosted arbitrarily close to 1 by using more ancilla photons and more complex interferometric schemes [41][42]. This concept has triggered an immense amount of theoretical and experimental works. For example, following this approach, a quantum-noise limited phase insensitive amplification has been implemented solely by a homodyne detection and feedforward [43].

2.4.1 Theory

At the quantum level, the Kerr nonlinear interaction is described by a Hamiltonian which is a quadratic function of the photon number operator $\hat{n}$[44],

$$\hat{H}_k = \hbar k \hat{a}^{\dagger 2} \hat{a}^2 = \hbar k \hat{n}(\hat{n} - 1), \tag{2.42}$$

where k is the Kerr nonlinear coefficient. The resulting unitary transformation of the quantum state of the optical mode is diagonal in Fock basis, which means that each Fock state $|n\rangle$ acquires a phase shift which is a non-linear function of n,

$$|n\rangle \xrightarrow{KerrEffect} e^{i\Phi\hat{n}(\hat{n}-1)} |n\rangle , \tag{2.43}$$

with $\Phi = kt$, where t is the time variable. Strong Kerr nonlinearity with $\Phi \approx 1$ would enable e.g. generation of macroscopic superpositions of coherent states [45], implementation of entangling quantum gates for universal quantum computing [46], and complete Bell state measurement in quantum teleportation [47][2].

With this experiment we showed the successful implementation of a strong Kerr nonlinearity by measurement-induced quantum operations on weak quantum states of light. Specifically, we emulate this interaction on the smallest non-trivial subspace spanned by the vacuum, single-photon and two-photon states, $|0\rangle$, $|1\rangle$ and $|2\rangle$. In this subspace, the Kerr interaction transforms a generic input state according to

$$e^{-\frac{i\hat{H}_k t}{\hbar}} \left(c_0 |0\rangle + c_1 |1\rangle + c_2 |2\rangle \right) = c_0 |0\rangle + c_1 |1\rangle + e^{-2i\Phi} c_2 |2\rangle . \tag{2.44}$$

We target a Kerr nonlinearity with $\Phi = \pi/2$, which induces a π-phase shift of the two-photon Fock state with respect to states $|0\rangle$ and $|1\rangle$. Up to a linear π-phase shift which flips the sign of odd Fock states[12], and an unimportant overall phase factor -1,

---

[12] The phase shift operator is defined as $\hat{U}(\Phi) = e^{-i\hat{n}\Phi}$.
A π phase shift on a state in the subspace $|0\rangle$, $|1\rangle$ and $|2\rangle$ is equivalent to

$$\hat{U}(\pi)(c_0 |0\rangle + c_1 |1\rangle + c_2 |2\rangle) = c_0 |0\rangle + e^{-i\pi} c_1 |1\rangle + e^{-2i\pi} c_2 |2\rangle = c_0 |0\rangle - c_1 |1\rangle + c_2 |2\rangle . \tag{2.45}$$

this transformation is equivalent to a π-phase shift in the amplitude of the vacuum state on the three-dimensional subspace considered, i.e.,

$$c_0 \left|0\right\rangle + c_1 \left|1\right\rangle - c_2 \left|2\right\rangle \xrightarrow[-1\ overall\ phase\ factor]{\pi-shift} -c_0 \left|0\right\rangle + c_1 \left|1\right\rangle + c_2 \left|2\right\rangle. \tag{2.46}$$

The change of sign in the amplitude of the vacuum component is thus the signature of the strong Kerr nonlinearity that we wish to demonstrate in our experiment. To implement the gate in Equation (2.46) we made use of the scheme in Figure 2.5. As seen in the previous section, this scheme allows us to to implement the transformation

$$\hat{V}(\hat{a}, \hat{a}^\dagger) = A\hat{a}\hat{a}^\dagger + B\hat{a}^\dagger\hat{a}, \tag{2.47}$$

that, making use of the relations $\hat{a}^\dagger\hat{a} = \hat{n}$ and $\hat{a}\hat{a}^\dagger = \hat{n} + \hat{I}$, becomes

$$\hat{V}(\hat{n}) = (A + B)\hat{n} + A\hat{I}. \tag{2.48}$$

The free parameters A and B have to be set according to the relations[13]

$$\begin{cases} \frac{V(1)}{V(0)} = \frac{2A+B}{A} = -1 \\ \frac{V(2)}{V(1)} = \frac{3A+2B}{2A+B} = 1 \end{cases} \tag{2.49}$$

to implement the wanted transformation of the coefficients as in Equation (2.46) $\left(\hat{V}(c_0 \left|0\right\rangle + c_1 \left|1\right\rangle + c_2 \left|2\right\rangle) = -c_0 \left|0\right\rangle + c_1 \left|1\right\rangle + c_2 \left|2\right\rangle\right)$. This system has no solutions, so, to make our task feasible we have to consider a simultaneous noiseless amplification [43] of the state

$$c_0 \left|0\right\rangle + c_1 \left|1\right\rangle + c_2 \left|2\right\rangle \xrightarrow[+\ Noisless\ Amplification]{Kerr\ Tranformation\ +} -c_0 \left|0\right\rangle + gc_1 \left|1\right\rangle + g^2 c_2 \left|2\right\rangle, \tag{2.50}$$

where $g > 1$ is the amplification factor.

$$\begin{cases} \frac{V(1)}{V(0)} = \frac{2A+B}{A} = -g \\ \frac{V(2)}{V(1)} = \frac{3A+2B}{2A+B} = g \end{cases} \rightarrow \begin{cases} g = 1 + \sqrt{2} \\ \frac{B}{A} = -3 - \sqrt{2} \end{cases} \tag{2.51}$$

That is the equivalent of the system (2.49), modified to take in account the amplification, with the relative solutions. It has to be noticed that the amplification doesn't spoil the signatures of nonlinearity. On the contrary, it is actually beneficial, because

---

[13]In Equation 2.49 the symbols V(n) have to be interpreted as $V(n) = \left\langle n\right| \hat{V}(\hat{n}) \left|n\right\rangle$. So, for example, $V(0) = \left\langle 0\right| (A + B)\hat{n} + A\hat{I} \left|0\right\rangle = A$.

we intend to probe the quantum operation with weak coherent states and the amplification makes the desired nonlinear effect even more visible. Otherwise, if wishing to achieve the nonlinearity in Equation (2.46) without amplification, one could either use two photon subtractions and additions instead of one [48], or the output state of Equation (2.50) could be noiselessly attenuated [49][50] with the help of a beam-splitter with amplitude transmittance $t = 1/g$, a highly efficient single-photon detector, and conditioning on observation of no photons at the auxiliary output port of the beam-splitter. The experiment requires the precise and stable setting of the relative weights and phases of the operator superposition to implement the desired conditional transformation. The resulting output states are subjected to balanced homodyne detection and finally analyzed via a full quantum state tomographic reconstruction.
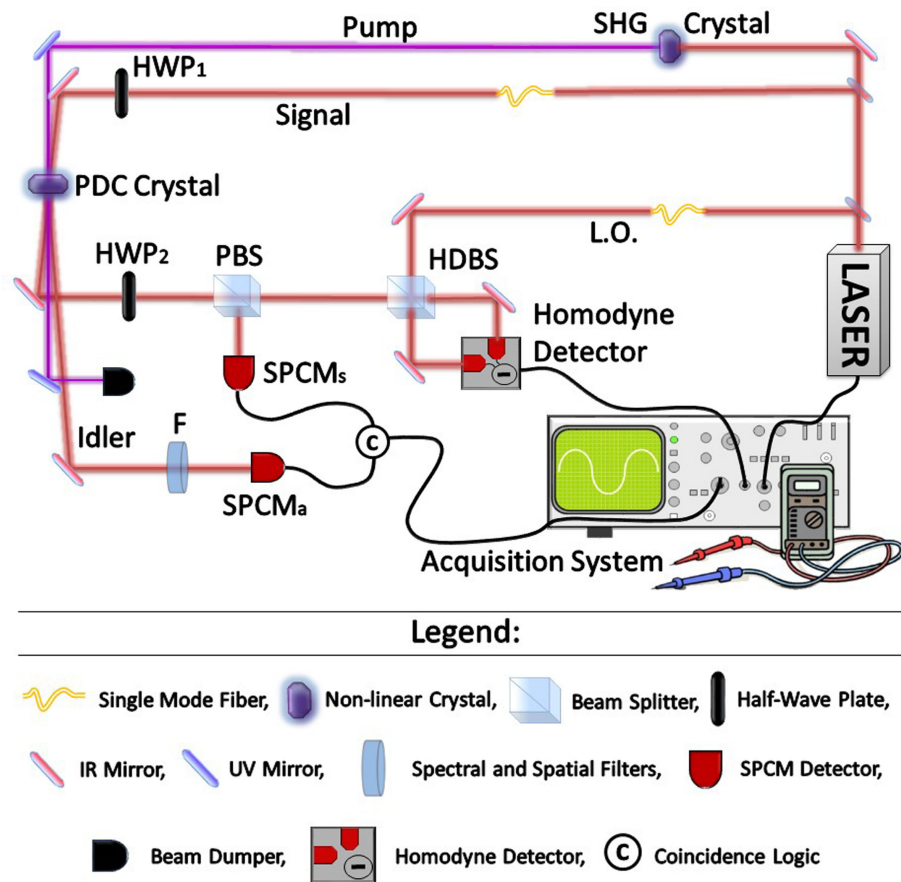
2.4.2 Experimental Details

Figure 2.6: Experimental setup schematic illustration.

The Laser   For all our experiments we used a Mode Locked Ti:sapphire laser emitting $1.5\,ps$ long pulses at a repetition rate of $80\,MHz$[14]. The emission is centered at $786\,nm$ of wavelength, distributed in a gaussian profile of width $0.6\,nm$. As shown in Figure 2.6, the output of this laser is splitted in three main portions. The largest of them is frequency doubled via a *Second Harmonic Generation* (SHG) process that occurs in a lithium triborate (LBO) crystal. The UV ($393\,nm$) output, of approximately $400\,mW$, is used as pump beam for the degenerate, non-collinear, type-I Parametric Down Conversion that occurs in a 3-mm long β-barium borate (BBO) crystal. As explained in Section 2.2 this process is used to implement the $\hat{a}^\dagger$ operator. The second part of the main laser beam is very attenuated to generate the weak coherent state ($|\alpha\rangle$) used as initial state of the transformation (2.50). The procedure used to set a specific vale of the amplitude of this state is described in Appendix C. The last portion of light is used as Local Oscillator for the Homodyne Detector.

Weights and Phase Adjustment   To satisfy the conditions (2.51) for the relative success probability of the sequence $\hat{a}^\dagger\hat{a}$ respect to $\hat{a}\hat{a}^\dagger$ we act on the rotation of the wave plates HWP_1 and HWP_2 of Figure 2.6. According to the Malus' law, the probability to rotate a photon from a linearly polarized beam to the orthogonal polarization is proportional to $\cos^2(\theta_{HWP})$, where θ_{HWP} is the angle between the polarization of the incoming beam and the axis of the plate. In the setting of these angles we have to keep in mind that the implementation of the $\hat{a}$ operator via the half wave plate scheme requires a low subtraction probability (Section 2.1). To satisfy both the conditions we tilted the first HWP of 4 degrees respect to the vertical polarization of the weak coherent state, while the second one of 1.9 degrees. The minus sign in the ratio $B/A = -(3 + \sqrt{2})$ can be obtained by rotating the first HWP in the opposite direction to the second one, with respect to the orientation corresponding to $\theta_{HWP} = 0$. Due to the birefringence of the BBO crystal[15], there is a spatio-temporal walk-off between the subtracted photon (horizontally polarized) from HWP_1 and the signal (vertically polarized), after the addition stage. The heralding photon from the second HWP does not suffer of this effect. This problem has the consequence to make the two subtraction heralding photons partially distinguishable. To compensate this effect we placed a second BBO crystal, identical to the one used for the $\hat{a}^\dagger$ implementation, between HWP_1 and the PDC crystal (not shown in Figure 2.6). This is rotated in such a way

---

[14]This means that each pulse is separated from the next one by ca. $12.5\,ns$.

[15]See Appendix A for more details about birefringence.

that its extraordinary axis is parallel to the ordinary axis of the PDC crystal. The fact that these two BBO have the same length ensure the walk-off compensation.

Detection   I already anticipated that the output of this experiment will be characterized using an Homodyne Detector. As we saw in Section 1.3.2, the Local Oscillator acts like a filter for the HD, making the detector only sensitive to the part of the signal in the same mode of the LO. We can start from here to better define the concept of single mode in our experiment. Every optical state with the same mode profile of the LO is defined as a single mode state. Our Homodyne Detector must be able to measure the quadrature distribution for each single mode, so we can study the properties of the single mode profile function of the LO beam to clarify how we optimize our setup to perform the characterization of manipulated states:

- LO Polarization Profile: Linear, vertically oriented.

  From the detection point of view the polarization features are not a problem because the HD photodiodes are insensitive to the polarization. To ensure that the signal lies in the same polarization mode of the LO we placed a polarizer, aligned with the LO, before the signal input port of the HDBS (not shown in Figure 2.6)

- LO Spatial Profile: The LO is spatially shaped, using a three-lens system, to obtain a gaussian beam with a waist of $200\,\mu m$ at a distance from the center of the Homodyne beam-splitter equal to the distance between this device and the PDC crystal.

  We can ensure the generation of the single photon from the addition stage in the LO spatial mode by manipulating the pump beam to have a waist of $200\,\mu m$ at the PDC crystal position (see Section 2.2). To produce the initial weak coherent state for our Kerr transformation in a single "spatial" mode, we have to shape it in such a way that it will have the same beam waist at the same position. Also for the $\hat{a}$ stage, we have to engineer the spatial mode collected by the fiber coupled to the heralding SPCM (see Section 2.1) with the same features.
  After the HDBS the output beams are focused on the two HD photodiodes (Hamamatsu S3883, active area of $1.7\,mm^2$). They have been also selected to have a good quantum efficiency in the spectral region of our laser emission.

- LO Spectral Profile: The LO is an unmodified portion of the output beam of the main laser, so its spectral profile has the same properties of the laser, described in the previous paragraph.

  Using the same laser to generate the LO and the signal state, all the involved beams have the same spectral properties. The only problems could come from the Parametric Down Conversion photon, that could be emitted at a different frequency from the LO. But, choosing the degenerate configuration, with a pump at a frequency double of the LO frequency, and highly filtering the heralding idler photon, we obtain an added single photon at the right wavelength (see Section 2.2).

- LO Temporal Profile: As for the spectral profile, the LO has the same temporal properties of the main laser. We can define a single temporal mode as a single light pulse with these features.

  The Homodyne Detector must be able to discern the electronic signal corresponding to each LO pulse from the next one, allowing for a *temporally resolved* homodyne detection. To achieve this purpose the overall electronic circuit of the detector has been designed to have a bandwidth of $100\,MHz$[16].
  We placed optical delays based on translation stages along the paths of the LO and signal pulses to accurately synchronize them.

The overall *mode matching efficiency*, obtained thanks to the procedures just described, can be checked with the technique described in Appendix B.
With our setup, for each trigger event[17] we acquire, via a Tecktronix oscilloscope (TDS7104), the HD signal corresponding to four consecutive LO pulses. The first one corresponds to the manipulated state, while the others, unaffected by the Kerr transformation, are used to control the stability of the system. Each optical pulse of length $1.5\,ps$ is converted, by the overall electronic circuit, in a voltage signal of approximately $10\,ns$ of duration. The quadrature value relative to each signal mode

---

[16]The main limitation for the detector bandwidth comes from the electronic circuit of the amplifier that performs the subtraction between the photocurrents produced by the two photodiodes. An home-made circuit has been realized, taking great care to minimize the stray capacitance that is the main cause of bandwidth reduction.

[17]See Appendix D for more details about the trigger apparatus.

is obtained by measuring the area of the electronic signal corresponding to each LO pulse.

To reach the best performance regime of the HD, a few other preliminary steps are required. The first one is an accurate balancing of the power at the output ports of the HDBS. This ensures the 50:50 splitting ratio of the homodyne beam-splitter, required for a balanced measure, as described in Section 1.3.2. Also the bias voltage of the two HD photodiodes has to be finely tuned, minimizing the residual $80\,MHz$ component of the HD signal after the subtraction of their photocurrents. This is required to maximize the *extinction ratio* between the photocurrents. This parameter is defined as the ratio between the signal measured when the two photodiodes are illuminated, and the one measured when one of them is blocked. For our detector, a value of $-42dB$ has been measured for this ratio[18]. Finally, to select the working point for the LO power, we checked the linearity of the detector exploiting the Equation (1.58). The results of a measurement of the variance of the HD signal relative to an input vacuum state, for various LO powers, are reported in Figure 2.7. Above $9\,mW$ of LO power, the detector is no longer linear, so we should stay below this limit during the measurements to avoid deviations from the theory derived in Section 1.3.2.
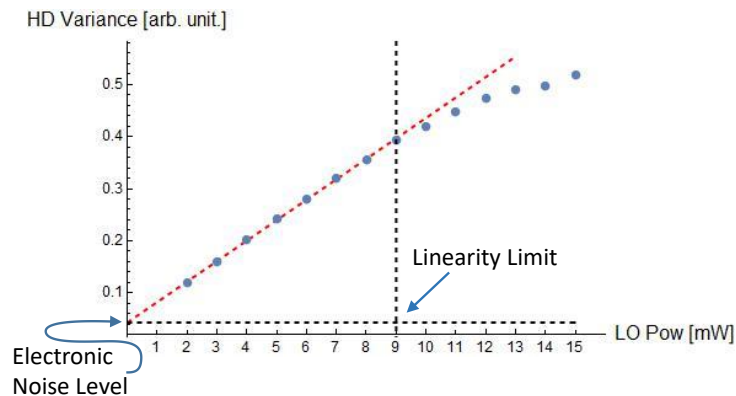

Figure 2.7: Linearity check made on our homodyne detector. The variance of the homodyne signal is measured for various powers of the Local Oscillator, injecting a vacuum state in the input port of the detector.

Using $9\,mW$ of LO power we have a signal amplification above the electronic noise

---

[18]In Section 1.3.2, when we introduced the losses effect, we made the implicit assumption that the two photodiodes are identical (we used the same detection efficiency for both of them). The maximization of the *extinction ratio* ensures the validity of this assumption.

(*signal-to-noise ratio*) of $9.6\,dB$. This parameter can be used to calculate the contribution of the electronic apparatus to the detection efficiency, leading to[19] $\eta_{el} = 0.9$.

2.4.3 Results

A full tomographic reconstruction is performed on the input and output states for three different values of the input coherent state amplitude, $\alpha = 0.23$, 0.53, and 0.79. We used an iterative maximum likelihood procedure (See Section 1.4), incorporating the effect of a finite ($\eta_{det} = 0.66$) detection efficiency, to reconstruct the density matrices in a 8×8 space in the Fock basis (from 0 to 7 photons). To do this we acquired a set of 50000 quadrature values for 9 different relative phases between the LO and the target state. The stabilization of the relative phase between the LO and the input coherent state during the measurement time is performed by locking the DC component of the HD signal. When a slow modulation is applied to the LO phase, we can see the interference fringes due to the interaction between the LO and the signal state in the HDBS. A mirror, mounted on a piezo actuator, along the LO path, is used to lock the fringe signal to different values, corresponding to different relative phases. The reconstructed density matrices are shown in Figure 2.8, together with those calculated by applying the $\hat{V}(\hat{n})$ operator on the input coherent states. The desired Kerr nonlinearity signature is evident in all the experimental data. All the off-diagonal terms containing a vacuum contribution are clearly negative, witnessing the expected sign change in the amplitude of the vacuum component. However, when comparing the experimental density matrices to those expected according to the transformation (2.48) with ideal parameters $B/A = -(3 + \sqrt{2})$ (rightmost column in Figure 2.8), some discrepancy is apparent. The most notable is the appearance of a small imaginary component. We found that all the experimental results can be reproduced very well (with fidelities around 90%) by using a single set of modified parameters in the $\hat{V}(\hat{n})$ transformation, corresponding to a B/A ratio of -5.97 and to an additional phase of about $\frac{\pi}{7}$ between the two terms in the operator superposition. Such small deviations from the ideal configuration, which only marginally affect the signatures of the sought nonlinearity, are fully compatible with the delicate alignment and setting of the proper small rotation angles in the wave plates responsible for the operator superposition. Another relevant aspect of our protocol to implement strong Kerr nonlinearity is that it does not involve post selection processes. The successful implementation of the

---

[19]See Section 1.3.2 for more details.

operation (2.50) is heralded solely by measurements on auxiliary modes, thus making the output state available for further processing and applications. In conclusion, our results confirm the feasibility of the method described above to realize strong Kerr transformations for quantum states of light, paving the way for its implementation in quantum computational schemes.
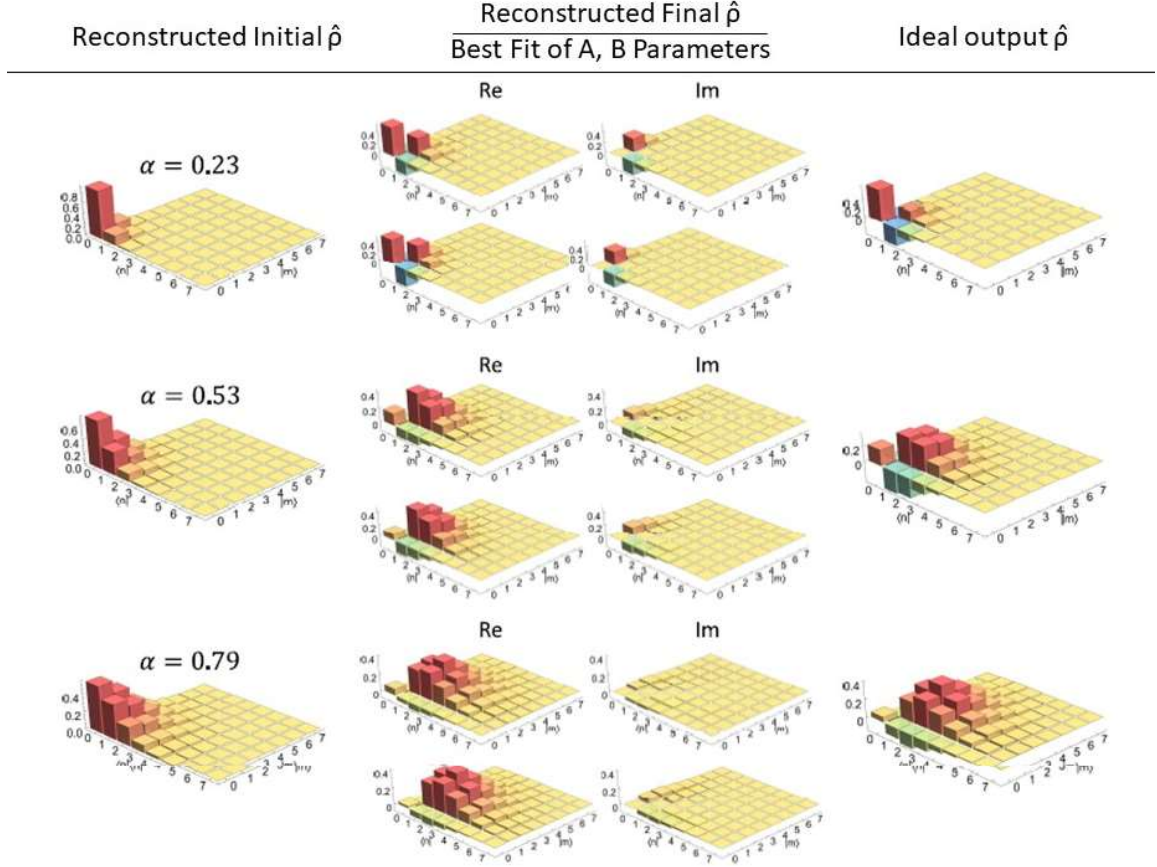
Figure 2.8: Reconstructed density matrices of input coherent states and output states after the emulated Kerr nonlinear interaction. The left column shows the real part of the reconstructed density matrices of the input coherent states (the imaginary part is negligible here). For each input state, the two central columns show the real and imaginary parts for the reconstructed output states (upper plots), together with those calculated from a best fit of the parameters in the applied $\hat{V}(\hat{n})$ transformation (lower plots). The corresponding fidelities are $F = 0.88, 0.86, 089$ for $\alpha = 0.23, 0.53, 0.79$, respectively. Finally, the right column shows the expected output states (containing no imaginary parts) that one would obtain from the ideal $\hat{V}(\hat{n})$ transformation with $B/A = -3 - \sqrt{2}$.

Chapter 3

Multi-Mode State Manipulation

We started the previous chapter with the description of the techniques used to implement the $\hat{a}$ and $\hat{a}^\dagger$ operators. We underlined, in many occasions, the importance of the *mode* concept, showing the experimental precautions that have to be considered to realize the single photon addition and subtraction on a specific target mode. Going further in Chapter 2 we focused on the manipulation of a single mode state, with the aim of emulating the effects of a strong Kerr nonlinearity on a weak traveling coherent state. Although experiments of this kind are fundamental to investigate some aspects of the quantum nature of light, they do not give us the possibility to study all of them. Indeed, already from the early period of quantum mechanics, there were interesting debates about the properties of multimode systems that can not be investigated dealing only with single mode states. Expanding the number of modes involved in a quantum optics experiment leads to a growth of complexity, both from the theoretical and the experimental point of view, but the ability to manipulate and characterize systems containing more than one mode is fundamental to study phenomena that mark the distance between the quantum world and the one in which we live. The most charming and controversial is for sure the *entanglement*. In the following chapter I will describe how to manipulate and measure a multi-mode optical system in order to investigate this property.

The entanglement is a direct consequence of the quantum mechanics formalism. This feature arises by the fact that, while in classical physics the phase space of a composed system is always represented by the Cartesian product of the phase spaces describing each subsystem, in quantum physics the concept of phase space is substituted with the Hilbert space [51]. In this context the state of a multipartite system is the tensor product of the Hilbert spaces of all the subsystems ($H_{tot} = \otimes_{i=1}^{n} H_i$). This has as

consequence that not all the states of a quantum system can be written as the product of the state vectors of each individual subsystem. This fact has been used by Werner in 1989 [52] to define an entangled state as the one that can not be expressed like a *separable state*, a state described by the product of the individual subsystem state vectors. Formally, such a separable (pure) state has the form:

$$|\Psi\rangle = |\Psi_1\rangle \otimes |\Psi_2\rangle \otimes \cdots \otimes |\Psi_n\rangle \,, \tag{3.1}$$

where $|\Psi_1\rangle, |\Psi_2\rangle, \cdots, |\Psi_n\rangle$ are the states of each individual subsystem. A generic state of an $n-$partite system has instead the form

$$|\Psi\rangle = \sum_{i_1,\ldots,i_n} c_{i_1,\ldots,i_n} |i_1\rangle \otimes |i_2\rangle \otimes \cdots \otimes |i_n\rangle \,, \tag{3.2}$$

where $|i_n\rangle$ is an orthonormal base for the whole system. Equation (3.2) can be reduced to Equation (3.1) only in same specific cases, splitting the ensemble of all possible states for a multipartite system in two groups, the *separable states* and the *entangled* ones. To better understand what dealing with an entangled state means let's make an example. Let's consider the state

$$|\psi_{AB}\rangle = \frac{1}{\sqrt{2}}(|H\rangle_A |V\rangle_B + |V\rangle_A |H\rangle_B), \tag{3.3}$$

where A and B label two different modes of the electromagnetic field, the two subsystems, and H and V are the polarizations of two single photon states present in each mode[1], respect to a common reference shared between them. This is clearly an entangled state according to the Werner definition. The interesting properties of this kind of states emerge if we look at each individual mode separately. Measuring the polarization state of the mode A (B) we will see, half of the time, an horizontal polarization and every other time, a vertical polarization. This means that we don't have any information about the individual subsystems but the correlations in the global state are well determined[2]. The quantum mechanics interpretation of this fact is based on the superposition principle. The two modes A and B are, at the same time, in the states $|H\rangle_A |V\rangle_B$ and $|V\rangle_A |H\rangle_B$. Only when one of them is measured, the global state of the system collapses in one of the two possibilities. In this way one can not define the state of each subsystem at any time, and this lead to the problems with

---

[1]The same conclusions hold for other kinds of physical systems like $\frac{1}{2}$ spin particles, etc.

[2]When an horizontal polarization is measured in mode A, a vertical one is certainly observed in mode B and viceversa.

the concept of *realism*. Moreover, there are no restriction about the distance between the two subsystems at the moment of the measurement. It means that, despite their relative location, a measure performed on one of them instantaneously influences the state of the other (problem of *locality*). These implications led Einstein, Podolsky and Rosen, who first discussed the effects of entanglement in 1935 [53][3] to consider it as the proof that quantum mechanics is an incomplete theory. For a long time, many scientists tried to explain the effects of entanglement considering the existence of some *hidden variables*, not experimentally accessible, that determine the state of the global system at the moment of its generation, trying to reproduce the "strange" predictions of quantum mechanics in a more classical way. Many of these theories also tried to solve the problem of locality, going under the name of *Local Hidden Variable Models* (LHVM). The solution of this dispute came from the work of Bell, in 1964 [54], when he formalized the LHVM. The main assumptions that he made were:

1. the results of a measurement are determined by the a priori properties of the system, independently from the measurement itself (realism),

2. acting on a part of the system does not influence the result of a measurement performed on another part, distant from the first one (locality),

3. the choice of the apparatus settings is independent from the hidden variables that determine the state of the system (freedom).

According to these constrains, Bell found the maximal value of the correlation that can occur between the results of measurements performed on a bipartite system, usually called *Bell inequality*. Then, he also proved that, performing suitable measurements on a quantum entangled bipartite system, this bound can be overcome. Bell's work is the theoretical discriminant between quantum mechanics and the LHVM. It asserts that these two theories are not compatible, putting an end to the attempt to incorporate the concepts of realism and locality in the quantum mechanics. The experimental answer came almost twenty years later, when Aspect et al. performed the first convincing test of the violation of the Bell inequality [55][56]. This, and many following experiments [57][58][59], confirmed the quantum mechanical predictions, putting entanglement at the basis of new ideas, like quantum cryptography [60][61], quantum dense coding [62], quantum teleportation [63], and many others. A crucial point for all these applications is the necessity to determine if a system is entangled or not, and to quantify the amount

---

[3]In the same period Schröedinger reached the same results independently [33].

of entanglement. This problem becomes more difficult to solve if we consider that, in real laboratory scenarios, it is more common to produce mixed states rather than pure states of the form (3.2). In this case, a state is separable if and only if it can be written in the form

$$\rho = \sum_i p_i \rho_1^i \otimes \rho_2^i \otimes \cdots \rho_n^i, \tag{3.4}$$

where $\rho_1, \cdots, \rho_n$ are the density operators of each subsystem, and the conditions $\sum_i p_i = 1$ and $p_i \geq 0$ must hold. All the states that can not be written as in Equation (3.4) are entangled. The problem of the detection and quantification of this property in the case of mixed states became harder when Werner showed the existence of some entangled mixed states that don't violate Bell's inequality. A milestone in the context of entanglement detection was then placed by Peres in 1996 [64], and later completed by M. Horodecki et al. [65].

Peres-Horodecki Criterion   Let's consider a bipartite system[4] in a separable state according to the definition (3.4). It can be described by the density operator ρ_{AB}, where A and B label the two subsystems. Fixing a product basis for the Hilbert spaces of A and B we can write the density matrix elements as[5]

$$\rho_{nm\nu\mu} = \langle n| \langle \nu| \rho_{AB} |\mu\rangle |m\rangle. \tag{3.5}$$

Let's define also the *Partial Transposition* operation corresponding to the transposition of only the indices relative to one subsystem. We will indicate it with the symbol T_A if it acts on the subsystem A ($\rho_{nm\nu\mu} \xrightarrow{T_A} \rho_{mn\nu\mu}$) or T_B if it acts on B ($\rho_{nm\nu\mu} \xrightarrow{T_B} \rho_{nm\mu\nu}$). This criterion asserts that, *if and only if* ρ_{AB} describes a separable state of a bipartite system, than also the operator $T_B\rho_{AB}$ (or $T_A\rho_{AB}$) is a physical density operator. Mathematically, this means that also $T_B\rho_{AB}$ must have unitary trace and non-negative eigenvalues. If this is not the case, it means that we are able to transform a physical state of the composite system into a non-physical one, acting on a single subsystem, which is not possible without the presence of quantum correlations (entanglement). Twice the sum of the negative eigenvalues of $T_B\rho_{AB}$ defines the NPT parameter (Negative under Partial Transposition) [64] that can be used to quantify the amount of entanglement. This parameter is zero for separable states, while it is 1 for maximally

---

[4]A system composed by two subsystems, e.g. the one of Equation (3.3).

[5]To clarify the notation, the Latin indices refer to the subsystem A, while the Greeks to B.

entangled systems. The Peres-Horodecki criterion is a necessary and sufficient condi-
tion to determine the presence of entanglement in bipartite systems of dimension $2 \otimes 2$
and $2 \otimes 3$ [64]. For systems of higher dimensions it is only a sufficient condition, indeed
there are entangled states whose density operator remains positive after partial transpo-
sition. In the following of this chapter I will use the NPT to quantify the entanglement.

We need to do a final step in the introduction of the entanglement before starting
to describe the experiment that I will show in the second part this chapter: we have to
clarify the case of the so called *Single-Particle Entanglement*. Between 2005 and 2006
this phenomenon has been deeply analyzed in a series of publications, with authors
Van Enk [66][67] and Drezet [68]. The question was: is the state

$$|\psi\rangle_{AB} = \frac{1}{\sqrt{2}}(|0\rangle_A |1\rangle_B + |1\rangle_A |0\rangle_B) \tag{3.6}$$

entangled? As usual, the labels A and B refer to the two different parts of a bipartite
system, while 0 and 1 denote the absence or presence of a particle in each mode. The
main arguments used to claim that there is no entanglement in the state (3.6) are:

1. One needs at least two particles for entanglement.

2. The state (3.6), when written in second-quantized representation has the form:

$$|\psi\rangle_{AB} = \frac{(\hat{a}_A^\dagger + \hat{a}_B^\dagger)}{\sqrt{2}} |0\rangle_A \otimes |0\rangle_B . \tag{3.7}$$

   that is clearly not entangled.

Van Enk proposed a simple but efficient gedanken-experiment to show the presence of
entanglement in (3.6). Let's use the optical framework to illustrate it, but we have to
keep in mind that it is applicable to more general situations. In this context, $|0\rangle_{A(B)}$
stands for no photons in the mode $A(B)$ and $|1\rangle_{A(B)}$ corresponds to one photon in
the same mode. Let's also assume that the modes A and B are two distinct spatial
directions along which the optical states travel. We can think to place a cavity on the
path of each involved spatial mode, and we can also put an atom in each of them,
initially prepared in the ground state $|g\rangle$. From the experimental point of view, it is
possible to engineer the cavities and the two optical modes to let the photon enter the
cavity and interact with the atom, exciting it to a specific state $|e\rangle$. Thus, starting
with the two modes in the state (3.6) and the atoms in the ground state, we will end

with

$$|\Psi\rangle_{AB} = \frac{1}{\sqrt{2}}(|g\rangle_A |e\rangle_B + |e\rangle_A |g\rangle_B), \tag{3.8}$$

for the atomic part, while the optical modes will be in the vacuum state after the interaction. In the Equation (3.8), A and B represent the location of the atoms inside the cavities. At this point, Van Enk concludes that the state (3.8) is an entangled state of two particles (the two distinct atoms), so the condition 1) is now satisfied, and also that there is no motivation to write the state of two distinguishable particles in a second-quantized form. Due to the fact that the interaction between the optical state and the atoms is *local*, no entanglement can be generated during this process [69]. Thus, we have to conclude that the entanglement, clearly present in (3.8), was also present in (3.6), and that, at the moment of the interaction, it has been transferred to the atomic system. With his arguments, Van Enk underlined the fact that entanglement is a property concerning at least two Hilbert spaces, related to some degree of freedom of the system. For the atomic system in the state (3.8), the two involved Hilbert spaces ($\mathcal{H}_A$ and $\mathcal{H}_B$) describe the energetic structure of the atoms placed in the location A and B. We can say that $\mathcal{H}_A$ and $\mathcal{H}_B$ are entangled in (3.8) with respect to the internal state degree of freedom of the two atoms. Accordingly, we just have to consider that the two Hilbert spaces describe two spatial modes of the traveling electromagnetic waves, while the degree of freedom with respect to which they are entangled is the particle number. To further stress the point 2, we can note that the absence of entanglement arises from an incomplete notation used to switch to the second-quantized form. Indeed, one really should write

$$|\psi\rangle_{AB} = \frac{1}{\sqrt{2}}(\hat{a}^\dagger_A \otimes \hat{I}_B + \hat{I}_A \otimes \hat{a}^\dagger_B) |0\rangle_A \otimes |0\rangle_B, \tag{3.9}$$

that clearly represents a nonlocal operation that leads to an entangled state.

During my master thesis I generated an optical state of the form (3.6) and I used the method described in reference [70] to detect the presence of entanglement, concluding that this kind of state can be considered entangled also from the experimental point of view. In the following chapter I will show how it is possible to move the degree of entanglement present in the single particle entangled state (Equation 3.6) to the macroscopic domain, in which each mode contains a macroscopic number of photons.

3.1 Single Photon Delocalized Addition

In this section I will describe a setup capable of experimentally generating the Single Particle Entangled state of Equation (3.6). It involves the basic ingredients used to realize the $\hat{a}^\dagger$ operator, as described in Chapter 2, plus some other trick. In the last part of this section I will show how it is possible to modify this setup to generate a new and more interesting entangled state, which will be used in the experiment presented in the last part of this chapter.

3.1.1 Delocalized Photon Addition to Vacuum States

A common method used to generate the state (3.6) makes use of a Single photon emitter, whose output is sent to the input port of a balanced beam-splitter.
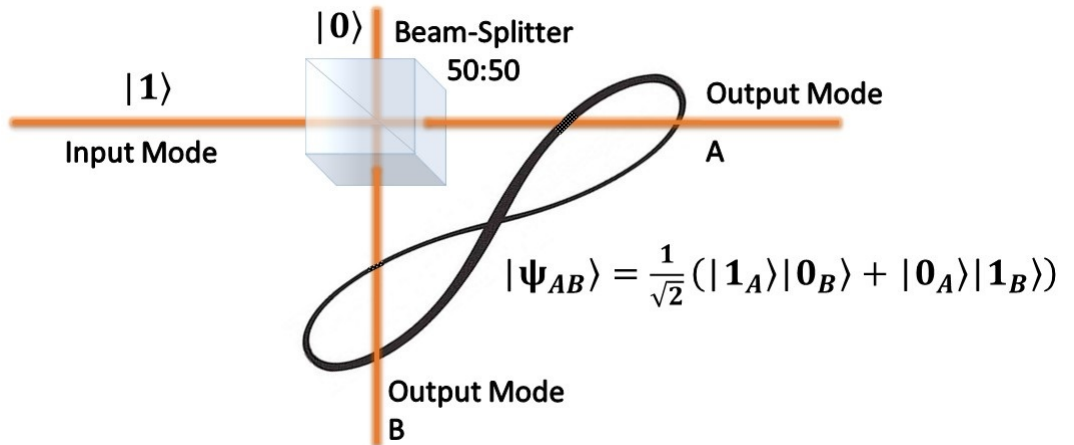
Figure 3.1: Schematic representation of a beam-splitter based setup used to generate the state (3.6).

The output modes, labeled A and B in Figure 3.1, are in the state

$$|\psi\rangle_{AB} = \frac{1}{\sqrt{2}}\Big(|0\rangle_A |1\rangle_B + |1\rangle_A |0\rangle_B\Big).\tag{3.10}$$

This is a well known method, largely used in quantum computation [41]. Based on this concept, an experimental realization of the quantum-teleportation protocol has been demonstrated [71]. Nevertheless, I will describe a more complex strategy to achieve the same purpose, but this will provide the basis for understanding the next part of this work.
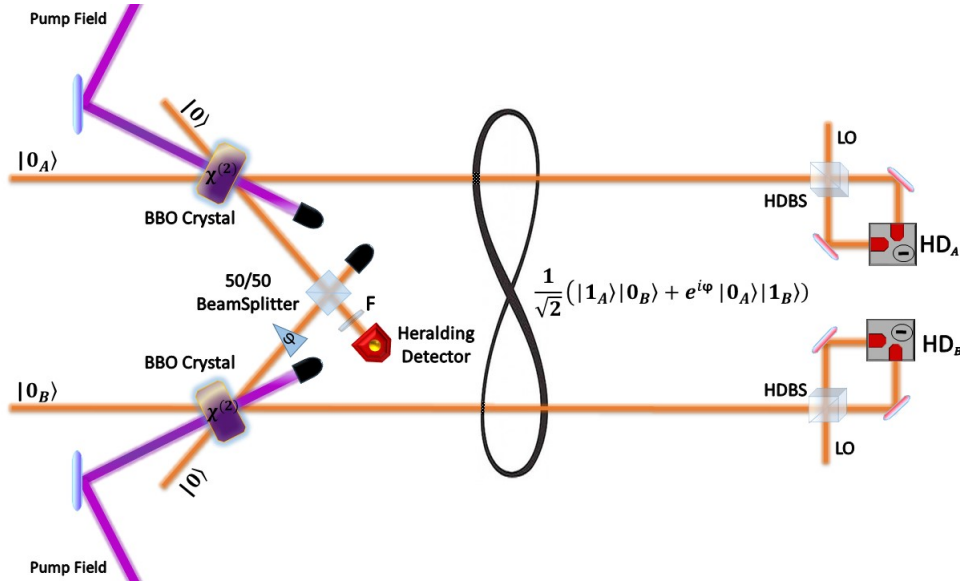
Figure 3.2: Schematic representation of the setup used to generate the state (3.6) based on the delocalized single photon addition.

In Figure 3.2, two $\hat{a}^\dagger$ operations, acting on signal modes labeled A and B, are implemented using two PDC crystals (see Section 2.2). Both the signal and idler channels are, initially, in the vacuum state. After the nonlinear process, the two idler modes are mixed in a 50:50 beam-splitter. Using the same expedients adopted in Section 2.3 to realize the superposition between different operators acting on the same mode, here we can erase the information about the mode on which the addition has been performed, erasing the knowledge about the origin of the idler photon. Indeed, a click in the heralding detector is produced, half of the time, by a photon coming from the upper PDC of Figure 3.2 (acting on the A signal mode), while in the other half from the bottom one (triggering the addition on the mode B). So, measuring just one of the two outputs one can not know (not even in principle) where the idler photon is coming from. This allows us to realize the superposition between two operators (they are the same in this case, $\hat{a}^\dagger$) acting on two different modes. Finely tuning the relative length of the path of the two idler modes we can control the phase of the superposition (φ). The filter (F), placed before the heralding detector, ensures that, when we see a click, we can be certain that the single photon in the signal modes has a good purity (see again Section 2.2). The operation triggered by the heralding detector is $(\hat{a}_A^\dagger \otimes \hat{I}_B + e^{i\varphi}\hat{I}_A \otimes \hat{a}_B^\dagger)$, and we call it *Delocalized Single Photon Addition*. As I showed in Section 2.2, the PDC implementation of the $\hat{a}^\dagger$ operator can be generalized to add

a single photon to a arbitrarily populated mode. In recent years, it has been demonstrated that, injecting a coherent state in one of the two signal channels and vacuum in the other, a so-called hybrid discrete/continuous-variable entanglement [72] can be generated.

3.1.2 Delocalized Photon Addition to Coherent States

The setup in Figure 3.2 can be used to investigate the problem of entangling large systems. Indeed, if we inject two identical coherent states ($|\alpha\rangle$) in the signal modes of the nonlinear crystals, the output modes A and B will be in the state

$$
\begin{aligned}
|\Psi_{AB}\rangle &= \mathcal{N}(\hat{a}_A^\dagger \otimes \hat{I}_B + e^{i\varphi}\hat{I}_A \otimes \hat{a}_B^\dagger)|\alpha\rangle_A |\alpha\rangle_B \\
&= \mathcal{N}\Big(\hat{a}_A^\dagger |\alpha\rangle_A |\alpha\rangle_B + e^{i\varphi}|\alpha\rangle_A \hat{a}_B^\dagger |\alpha\rangle_B\Big) \\
&= \mathcal{N}\Big(|\alpha,1\rangle_A |\alpha\rangle_B + e^{i\varphi}|\alpha\rangle_A |\alpha,1\rangle_B\Big),
\end{aligned}
\tag{3.11}
$$

where $\mathcal{N}$ is the normalization factor and $|\alpha,1\rangle$ indicates a coherent state on which a single photon addition has been performed. This kind of state has been characterized in [73] and is called *Single Photon Added Coherent State* (SPACS). In particular, the mean photon number of each mode ($\bar{n} = |\alpha|^2$) can be made arbitrarily large by increasing the amplitude of the injected coherent states, until reaching the macroscopic regime. It is interesting to note the link between the state (3.11) and the one obtained applying two identical displacement operators on both the modes A and B of the single particle entangled state (3.10):

$$
\begin{aligned}
|\Psi_{AB}\rangle &= \mathcal{N}\Big(|\alpha,1\rangle_A |\alpha\rangle_B + e^{i\varphi}|\alpha\rangle_A |\alpha,1\rangle_B\Big) \\
&= \mathcal{N}\Big(\hat{a}_A^\dagger \otimes \hat{I}_B + e^{i\varphi}\hat{I}_A \otimes \hat{a}_B^\dagger\Big)\hat{D}_A(\alpha)\hat{D}_B(\alpha)|0\rangle_A |0\rangle_B \\
&= \mathcal{N}\underbrace{\hat{D}_A(\alpha)\hat{D}_A^\dagger(\alpha)}_{\hat{I}_A}\underbrace{\hat{D}_B\hat{D}_B^\dagger(\alpha)}_{\hat{I}_B}\Big(\hat{a}_A^\dagger\hat{D}_A(\alpha) \otimes \hat{D}_B(\alpha) + e^{i\varphi}\hat{D}_A(\alpha) \otimes \hat{a}_B^\dagger\hat{D}_B(\alpha)\Big)|0\rangle_A |0\rangle_B \\
&= \mathcal{N}\hat{D}_A(\alpha) \otimes \hat{D}_B(\alpha)\Big(\hat{D}_A^\dagger(\alpha)\hat{a}_A^\dagger\hat{D}_A(\alpha) \otimes \hat{I}_B + e^{i\varphi}\hat{I}_A \otimes \hat{D}_B^\dagger\hat{a}_B^\dagger\hat{D}_B(\alpha)\Big)|0\rangle_A |0\rangle_B \\
&= \mathcal{N}\hat{D}_A(\alpha) \otimes \hat{D}_B(\alpha)\Big((\hat{a}_A^\dagger + \alpha^*\hat{I}_A) \otimes \hat{I}_B + e^{i\varphi}\hat{I}_A \otimes (\hat{a}_B^\dagger + \alpha^*\hat{I}_B)\Big)|0\rangle_A |0\rangle_B \\
&= \mathcal{N}\Big[\hat{D}_A(\alpha) \otimes \hat{D}_B(\alpha)\Big(\hat{a}_A^\dagger \otimes \hat{I}_B + e^{i\varphi}\hat{I}_A \otimes \hat{a}_B^\dagger\Big)|0\rangle_A |0\rangle_B + \\
&\quad + \alpha^*(1 + e^{i\varphi})\hat{D}_A(\alpha) \otimes \hat{D}_B(\alpha)|0\rangle_A |0\rangle_B\Big] \\
&= \mathcal{N}\Big[\hat{D}_A(\alpha) \otimes \hat{D}_B(\alpha)\Big(|1\rangle_A |0\rangle_B + e^{i\varphi}|0\rangle_A |1\rangle_B\Big) + \alpha^*(1 + e^{i\varphi})|\alpha\rangle_A |\alpha\rangle_B\Big],
\end{aligned}
\tag{3.12}
$$

for which it is easy to calculate the normalization factor

$$\mathcal{N}^2 = \langle \Psi_{AB} | \Psi_{AB} \rangle = 2\Big(1 + |\alpha|^2(1 + \cos(\varphi)\Big). \tag{3.13}$$

From Equation (3.12) we can see that the state generated by the setup of Figure 3.2, when the signal modes are seeded with two coherent states, is the same of the one obtained applying the operator $\hat{D}_A(\alpha) \otimes \hat{D}_B(\alpha)$ on the output modes of the setup in Figure 3.1 only if $\varphi = \pi$. The setup in Figure 3.12 is more versatile than the one of Figure 3.1 and more suitable to study the entanglement properties of a macroscopic system.

The form of the state $|\Psi_{AB}\rangle$ obtained in Equation (3.12) is useful to understand the interesting entanglement properties of this kind of states. Since this property is invariant under local operations, we can apply the operator $\hat{D}_A(-\alpha) \otimes \hat{D}_B(-\alpha)$ to $|\Psi_{AB}\rangle$, and then easily calculate the NPT value:

$$NPT(\alpha, \varphi) = \frac{1}{1 + |\alpha|^2(1 + \cos(\varphi))}. \tag{3.14}$$

It is interesting to note that, if we set the operator superposition phase φ equal to 0, the amount of entanglement decreases fast while increasing the mean photon number of the injected coherent state. On the contrary, setting $\varphi = \pi$, the NPT value is constant and maximal for all the α values. Figure 3.3 shows the NPT behavior for the odd ($\varphi = \pi$) and even ($\varphi = 0$) version of the state (3.11), varying the injected mean photon number in the modes A and B.
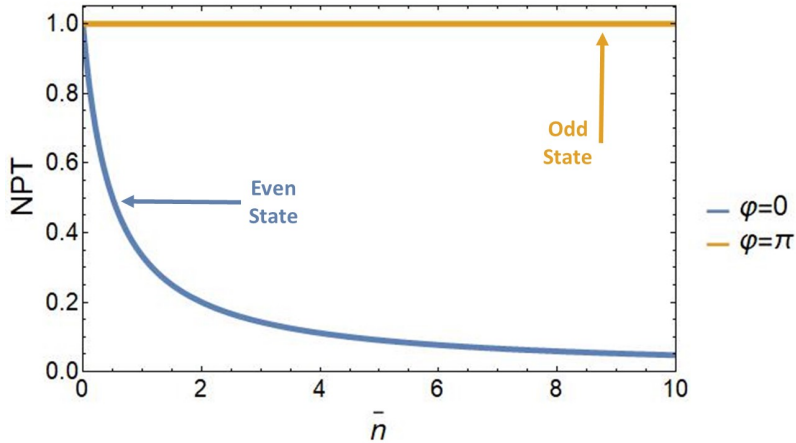

Figure 3.3: NPT of the state (3.11) for different values of the mean photon number injected in the signal modes. The yellow line represents the entanglement behavior of odd version of the state, while the blue one correspond to the odd verion.

The differences between the odd and the even state can be understood analyzing the last line of Equation (3.12). When the phase φ is equal to π, the separable part of the state ($|\alpha\rangle_A |\alpha\rangle_B$) is erased, making the state $|\Psi_{AB}\rangle$ equal to the displaced single particle (maximally) entangled state. Otherwise, in the even state, the separable part is maximal and may quickly mask the entangled contribution for large $|\alpha|$.

In our opinion, it is very interesting to experimentally test if, applying the delocalized photon addition operator, it is possible to generate an entanglement between separable states of arbitrary macroscopicity. In the next section, I will report about the methods and results of an experiment that we carried out to generate and characterize the odd version of the state (3.11).

Another peculiarity that distinguishes the odd from the even state is the so called *discorrelation* [74]. This property concerns the joint photon number probability of the two modes

$$P(n_A, n_B) = |\langle n_A| \langle n_B|\Psi_{AB}\rangle|^2 = Tr\Big\{|n_A\rangle \langle n_A| \otimes |n_B\rangle \langle n_B| \hat{\rho}_{AB}\Big\}, \qquad (3.15)$$

where $\hat{\rho}_{AB} = |\Psi_{AB}\rangle \langle \Psi_{AB}|$ is the the density operator of the state (3.11). Its matrix elements, expressed in the Fock basis, have the form:

$$\langle n_A| \langle n_B| \hat{\rho}_{AB} |m_B\rangle |m_A\rangle =$$
$$= \frac{e^{-2\alpha^2}\alpha^{(n_A+n_B+m_A+m_B-2)}(n_A + e^{i\varphi}n_B)(m_A + e^{i\varphi}m_B)}{2\big(1 + \alpha^2\big(1 + \cos(\varphi)\big)\big)\sqrt{n_A!n_B!m_A!m_B!}}, \qquad (3.16)$$

where I used a phase reference in which the coherent states injected in the PDC crystal have real amplitude. The behavior of $P(n_A, n_B)$ is shown in Figure 3.4 for the two cases. While for the even state, performing a photon number measurement on both the modes A and B, the probability to obtain the same result is very high, in the odd case it is zero. The discorrelation is one of the many forms of correlation that can be observed in the quantum world. Differently from anti-correlation and decorrelation, it can be summarized in the fact that "the joint photon number probability $P(n,n)$ of measuring n photons in each mode is precisely zero for all n, but the marginal distributions $P(n_A) = Tr_B\{\hat{\rho}_{AB}\}$ $(P(n_B))$ are nonzero for all n_A (n_B)". This property reminds the fact that the two spatial modes of the state (3.11) are entangled respect to the photon number degree of freedom, according to the idea of Van Enk discussed at the beginning of this Chapter.
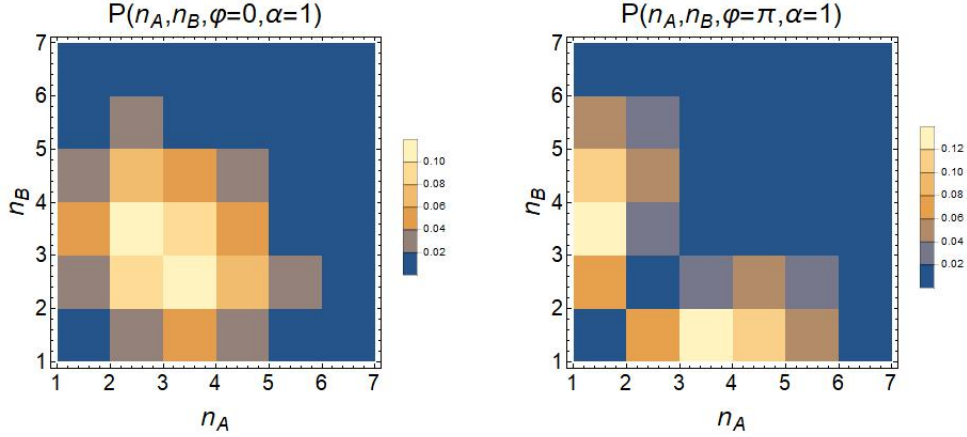
Figure 3.4: Joint photon number probability of the state (3.11) for the even (on the left) and the odd superposition (on the right).

3.2 Entangled and Discorrelated Macroscopic States of Light

3.2.1 Time Bins Implementation: Experimental Details

To experimentally test the theory presented in the previous section we chose to delocalize the addition of a single photon between two well-separated temporal modes ("*time bins*", [75]), instead of using spatial modes as described above. This is a convenient choice from the experimental point of view that does not modify the relevant properties of the state. Looking at Figure 3.2 it is easy to note that entangling two spatial modes requires two nonlinear crystals and two detection devices. In general, enlarging the number of modes by exploiting the spatial degrees of freedom requires a consequent increase of the elements needed to generate and characterize the state under test. Moreover, the parts of the composed system travel along different paths, suffering different losses and phase fluctuations. This experimental inconvenient can cause a strong degradation of entanglement, making its detection more and more complicated. On the contrary, as it can be noticed looking at Figure 3.5, the time bin implementation allows us to increase the number of modes without increasing the resources needed. The main request that has to be satisfied to realize this kind of implementation concerns the spectral bandwidth of the detector device. It has to be able to discriminate the involved modes, without mixing them. Roughly speaking, the detector has to be fast enough to acquire the signal relative to each mode without any contamination by

the others.

$$|\psi_{AB}\rangle = \mathcal{N}(|\alpha, 1\rangle_A |\alpha\rangle_B + e^{i\varphi}|\alpha\rangle_A|\alpha, 1\rangle_B)$$
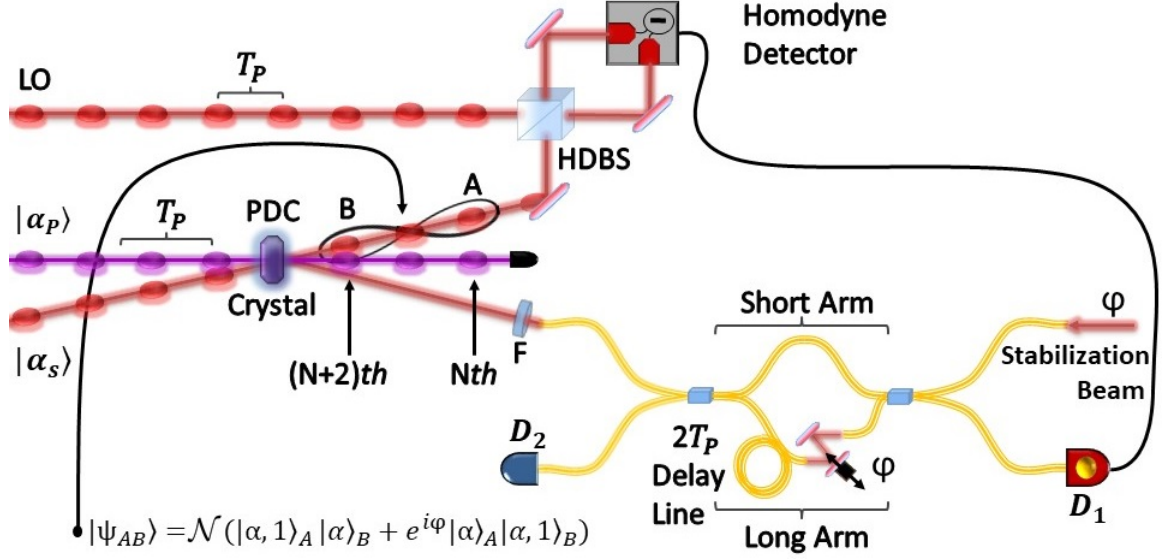
Figure 3.5: Schematic picture of the experimental apparatus used to generate and characterize the time bin version of the state of Equation (3.11).

Figure 3.5 shows a schematic picture of the generation and detection part of the setup that we used to characterize the state (3.11). The main components of the setup (laser, PDC crystal, Homodyne Detector) are the same used to realize the experiment described in the previous chapter (see Section 2.4). As in that case, for this experiment the temporal modes are defined by the local oscillator pulses. Each temporal mode corresponds to a different pulse emitted by the Ti:Sapphire laser. Thus, two consecutive temporal modes are separated by $12.5\,ns$ and each one is characterized by a gaussian profile of width $1.5\,ps$. The addition operation is again performed by exploiting the PDC process (see Section 2.2). In order to delocalize the $\hat{a}^\dagger$ operation between two temporal modes we have to erase the information about the time at which it has been performed. We can reach this goal by allowing the herald photon from the addition device to travel along two indistinguishable paths of different length towards the heralding detector (D_1). To do so, we coupled the idler mode of the PDC crystal, after the filters (F), to a *balanced Mach-Zehnder interferometer*[6]. If we set the time delay between its two arms equal to twice the time separation between two consecutive

_____

[6]In this context the adjective balanced is referred to the beam-splitters used to realize the interferometer. Both of them are set to have a balanced (50:50) splitting ratio. This note wants to clarify that, as it is common in other contexts, the adjective is not referred to the length of the arms, that, actually, are unbalanced in our setup.

laser pulses ($2T_p$), an idler photon detected by D_1 may have been generated by either the Nth or the (N + 2)th pump pulse, projecting the state of the two relative signal pulses in the state (3.11)[7]. The idea at the base of this technique is the same that we used in the case of the superposition of different operations applied to the same mode. In that case, we erased the information about what operation had been performed to implement the operator $(c_1\hat{O}_A + c_2 e^{i\varphi}\hat{O}'_A)$ each time we had a click in the heralding detector placed after the balanced beam-splitter (see Section 2.3). In the same way, for the temporal domain case, each trigger corresponds to the application of the operation $\frac{1}{\sqrt{2}}(\hat{a}_A^\dagger \otimes \hat{I}_B + e^{i\varphi}\hat{I}_A \otimes \hat{a}_B^\dagger)$. The phase of the superposition can be controlled acting on the relative phase between the two arms of the interferometer. For this experiment we built a fiber Mach-Zehnder interferometer that guarantees a better phase stability compared to a realization in air. It has to be noticed that $25\,ns$ of time delay ($2T_p$) between the two fiber paths correspond to $\approx 5.1\,m$ of length unbalancing[8]. This condition makes the interferometer very sensitive to phase fluctuations, requiring a careful stabilization. A small air-gap in the long arm allows us to finely tune the relative length of the two paths and to control the phase of the superposition (φ). As I showed in the previous section, this parameter strongly influences the entanglement properties of the state, switching from the maximally entangled odd version to the even one, much less correlated. To control this parameter we mounted a mirror on a piezo-stage placed in the air part of the interferometer. As shown in Figure 3.5, a weak portion of the main laser output is sent to the unused output port of the interferometer. We desynchronized the pulses of this beam with respect to the idler photons, ensuring no interactions between them. This allows us to actively control the superposition phase φ during the experiment by monitoring, with the detector D_2, and locking the intensity of interference fringes produced by the control beam. In order to reach this goal, I built a microcontroller-based circuit able to read and elaborate the signal from D_2, to produce the output voltage used to drive the piezo in the air part of the interferometer. The software, loaded on the microcontroller, incorporate a proportional–integral–derivative

---

[7]We chose to delocalize the addition operation over two nonconsecutive temporal modes to keep them well separated. We tested an $1T_p$ configuration for the interferometer, but due to the finite bandwidth of the HD, there was a small contamination of the mode B by the mode A. In the $2T_p$ configuration, the middle temporal mode is populated by an unmodified coherent state of the train injected in the PDC crystal. The unavoidable contamination has, in this case, the only effect to reduce the detection efficiency, easy to incorporate in the theoretical model.

[8]We use optical fibers with pure silica core, whose refractive index is 1.45332 at $800\,nm$ of wavelength.

(PID) control loop used to perform the active locking [76].

Losses and Noise

For a correct analysis of the experimental data that I will show in the next session, we have to consider the limits of the setup of Figure 3.5 that make the final state deviate from the theoretical one of Equation (3.11). We can start from the PDC process. As explained in Section 2.2, the pairs of photons emitted during this nonlinear process have to be carefully manipulated to ensure that the emission in the signal channel occurs in a specific target mode. I showed that our ability in this operation can be quantified by the η_{gen} parameter. With our setup, we are able to reach a generation efficiency of $\approx 92\%$. This means that, in the 92% of the realizations, we add the single photon to the right mode, while in the rest of the cases, we fail to perform the addition, leaving the target mode unchanged. We have to remember that, in this experiment, the signal modes are seeded with two coherent pulses of amplitude α in a separable state, and their density matrix can be expressed in the Fock basis as:

$$
\begin{aligned}
\hat{\rho}_\alpha &= |\alpha\rangle_A \langle\alpha| \otimes |\alpha\rangle_B \langle\alpha| \\
&= \sum_{n_A,n_B,m_A,m_B} \frac{e^{-2\alpha^2}\alpha^{(n_A+n_B+m_A+m_B)}}{\sqrt{n_A!n_B!m_A!m_B!}} |n_A\rangle |n_B\rangle \langle m_B| \langle m_A|.
\end{aligned}
\tag{3.17}
$$

Thus, the bipartite state, composed by the two temporal modes labeled A and B, is better described by the mixed state $\hat{\rho}_{AB}^{\eta_{gen}}$, than by the density matrix of Equation (3.16).

$$
\hat{\rho}_{AB}^{\eta_{gen}} = \eta_{gen}\,\hat{\rho}_{AB} + (1-\eta_{gen})\,\hat{\rho}_\alpha,
\tag{3.18}
$$

Since we are interested in the generation of the odd version of the state (3.11), we have to consider that the piezo-based system, used to control the superposition phase φ, introduces a small fluctuation of this parameter, as shown in Figure 3.6. The blue line on the left is the control signal, measured by the detector D_2 of Figure 3.5, used to stabilize the phase in our setup, during the "scan" part of the locking algorithm. In this part, the microcontroller used to drive the piezo looks for the maximum (Max) and the minimum (Min) of the interference fringes. Then, we can set the desired φ value by locking the interference signal at a value given by the formula:

$$
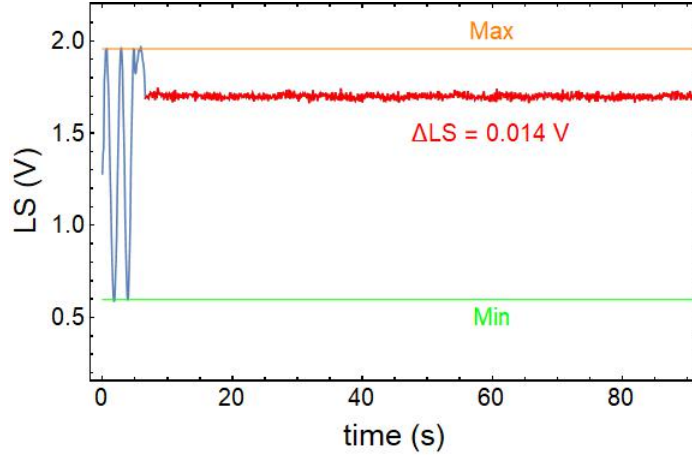LS(\varphi) = \frac{Max+Min}{2} + \frac{Max-Min}{2}\cos(\varphi+\varphi_{Off}).
\tag{3.19}
$$

Figure 3.6: Typical behavior of the signal used to lock the parameter φ.

The offset phase φ_{Off} is related to the offset between the phase measured while looking at the fringes produced by the control beam and those obtained from the counterpropagating idler states.

We calibrated this offset by injecting a more intense coherent beam, easier to be detected, in the interferometer port usually dedicated to the idler photons. We found that the minimum of the interference fringes produced by this beam can be obtained by locking the control signal to the phase $\varphi_{Lock} \approx \frac{3\pi}{10}$. Thus, the offset phase in Equation (3.19) is $\varphi_{Off} = \pi - \frac{3\pi}{10} = \frac{7\pi}{10}$. The right part (red one) of the graph 3.6 shows this signal during the "locking part". The residual noise of the locking signal can be translated to a mean phase error of $\Delta\varphi \approx \frac{\pi}{100}$. We can take into account this deviation from the ideal case by averaging the density matrix $\hat{\rho}_{AB}^{\eta_{gen}}$ over an angle of $\frac{\pi}{100}$ around $\varphi = \pi$.

Another source of error comes, again, from the the Mach-Zehnder interferometer. We saw that setting $\varphi = \pi$ corresponds to erasing the separable part of the state (3.11). This is exactly true if our Mach-Zehnder interferometer is perfect, with no losses and exactly balanced beam-splitters. In the real case, this type of imperfections lead to a visibility of the interference fringes, measured at the interferometer outputs, smaller than one. With our interferometer we measure a visibility of 0.996. This experimental deviation from the ideal case can be implemented, in the theoretical model describing the odd state generation, considering an α-dependent increase of the dark counts, or, equally, a decrease of the generation efficiency (see Section 2.2). To confirm this hypothesis, we measured the count rate of the trigger photons (the clicks from the detector D_1 of Figure 3.5) varying the mean photon number of the two modes that

compose our system. In the ideal case, this parameter should be constant. The experimental results are shown in Figure 3.7, confirming a linear increase of the trigger counts when the mean photon number of the injected coherent states increase.
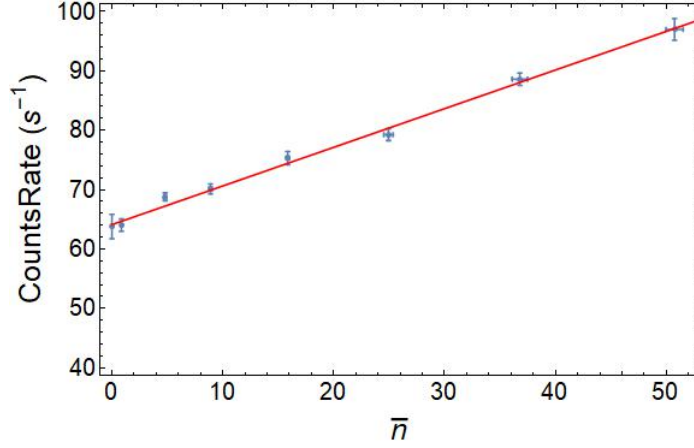

Figure 3.7: Behavior of the trigger count rate when increasing the macroscopicity of the state.

3.2.2 Tomography of the State

We characterized the state produced with our setup by performing a tomographic reconstruction of its density matrix. To do so, we have to perform independent quadrature measurements on both the temporal modes A and B. The acquisition system (Homodyne Detector and oscilloscope), described in Section 2.4.2, has been used to acquire the quadrature values. The resulting data set has the form:

$$\{y_A^i, y_B^i\} = \{\{x_A^i(\theta_A^j), \theta_A^j\}, \{x_B^i(\theta_B^j), \theta_B^j\}\} \tag{3.20}$$

using the same notation of Section 1.4. Here θ_A and θ_B are the phases of the quadrature measurements performed on each mode. Choosing again a phase reference in which the coherent states injected in the PDC crystal have real amplitude ($\alpha \in \mathbb{R}$), we can express θ_A and θ_B in terms of the global phase of the LO pulses train (θ_{gl}^{LO}) and the relative phase between the LO pulses correspondent to the signal modes A and B.

$$
\begin{aligned}
\theta_A &= \theta_{gl}^{LO} + \frac{\theta_{rel}^{LO}}{2} \\
\theta_B &= \theta_{gl}^{LO} - \frac{\theta_{rel}^{LO}}{2}.
\end{aligned}
\tag{3.21}
$$

I will show in the next subsection how we can control θ_{gl}^{LO} and θ_{rel}^{LO}. The density matrix of the state under analysis can be reconstructed acquiring 50000 quadrature values for 9 phase values spaced by $\frac{\pi}{8}$ in the interval $[0\,,\pi]$, for both θ_{gl}^{LO} and θ_{rel}^{LO}. Practically, to perform a full tomography reconstruction of the state under test we need to acquire 50000 quadrature values for each one of the 81 combinations of the two phase parameters θ_{gl}^{LO} and $\theta_{rel}^{LO} \in \{0, \frac{\pi}{8}, \frac{\pi}{4}, \frac{3\pi}{8}, \frac{\pi}{2}, \frac{5\pi}{8}, \frac{3\pi}{4}, \frac{7\pi}{8}, \pi\}$. To analyze this data set we used a two-mode extended version of the maximum likelihood algorithm described in Section 1.4 [23][77]. I will discus the results in the next session.

The Global Phase

As for the superposition phase φ, we can control the global phase θ_{gl}^{LO} using a piezo-mounted mirror and a reference signal. The electronic system used to drive the piezo is a copy of the one used to control the phase of the operator superposition, described in the previous section. As in the that case we have to evaluate the noise introduced on the phase θ_{gl}^{LO} by the locking circuit, that has been measured of the same order of the one measured for the parameter φ. The reference used to stabilize the global phase to different values is the DC component of the HD signal. This signal presents the interference fringes due to the interaction between the local oscillator pulses and the injected coherent states in the HDBS. As in the case of the superposition phase, different values of this signal correspond to different values of θ_{gl}^{LO}, allowing us to actively stabilize it. For example, locking to the maximum of the reference signal means that the LO and the injected coherent states have the same phase. We will use this condition to fix the phase reference, so it will correspond to $\theta_{gl}^{LO} = 0$. We can obtain the other global phase values according to the relation

$$LS(\theta_{gl}^{LO}) = \frac{Max + Min}{2} + \frac{Max - Min}{2}\cos(\theta_{gl}^{LO}),\tag{3.22}$$

that is the analogue of Equation (3.19).

The Relative Phase

To control the θ_{rel}^{LO} parameter, we need to change the relative phase between two LO temporal modes separated by $25\,ns$. In this case, we need a device much faster than a piezo[9]. We placed, along the LO path, an ultrafast electro-optic modulator

---

[9]Typically, the maximum frequency with which a piezo-mounted mirror can be moved is $10\,KHz$. To control θ_{rel}^{LO} we need a phase modulation of the LO pulses at $20\,MHz$, so a piezo system can not be used.

(EOM) made by Thorlabs (EO-PM-NR-Cx). The core of this device is a birefringent crystal whose extraordinary refractive index can be modulated using a voltage signal (see Appendix A for more details). Letting the LO pass through this crystal we can modulate its phase. The version of phase modulator that we used can be driven from DC up to $100\,MHz$. After this component, the LO acquires a phase shift proportional to the amplitude of the electrical signal applied to the RF port [78]. To obtain the LO phase modulation that we need we used a sinusoidal modulation voltage of period $4T_p$ ($\omega_{drive} = \frac{2\pi}{4T_p} = \frac{\omega_{RR}}{4}$, where ω_{RR} is the repetition frequency of our laser), synchronized with the train of optical pulses emitted by the laser. Figure 3.8 explains this concept.
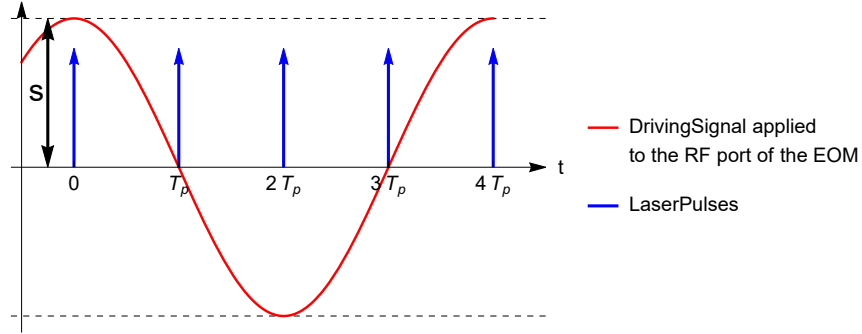
Figure 3.8: EOM driving signal strategy used to control the relative phase between two local oscillator pulses separated by $25\,ns$.

The blue arrows represent the LO pulses, while the red line is the driving signal. In this way, the pulse at time 0 and the one at time $2T_p$ acquire a relative phase shift (θ_{rel}^{LO}) proportional to the modulation depth s, while the pulses at time T_p and $3T_p$ exit the EOM with the phase unchanged. Using the phase reference defined in the previous paragraph, we can consider that the pulse at time 0 acquires a phase shift of $\frac{\theta_{rel}^{LO}}{2}$ respect to the corresponding temporal mode of the signal, while the pulse at time $2T_p$ will be shifted of $-\frac{\theta_{rel}^{LO}}{2}$ respect to its corresponding signal mode. To generate the driving signal, we used the AD9959 Direct Digital Synthesizer (DDS) [79]. This device can provide a sinusoidal voltage synchronous with an external reference. From the output of the laser mode-locker we can obtain a signal synchronous with the pulses train (at frequency ω_{RR}), suitable for the synchronization. Another important feature of this DDS is the possibility to arbitrary set the frequency and the phase of its outputs, that, however, remain in phase with the reference signal. Therefore, we can obtain the EOM driving signal at frequency $\frac{\omega_{RR}}{4}$ and we can also compensate the phase shift between this signal and the LO pulses due to the overall electronic circuit. In order to

produce the high voltage amplitude ($\approx 150\,V$) required to produce the desired phase shift ($\theta_{rel}^{LO} = \pi$) at a frequency of $20\,MHz$, we built a resonant circuit after the RF port of the EOM, as shown in Figure 3.9.
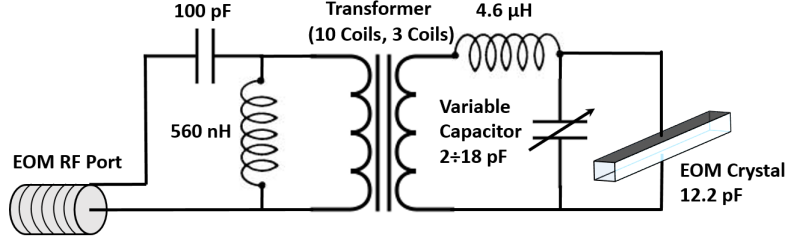

Figure 3.9: Resonant circuit built inside the EOM. This circuit has been built to have a resonance frequency of $\frac{\omega_{RR}}{4}$, with a factor of merit of ≈ 20. This trick reduces the amplitude of the modulation signal required to induce a π-phase shift.

The left side of the circuit, including the transformer, is an impedance matching circuit, needed to avoid back reflections of the driving signal. The right side determines the resonant frequency, set to $\frac{\omega_{RR}}{4}$ and finely tuned using the variable capacitor. Thanks to a factor of merit of the overall circuit (Q) of approximately 20 we can obtain a π phase shift with a driving signal of amplitude around $5V$, that is easier to generate at high frequencies. The overall scheme used to control θ_{rel}^{LO} is summarized in Figure 3.10.
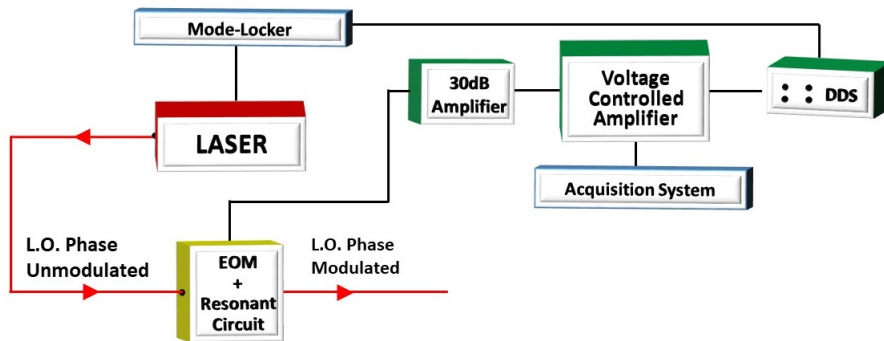
Figure 3.10: The overall phase control scheme for the LO beam.

The voltage controlled amplifier, following the DDS, has a variable gain that can be set from 0 to 10. We used this device to control the modulation depth s. The procedure used to calibrate this setup is shown in Appendix E.

3.2.3   Results

Using the methods just described to control the global (θ_{gl}^{LO}) and the relative (θ_{rel}^{LO}) phase of the LO pulses correspondent to the signal modes A and B, we performed a complete tomography reconstruction of the odd state of Equation (3.11). We set $|\alpha|^2 = 1$ for all the coherent states injected in the PDC crystal[10]. The overall data acquisition required more then 48 hours to be completed. Unfortunately, our setup is not stable enough to perform a so long measurement. Indeed, the fidelity[11] of the reconstructed density matrix respect to the ideal odd state, for which we considered the effects of the non-unitary generation and detection efficiency $(\eta_{gen} = 0.92, \eta_{det} = 0.60)$, is just 0.36. Beyond that, we have to consider that also the maximum likelihood algorithm takes a long time to analyze the data (more then 100 hours). This is because the number of density matrix elements needed for a faithful representation of the odd state with $|\alpha|^2 = 1$ is almost 2500. It is worth noting that this number grows very fast with the mean photon number of both modes; for instance, the density matrix of a state of the form (3.11) with $\bar{n} = 50$ photons requires 30 millions density matrix elements. Since this huge amount of elements prevents us to proceed with full reconstruction of the density matrix for macroscopically populated modes, we have to develop other strategies to quantify the amount of entanglement in the generated states.

Global Phase Averaged

The first method that we decided to test aims to reduce the number of density matrix elements and the duration of the acquisition time by averaging the global phase of the LO pulses. From a practical point of view this means that we analyze the state produced after the single photon delocalized addition by performing a partial tomographyc reconstruction. We acquire 50000 quadratures values, for each mode, for 9 different values of θ_{rel}^{LO}, while the global phase θ_{gl}^{LO} is randomized by applying a sinusoidal modulation, with frequency of $10\,KHz$, to the piezo used to control this parameter (see Section 3.2.2). This modulation is not synchronized with the acquisition system, so,

---

[10]See Appendix C for the details about the method used to calibrate α.

[11]It is a parameter used to quantify how much two quantum states are close to each other. If ρ_{AB}^{th} is the theoretical density operator and ρ_{AB}^{M} is the measured one, we have:

$$Fidelity = \left[Tr\{\sqrt{\sqrt{\hat{\rho}_{AB}^{th}}\hat{\rho}_{AB}^{M}\sqrt{\hat{\rho}_{AB}^{th}}}\}\right]. \qquad (3.23)$$

This parameter is 1 for two identical state, while it is 0 if they are orthogonal.

each time a trigger event occurs[12], the consequent quadrature measurement is performed at a random θ_{gl}^{LO} phase. It is evident that, scanning just one phase parameter the total acquisition time needed for the measurement is roughly the square root of the time needed for the full tomography. This allows us to obtain a good stability of the overall apparatus during the measurements. Furthermore, a great advantage of this technique is that only the density matrix elements that satisfy the condition $n_A - m_A + n_B - m_B = 0$ are different from zero, all the others are averaged to zero. Figure 3.11 shows the reduction of the number of density matrix elements needed to represent the states measured using the θ_{gl}^{LO} averaged method respect to a full tomographyc reconstruction.
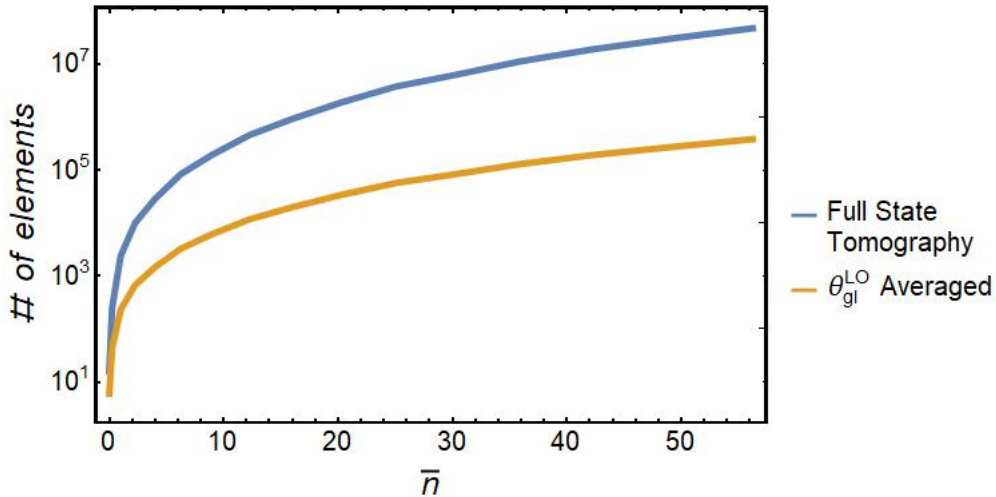
Figure 3.11: Comparison between the number of density matrix elements needed for a faithful representation of the odd state with and without averaging the global phase.

The average operation, of course, also changes the entanglement properties of the reconstructed states. Figure 3.12 reports the theoretical NPT behavior for the odd and even state expected performing the θ_{gl}^{LO} averaged partial tomography.

---

[12]See Appendix D for more details about the trigger used for this experiment.
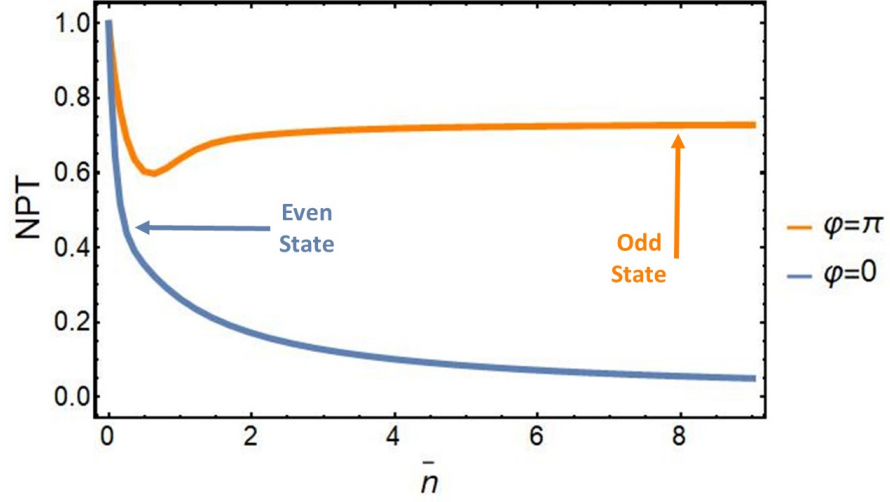
Figure 3.12: Theoretical behavior of the NPT value for the odd and even state measured averaging the LO global phase.

It is interesting to note that NPT of the odd state is lowered by global phase averaging respect to what shown in Figure 3.3, but the entanglement is still well preserved for large mean photon numbers of the modes A and B. We performed the measurement just described of the odd state for $\bar{n} = 0$, 0.29, 1.29, 5.44. The relative NPT values are represented by the green dots in Figure 3.13. Also in this case we must pay close attention to the experimental imperfections that inevitably occur in the generation and detection of these states for a correct interpretation of the results. For the generation part the same conclusion obtained in Section 3.2.1 hold. The imperfections induced by the detection part can be accounted by the Equation (1.56). Considering that the Homodyne Detector used to collect the quadrature values is the same used in the experiment described in Section 2.4.2, and that we measured a mode matching efficiency of 0.92, we obtain an overall detection efficiency of $\eta_{det} = 0.60$. The good agreement between the experimental points and the theoretical model including both the generation and detection efficiency confirms our prediction about the entanglement features of the odd state.
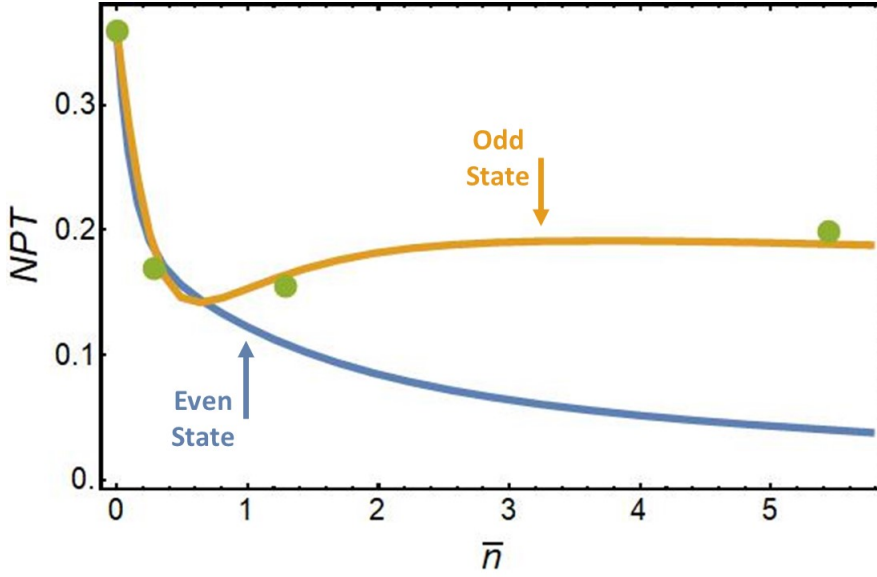
Figure 3.13: Experimental NPT (green dots) for the generated odd state as a function of mean photon number ($\bar{n}$) and calculated NPT (lines) for the odd (yellow) and even (blue) state measured by averaging the global phase.

This result tells us that, with the available technology, we are able to produce optical states which degree of entanglement slowly decrease increasing their mean photon number. However, investigating the macroscopic regime exploiting this technique is not possible. Despite the number of density matrix elements is considerably reduced with respect to full tomography, the maximum mean photon number that can be reached is about 6 due to bounded computational resources needed for the reconstruction algorithm[13]. I will show a technique suitable to overcome this problem in the next part of this session.

It is interesting to note that the discorrelation properties, discussed in Section 3.1.2 for the ideal state of Equation (3.11), are evident also performing the partial tomographic reconstruction with the method just described. The joint photon number probability distributions for the modes A and B, obtained from the density matrix measured setting $\bar{n} = 5.44$, is reported in Figure 3.14.

---

[13]A parallel code, implementing the two mode version of the maximum likelihood algorithm presented in Section 1.4, takes more than 60 hours to reconstruct a $\bar{n} = 5$ odd state, running on a 8-core 3GHz Xeon processor.
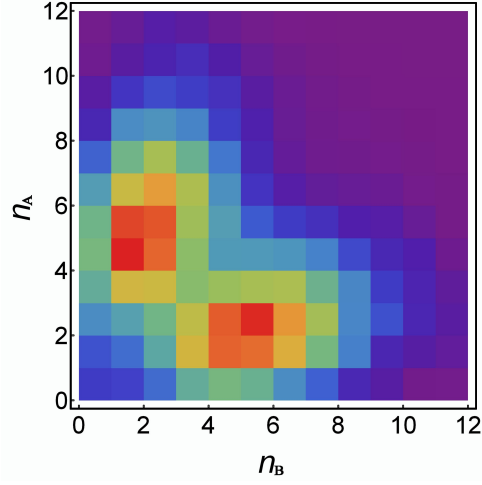
Figure 3.14: Experimental discorrelation property of the odd state with $\bar{n} = 5.44$, to be compared with Figure 3.4.

Global Phase Locked

As explained at the beginning of this chapter, applying two identical displacement operators $(\hat{D}_A(\alpha) \otimes \hat{D}_B(\alpha))$ on both the modes of a bipartite entangled state doesn't change its entanglement properties. In our case, choosing the proper amplitude and phase of the displacement operator, precisely the same amplitude and opposite phase respect to the coherent states injected in the signal mode to generate the state (3.11), we can remove the macroscopic component of the state. If we do this before the detection stage[14], we obtain the entanglement behavior of the initially macroscopic state by measuring the density matrix of the microscopic one. In this way we can use an Hilbert space of dimension 2, spanned by the Fock states $|0\rangle$ and $|1\rangle$, to described it, drastically reducing the computational resources needed for its characterization. Such an approach has been proposed [80] and tested [81] by Gisin et al. This method has been criticized due to the fact that, actually, no macroscopic states are measured.

To overcome the problems of the method previously proposed (Global Phase Averaged) we decided to exploit the advantages of the *back-displacement* $(\hat{D}_A(-\alpha) \otimes \hat{D}_B(-\alpha))$, but we choose to apply this operator in a post-processing step by applying a numerical high-pass filter to the quadrature values measured by the modes A and B macroscopically populated. In practice we performed a different kind of partial tomography respect to the Global Phase Averaged method. Even in this case we acquired 50000

---

[14]An optical implementation of the displacement operator can be realized using a beam-splitter and an auxiliary coherent state [80].

quadrature values for 9 different LO relative phase (θ_{rel}^{LO}) for both the temporal modes, but, this time, the global phase (θ_{gl}^{LO}) was locked to 0 during all the acquisitions. This measurement scheme can be graphically illustrated using the phasor diagram formalism introduced in Section 1.3.2. In this context, the measurements performed to analyze the produced state via the Global Phase Locked method are represented in Figure 3.15.
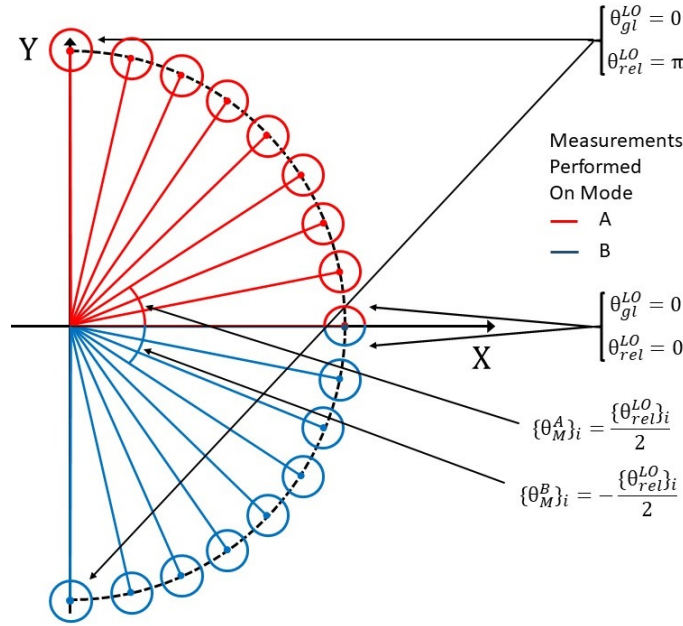

Figure 3.15: Phasor diagram representing the measurements performed to realize the Global Phase Locked analysis.

The red part of this graph represents the measurements performed on the mode A, while the blue part represents the ones performed on the mode B. As explained in Section 3.2.2, considering that θ_{gl}^{LO} is always locked to 0, each measurement angle can be obtain by the relations

$$\left\{ \theta_M^A = \frac{\theta_{rel}^{LO}}{2} \ , \ \theta_M^B = -\frac{\theta_{rel}^{LO}}{2} \right\}. \tag{3.24}$$

Contrary to the Global Phase Averaged method, with this measurement scheme no density matrix elements are reduced to zero, but in this way the post selection application of the back-displacement operator is easy to implement. Indeed, it is sufficient

to subtract, from each quadrature data set[15], its mean value.

$$\{y_A'^i, y_B'^i\} = \{\{x_A^i(\theta_A^j) - \bar{x}_A(\theta_A^j), \theta_A^j\}, \{x_B^i(\theta_B^j) - \bar{x}_B(\theta_B^j), \theta_B^j\}\} \tag{3.25}$$

The validity of this method can be experimentally proved by looking at the correlations between the quadrature values relative to the modes A and B measured with our scheme

$$Cor(\alpha, \theta_{rel}^{LO}) = \langle \hat{X}_A(\theta_{rel}^{LO}) \cdot \hat{X}_B(\theta_{rel}^{LO}) \rangle. \tag{3.26}$$

If we don't apply the numerical displacement the measured correlation follow, at least for small values of θ_{rel}^{LO}, the theoretical behavior

$$Cor(\alpha, \theta_{rel}^{LO}) = \langle \Psi_{AB}^{odd}(\alpha)| \hat{X}_A(\theta_{rel}^{LO}) \cdot \hat{X}_B(\theta_{rel}^{LO}) |\Psi_{AB}^{odd}(\alpha) \rangle, \tag{3.27}$$
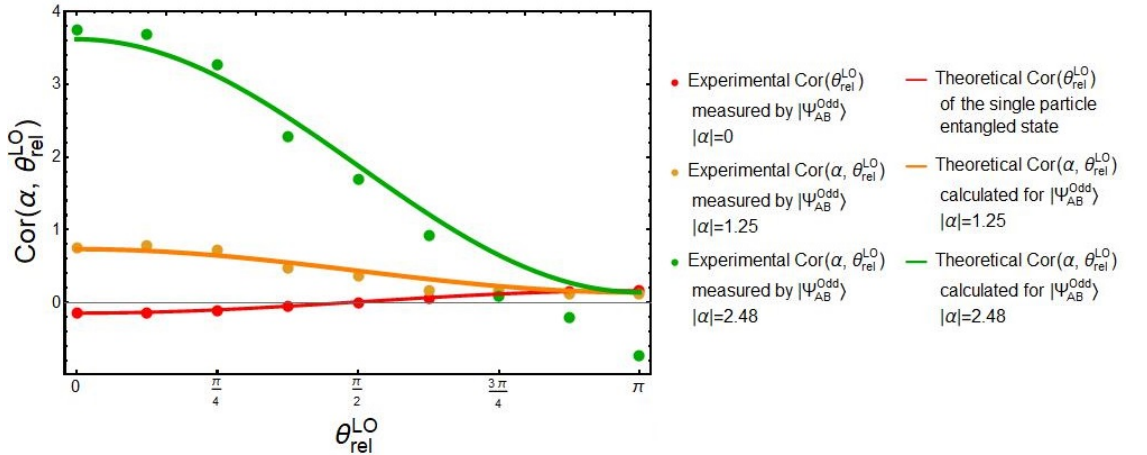
as it is shown in Figure 3.16.

Figure 3.16: Correlations between the quadrature values of the mode A and B obtained by measuring the entangled odd states produced with our setup for different values of α.

In Figure 3.17 are instead reported the quadrature correlations obtained after the numerical displacement applied to the same data used in Figure 3.16. In this case we have a good agreement between the post-processed experimental data and the

---

[15]To avoid misunderstanding I recall that a data set correspond to 50000 quadrature values acquired for a fixed value of θ_{rel}^{LO}.

theoretical correlation behavior of the single particle entangled state, that is exactly
what we expect applying the back-displacement to the odd state.

$$\hat{D}_A(-\alpha) \otimes \hat{D}_B(-\alpha) \left|\Psi_{AB}^{odd}(\alpha)\right\rangle = \frac{1}{\sqrt{2}} \Big(|1\rangle_A |0\rangle_B - |0\rangle_A |1\rangle_B \Big). \qquad (3.28)$$
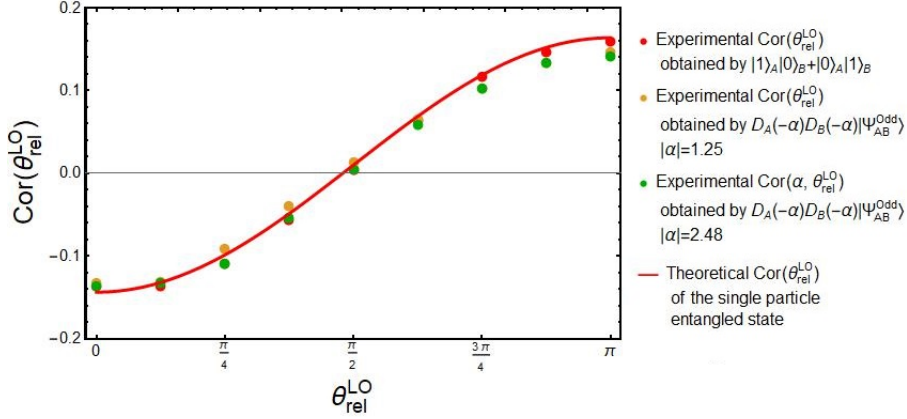

Figure 3.17: Correlations between the quadrature values of the mode A and B obtained
by applying the numerical back-displacemnt to the $|\Psi_{AB}^{odd}(\alpha)\rangle$ states produced with our
setup, for two values of α.

To optimize the numerical displacement and to understand the source of the devia-
tion from the theoretical curve of the data in Figure 3.16, we performed the same
measurements described in Figure 3.15 on a separable, two modes, coherent state
$|\Phi_{AB}\rangle = |\alpha\rangle_A \otimes |\alpha\rangle_B$. The experimental values of the correlation parameter (3.26) are
shown in Figure 3.18 and present the same deviation, observed in Figure 3.16, from
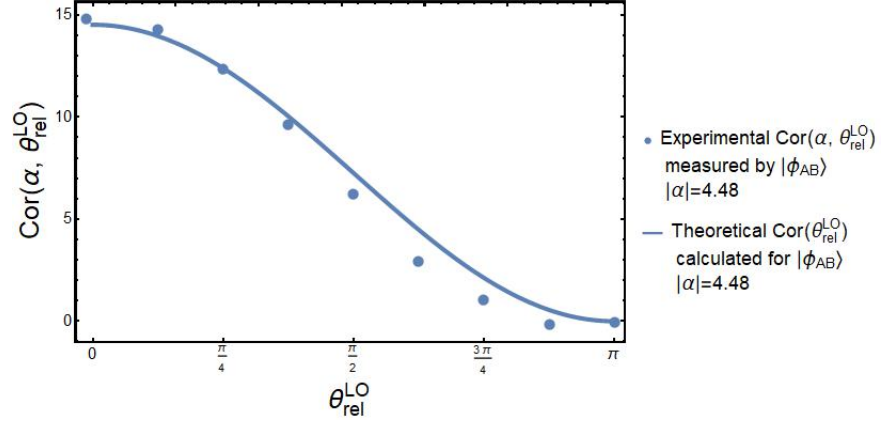the theoretical behavior when θ_{rel}^{LO} approach to π.

Figure 3.18: Correlations between the quadrature values of the mode A and B obtained by measuring the state $|\Phi_{AB}\rangle$.

This anomaly can be explained considering an extra noise in the quadrature measurements, dependent on θ_{rel}^{LO}. If we look at the variance of the quadrature data used to realize Figure 3.18, this phase dependent noise is evident, as it is shown in Figure 3.19[16].
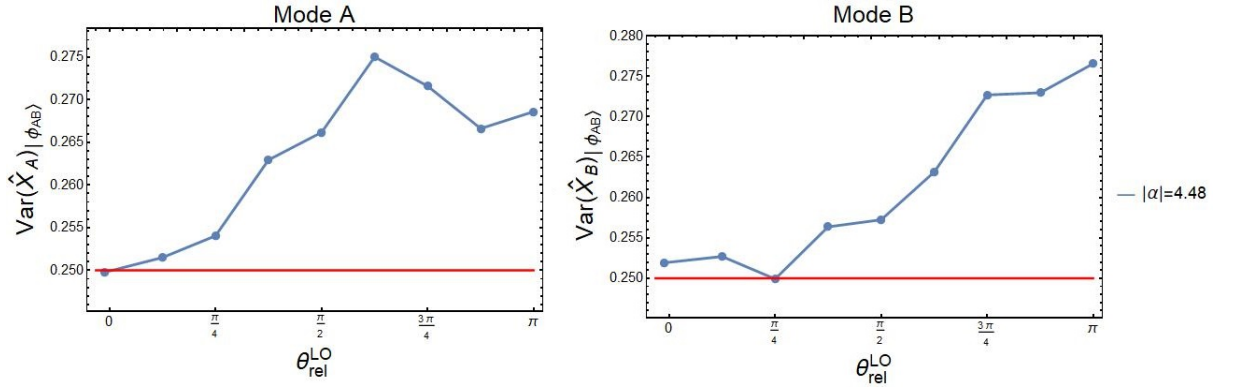

Figure 3.19: Variance of the quadrature values acquired by measuring the state $|\Phi_{AB}\rangle$ for the 9 values of θ_{rel}^{LO}, for the mode A (left) and B (right).

---

[16]It is useful to remember that a coherent state is a minimum uncertainty state (see Section 1.2). This means that the variance of a quadrature measurement performed on a coherent state should be constant respect to α and to the measurement phase, and, using our notation, it should be equal to $\frac{1}{4}$ (red line in figure). The phase dependent increment of the quadrature distribution variance is the signature of the presence of a phase dependent noise.

From the measurements performed on the state $|\Phi_{AB}\rangle = |\alpha\rangle_A \otimes |\alpha\rangle_B$ we also understood that this extra noise is also α-dependent. In Figure 3.20 I show the variance of the quadrature measurement performed at various coherent amplitude. Each point corresponds to the variance calculated on all the quadrature data acquired according to the scheme of Figure 3.15 for each value of α[17].
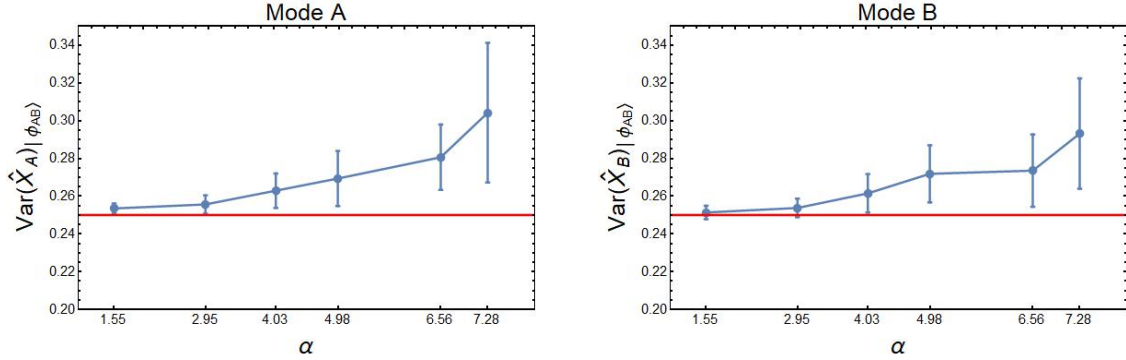

Figure 3.20: Variance of the quadrature values acquired by measuring the state $|\Phi_{AB}\rangle$ for different values of α, respectively for the mode A (top) and B (bottom). The red line represents the theoretical value of the quadrature variance for measurements performed on coherent states.

To understand the origin of this extra noise we have to remember the modulation strategy used to control the θ_{rel}^{LO} phase, illustrated in Figure 3.8. The modes A and B, on which we delocalized the single photon addition to generate the state (3.11), correspond to the local oscillator pulses at time 0 and $2T_p$ of that figure[18]. As justified in Section 3.2.1, we choose to leave an unused optical mode between A and B. The phase of its relative LO pulse is not modified passing through the EOM, for all the modulation depths s[19]. As explained in Section 2.4.2, with our acquisition system we record, for each trigger event, the homodyne signal corresponding to 4 modes $(A \rightarrow T = 0,\ A' \rightarrow T = T_p,\ B \rightarrow T = 2T_p,\ B' \rightarrow T = 3T_p)$. If we set a modulation depth corresponding to $\theta_{rel}^{LO} = 0$, the mean value of the homodyne signal is the same for all the 4 recorded modes, equal to $\langle \hat{H}_-\rangle_{A,A',B,B'} = |\alpha|$. If instead we set $\theta_{rel}^{LO} = \pi$, the mean value of the signal corresponding to the modes A' and B' is the same, while the one of the modes A and B is 0. This means that our HD have to switch the output

[17]The error bar is the standard deviation of the quadrature variance over the 9 values of θ_{rel}^{LO}.

[18]The origin of the time axis is coincident with the arrival of the trigger event from the detector after the MZ interferometer that herald the application of the delocalized single photon addition.

[19]See Section 3.2.2 for more details.

signal mean value from 0 to $|\alpha|$ in a time smaller than $T_P = 12.5\,ns$. The bandwidth of our detector ($100\,MHz$) doesn't full satisfy this request, causing the extra-noise shown in Figure 3.19 and 3.20.

We found that, optimizing the numerical back displacement, it is possible to erase this noise. We can suppose that the apparatus limitations just discussed produce a fluctuation of the quadratures mean value, faster than the time needed to acquire the 50000 quadrature values composing the data set $\{x_A^i(\theta_A^j), x_B^i(\theta_B^j)\}$, for each $\{\theta_A^j, \theta_B^j\}$. Considering that the this data set is time ordered, we can partition it in faster acquired (smaller) ensembles and calculate from each of them $\bar{x}_A(\theta_A^j)$ and $\bar{x}_B(\theta_B^j)$ used in Equation (3.25) to back-displace the quadrature values. From each partition we subtracted its relative mean values, that, in this way, is less sensitive to the fast fluctuations. Practically, the finite bandwidth of the HD introduce noise in the detection of the coherent states amplitude, with the back displacement we remove this parameter from the state. Adjusting the length of the ensemble used to perform this operation (DispBin) we can reduce the amplitude fluctuations and so the extra noise. To adjust the DispBin parameter we noticed that, as I explained in Chapter 1, also the vacuum state $|0\rangle_A \otimes |0\rangle_B$ is a minimum uncertainty state, with the same quadrature fluctuations of the state $|\Phi_{AB}\rangle$. We reduced the DispBin parameter until we reach the same quadrature variance obtained by performing the measurements of Figure 3.15 on the vacuum state[20]. Some example steps of the optimization are shown in Figure 3.21.
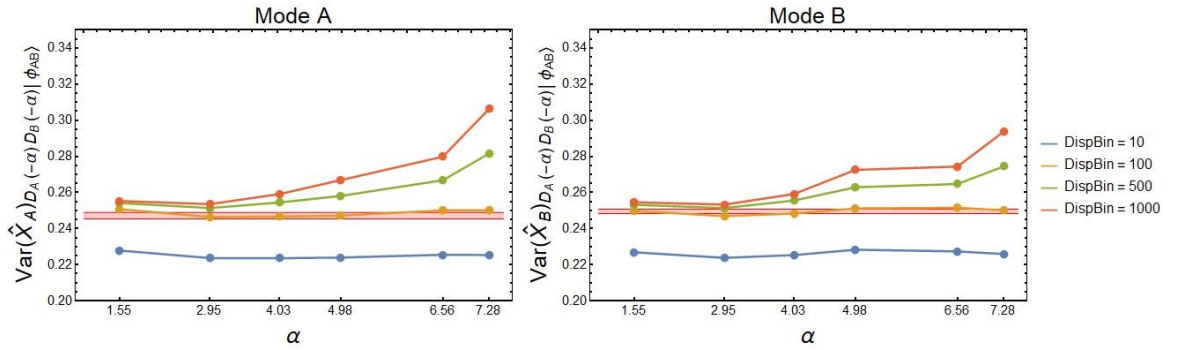

Figure 3.21: Variance of the quadrature measurement performed on the state $|\Phi_{AB}\rangle$ after the application of the back-displacement operator for different values of DispBin. The red bar is the quadrature variance obtained measuring the state $|0\rangle_A \otimes |0\rangle_B$.

Practically we optimized the DispBin parameter to obtain, after the application of

---

[20]We simply obtained the state $|0\rangle_A \otimes |0\rangle_B$ by blocking the signal port of the HDBS with an opaque material.

the numerical back-displacement on the data measured from the state $|\Phi_{AB}\rangle$, the same results obtained from the measurements performed on the state $|0\rangle_A \otimes |0\rangle_B = \hat{D}_A(-\alpha) \otimes \hat{D}_B(-\alpha) |\Phi_{AB}\rangle$. From this analysis we found that a binning of 100 is optimal to perform the numerical back-displacement.

We used the independently optimized back-displacement to analyze the data measured from the odd version of the state (3.11) generated with our setup. The entanglement behavior obtained using the Global Phase Locked method is reported in Figure 3.22. The red line is the NPT value that we expect for the odd state considering a constant generation efficiency (η_{gen}) of 0.92 (see Section 3.2.1 for the details), and a detection efficiency of 0.60 (see Section 1.3.2), while the blue line is the entanglement behavior for the even state obtained from the same model.
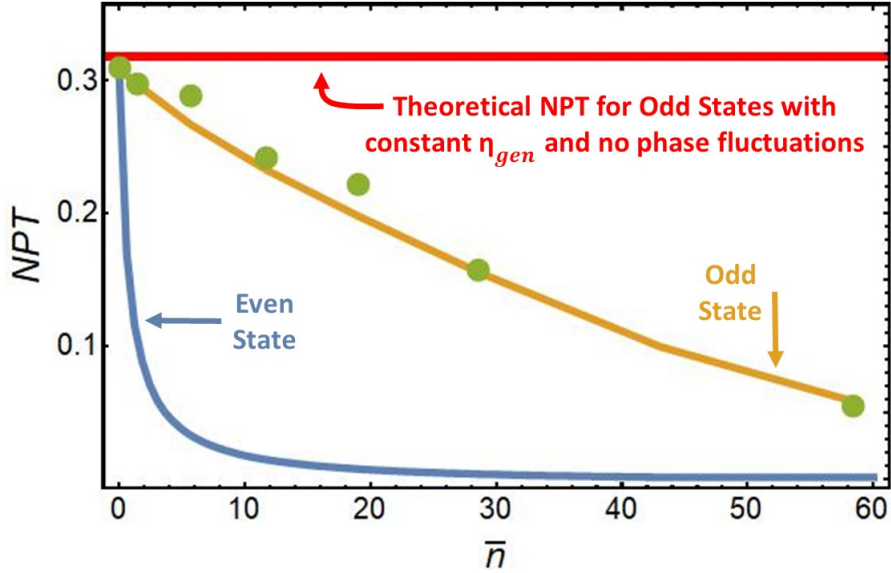

Figure 3.22: Experimental NPT (green dots) for the generated odd state as a function of mean photon number ($\bar{n}$) and calculated NPT (lines) for the odd (yellow) and even (blue) state.

The dependence of the measured NPT values (green dots in the figure) from the mean photon number of the two modes is caused both by the θ_{gl}^{LO} noise discussed in Section 3.2.2 and the one associated to the superposition phase φ (see Section 3.2.1), and by the dependence of the generation efficiency by the mean photon number of the modes A and B, as discussed in Section 3.2.1. The orange line is the NPT curve obtained by a model including all these effects. The good agreement between the experimental points and the theoretical model confirms that the class of states in Equation (3.11)

can be used to investigate the entanglement properties of macroscopic systems. Indeed, the data in Figure 3.22 clearly show the presence of entanglement for bipartite systems with up to 60 photons per mode.

From this experiment we can conclude that the Single Photon Delocalized addition presented in Section 3.1 can be use to generate entanglement between macroscopically populated optical systems initially prepared in a separable state. We also investigated the entanglement properties of a sub-class of state that can be produced with this technique, the odd version of the state (3.11). With this experiment we underlined the experimental fragilities that may prevent the study of the entanglement in macroscopic systems. To be able to further increase the mean photon number per mode we have to improve the interference fringe visibility of the Mach-Zehnder interferometer used to delocalize the addition operation, removing the dependence of the generation efficiency from the mean photon number. The main change needed to improve the detection part regards the spectral bandwidth of the homodyne detector used to collect the quadrature values from the state under test. Enlarging this parameter allows us to reduce the quadrature extra-noise characteristic of the Global Phase Locked method.

Future perspectives   In the just described experiment we used the NPT to quantify entanglement. I showed that to calculate this parameter we need to know the density matrix that describe the state we want to test. We saw that the full tomography needed to reconstruct the desired density matrix is very demanding from the experimental point of view, so demanding that in many cases it requires to find simplified measurement strategy (partial tomography). For this reason, along the years, many efforts have been devoted to develop "cheaper" methods to discriminate between separable and entangled states. From the definition (3.4), we can see that the space of all separable states is a convex space[21]. It is possible to demonstrate that, if $\hat{\rho}_{AB}$ is a state in such a space, it is mapped into a positive operator (a physical state) by a map of the form $(\hat{I}_A \otimes \hat{\Lambda}_B)$, where $\hat{\Lambda}_B$ is a positive map[22] acting on the subsystem B, while $\hat{I}_A$ stands for the identity operator of the subsystem A. The main idea, first developed by Terhal [82], is that this property of the separable states doesn't hold for entangled states i.e., if a state $\hat{\rho}^*$ is entangled, then there exists a positive map Λ_B such that

---

[21]A space is convex if each of its elements can be expressed as a linear combination of its base vectors where all coefficients are non-negative and sum to 1.

[22]Λ is a positive map if it maps a positive operator $\hat{O}$ into a positive operator. This means that, if $\hat{O}$ has non-negative eigenvalues, then $\hat{O}' = \Lambda(\hat{O})$ also has none.

$(\hat{I}_A \otimes \hat{\Lambda}_B)\hat{\rho}^*$ is not positive. This implies that it is always possible to find an Hermitian operator $\hat{W}$ such that

$$Tr\{\hat{W}\hat{\rho}\} \geq 0 \qquad\qquad Tr\{\hat{W}\hat{\rho}^*\} < 0$$
$$\forall \hat{\rho} \in \{separable\, states\} \qquad \forall \hat{\rho}^* \in \{entangled\, states\} \qquad (3.29)$$

Such an operator was defined as an *Entanglement Witness* by Terhal. $\hat{W}$ is Hermitian, so it can be measured. The main virtue of this kind of observables is that they allows an experimental detection of entanglement. On the other hand, given a general entangled state, to find the witness capable to detect it is an hard task. Referring to Figure 3.23, if the entangled state $\hat{\rho}^*$ (represented by the black dot in figure) is detected by the witness $\hat{W}_{(1)}$, it will not be detected by $\hat{W}_{(2)}$.
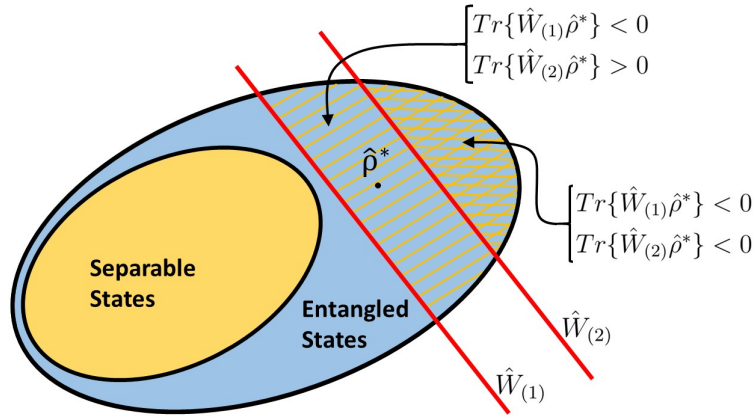

Figure 3.23: Geometric representation of entanglement witnesses.

To solve this problem, numerical methods and general strategies to find suitable entanglement witnesses have been studied [83][84][85], but, until the present days, they are not very efficient.

In the future we will look for the existence of a properly tailored entanglement witness capable to detect the entanglement of the state 3.11. Our hope is to reduce the complexity of the measurement strategy in order to further increase the mean photon number of the two modes of the state 3.11.

Conclusions

In the first chapter of this thesis I introduced the main concepts of quantum optics, focusing on the formalism needed to explain the experimental techniques presented next. I paid particular attention to Homodyne Detection due to its central role during my PhD work. Indeed, all the optical states discussed and experimentally generated in this thesis were characterized performing homodyne measurements and tomographic reconstructions of their density matrix. Then, I described the experimental implementation of the main tools in the field of state engineering. After a theoretical review of the techniques used to realize the creation and the annihilation operators, I showed a general scheme used to implement more sophisticated operations, based on their superposition. I showed an experiment in which, exploiting the superposition of different sequences of $\hat{a}$ and $\hat{a}^\dagger$, we were able to emulate the effect of a strong Kerr nonlinearity on a quantum state of light. These results show that measurement-induced operations, although working in a non-deterministic way, can be used to implement transformations forbidden with the materials available today, and can thus pave the way for implementation in quantum computational schemes.

Finally, I investigated the properties of multipartite optical systems, focusing on the phenomenon of entanglement. Also in this case, I described an experimental technique useful to manipulate the state of such kind of systems. I showed that the so-called Delocalized Single-Photon Addition can turn the initially separable state of a bipartite system into a maximally-entangled one, independently of how macroscopic the initial state was. Then, I presented two different techniques to detect the amount of entanglement generated by delocalizing the addition of a single photon between two modes populated by states of increasing mean photon number. Despite the experimental difficulties involved in the accurate quantum tomographic measurement of macroscopic systems, we were able to detect substantial levels of entanglement also between two different light states each containing up to 60 photons. The results obtained from this experiment were preliminary published on arxiv [86] and presented during the 2018

IEEE Photonics Society Summer Topical Meeting [87].

Appendix A

Birefringence

During the course of this thesis the well known phenomenon of birefringence has been widely used in various experimental situations. Both the techniques used to realize the annihilation and creation operators take advantages from this effect. For the first one we used an *half wave plate* (HWP), a birefingence based optical component, to replace the beam-splitter in the polarization implementation of this operator (see Section 2.1 for more details). Thanks to this effect we could also reach the phase matching condition necessary for an efficient implementation of the $\hat{a}^\dagger$ operator (see Section 2.2 for more details). Also the working principle of the *electro-optic modulator* used to control the LO phase as explained in Section 3.2.2 can be explained in therms of a birefingence effect.

A material is said birefringent when it shows different optical properties respect to differently polarized light, in particular when the refractive index is depending on the directions of polarization and propagation of the light beam, as a consequence of a natural or induced anisotropy. We will focus on a particular type of birefringent crystal, said uniaxial, in which the refractive index takes different values if taken along the direction defined by a particular crystal axis or in its perpendicular plane. This particular axis is usually called *extraordinary axis* or optical axes. To simplify the use of this type of crystals in an optical experiment they are often cut so that the optical axis is parallel to the input face, as shown in Figure A.1.
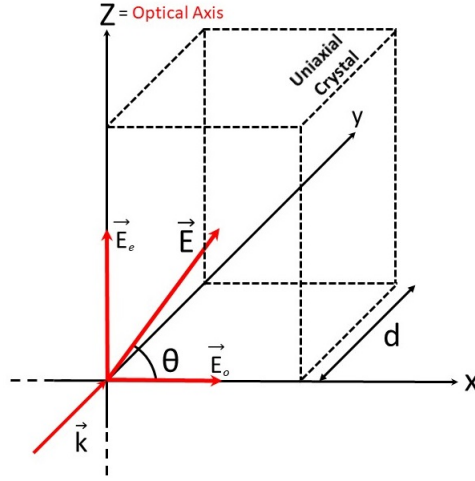
Figure A.1: Schematic pictures of an uniaxial birefingent crystal. $\vec{k}$ and $\vec{E}$ represent respectively the wave vector and the electric field of the light incident on the crystal.

We can decompose the electric field of the beam injected in such a crystal in two polarization components, the one parallel to the optical axis will fill a refractive index (n_e), different from the one filled by the x component (n_o). The two polarizations accumulate different phase delays as it is clear from Equation (A.1), that describes a classical electric field propagating in the crystal.

$$\mathbf{E}(y > 0) = E_0 e^{i\omega t} e^{i2\pi n_o \frac{y}{\lambda}} (\mathbf{i}\cos(\theta) + \mathbf{k}e^{i\Delta\phi}\sin(\theta)), \qquad \Delta\phi = 2\pi(n_e - n_o)\frac{y}{\lambda}, \ (A.1)$$

where $\mathbf{i}$ and $\mathbf{k}$ are the versors of the x and z axis respectively. This effect can be used to separate them, as in a Polarizing Beam-Splitter[1], to switch from a linear to a circular polarized beam, and vice versa, or to simply rotate a linear polarization.

The HWP used for the $\hat{a}$ implementation can be realized properly choosing the length of the crystal. If we cut the it to satisfy the condition $(n_e - n_o)d = \lambda/2$, the output polarization will be rotated of an angle of 2θ.

Some birefringent materials also present the so called Electro-Optical Effect, thanks to which is possible, applying an electrical voltage between the faces perpendicular to the extraordinary axis, to modulate the extraordinary refractive index. Aligning the polarization of the incoming beam to the extraordinary axis ($\theta = 90\,\mathrm{deg}$), the output polarization will not be rotated, but the beam will have acquired a phase of $\Delta\phi = 2\pi\,n_e(V_s)\frac{d}{\lambda}$, where V_s is the amplitude of the modulation voltage.

It is worth noting that, while the influence on the propagation direction of a beam

---

[1]As the one used in the experimental implementation of the $\hat{a}$ operator in Section 2.1.

passing through a birefringence material can be positively used to produce devices like PBS, at the same time, in many experimental situations, it can also create technical problems that must be taken into consideration. The e and o polarization components spatially separate when traveling inside the crystal. Indeed the electric displacement field $\mathbf{D}_e$ and the electric field $\mathbf{E}$ of the e polarization are no more parallel due to the anisotropy of the material and the wavevector $\mathbf{k}_e$, orthogonal to $\mathbf{D}_e$, is deviated respect to the ordinary beam direction of propagation $\mathbf{k}_o$. This phenomenon, called *spatial walk-off*, prevents to use beams waists too small within the crystal to avoid complete geometrical separations of the outgoing beams.

Appendix B

Visibility and Mode Matching Efficiency

The procedures described in Section 2.4.2 to obtain a good mode matching between the signal mode and the Local Oscillator are fundamental for a good Homodyne Detection of the quantum states generated with our setup. To quantify the goodness of our mode matching we can measure the visibility of the interference fringes $(Vis = \frac{I_{max}-I_{min}}{I_{max}+I_{min}})$ produce by the interaction of the LO with the signal at one of the two outputs ports of the Homodyne beam-splitter.

Let's consider, for example, that we want to measure the η_{mm} between the LO and the coherent state used as initial signal state in the experiments described in Section 2.4 and 3.2. Without attenuating this beam we can easily measure the interference fringes using a common power meter. We can indicate with $\alpha_L(\Gamma)$ the profile function of LO and with $\beta_S(\Gamma)$ the one of the coherent state in the signal mode, Γ indicate all the degrees of freedom needed to describe the whole mode profile. The intensity measured

by the power meter is:

$$
\begin{aligned}
I(\alpha,\beta) &= \int d\Gamma \; \langle\alpha_L,\beta_S|\, \hat{a}^\dagger(\Gamma)\hat{a}(\Gamma)\, |\beta_S,\alpha_L\rangle \\
&= \frac{1}{2}\int d\Gamma \; \langle\alpha_L,\beta_S|\left\{\hat{a}_S^\dagger(\Gamma)\hat{a}_S(\Gamma) - i\hat{a}_L^\dagger(\Gamma)\hat{a}_S(\Gamma)+\right. \\
&\quad \left. + i\hat{a}_S^\dagger(\Gamma)\hat{a}_L(\Gamma) + \hat{a}_L^\dagger(\Gamma)\hat{a}_L(\Gamma)\right\}|\beta_S,\alpha_L\rangle \\
&= \frac{1}{2}\int d\Gamma \left\{n_S|\tilde{\beta}_S(\Gamma)|^2 - i\sqrt{n_S n_L}\tilde{\beta}_S(\Gamma)\tilde{\alpha}_L^*(\Gamma)+\right. \\
&\quad \left. + i\sqrt{n_S n_L}\tilde{\beta}_S^*(\Gamma)\tilde{\alpha}_L(\Gamma) + n_L|\tilde{\alpha}_L(\Gamma)|^2\right\} \\
&= \frac{1}{2}\int d\Gamma \left\{n_S|\tilde{\beta}_S(\Gamma)|^2 + n_L|\tilde{\alpha}_L(\Gamma)|^2+\right. \\
&\quad \left. + \sqrt{n_S n_L}|\tilde{\alpha}_L(\Gamma)||\tilde{\beta}_S(\Gamma)|(e^{i(\theta_L-\theta_S+\frac{\pi}{2})} + e^{-i(\theta_L-\theta_S+\frac{\pi}{2})})\right\},
\end{aligned}
\tag{B.1}
$$

where the operator $\hat{a}(\Gamma)$, that describe the field at the output port of the beam-splitter, is linked to the operators $\hat{a}_S(\Gamma)$ and $\hat{a}_L(\Gamma)$, describing the input fields, via the relations (1.47). As for the homodyne description, also in this case we introduced the profiles of the coherent state normalized to 1 ($\tilde{\alpha}(\Gamma)$ and $\tilde{\beta}(\Gamma)$) and their mean photon number nL and n_S. Using Equation (B.1) to calculate the visibility of the interference fringes we have:

$$
Vis(\alpha,\gamma) = \frac{2\sqrt{n_L n_S}}{n_L + n_S}\int d\Gamma \; |\tilde{\alpha}_L(\Gamma)||\tilde{\beta}_S(\Gamma)|.
\tag{B.2}
$$

If we equalize the intensity of the two interacting beam we have that this parameter is exactly equal to the square root mode matching efficiency defined in Section 1.3.2.

$$
\eta_{mm} = \Big[Vis(\alpha,\gamma)\Big]^2
\tag{B.3}
$$

Measuring the mode matching efficiency between the LO and the single photons emitted by the PDC crystal in the signal is an harder task. An additional bright beam, occupying the same mode of the down-converted signal photons, should then be used to check the mode matching instead of them. To produce a bright beam with these characteristics we exploited a three wave mixing process, where a difference frequency wave is generated in the PDC crystal by the injection of the ultraviolet pump with an intense infrared coherent state aligned along the idler direction. If the infrared beam is temporally and spectrally matched with the idler mode, the generated beam[1] is emitted in the signal mode.In the spatial domain a precise coupling between the pump

---

[1]The output of the difference frequency generation process can be considered as a coherent state.

and the field in the idler channel is not necessary and a wider idler seed beam can be used. A formal demonstration can be found in [29] but we can intuitively understand it by imaging that the nonlinear interaction takes place only within the spatial overlap region, i.e. with the narrower pump acting as filter, so a broader size is a sufficient condition to produce a bright signal wave well matched to the selected single photon mode.Now we can use the just describe technique to measure also the mode matching efficiency between the LO and the signal mode of the PDC process.

Appendix C

Coherent States Amplitude Calibration

To calibrate the amplitude of the coherent states used during this thesis we exploit the idea of Klyshko[88], proposed as metrological tool for absolute radiance measurements [89]. He noticed that the measure of the rate of the photons emission in the idler mode of a parametric down conversion process, with and without seeding the signal mode, can be used to obtain an absolute calibration of the amplitude of the seeding states. Indeed, referring to Section 2.2, we have that the spontaneous emission rate of the idler photons (CR_i^{sp}) is proportional to the amplitude of the pump field and to the nonlinear susceptivity coefficient of the BBO crystal. Instead, in the stimulated case, where a coherent state of amplitude $|\alpha|_{PDC}$ is injected in the signal mode, the idler emission rate (CR_i^{st}) is increased by a factor $(1 + |\alpha|_{PDC}^2)$. Thus, we can obtain $|\alpha|_{PDC}$ as:

$$|\alpha|_{PDC}^2 = \frac{CR_i^{st}}{CR_i^{sp}} - 1. \tag{C.1}$$

To measure the idler emission rate we used the SPCM detector placed after the narrow band filters along the idler path as explained in Section 2.2. This scheme is slightly different from the one proposed in [89]. In particular, the presence of the filters gives us a measure of the seed mean photon number $(|\alpha|_{PDC}^2)$ in a mode different from the signal one, given by the convolution between the pump and the seed modes. To take into account this fact and to therefore obtain the mean photon number injected in the signal mode $(|\alpha|_s^2)$ we performed a calibration using a calibrated Power Meter.

We generate the states used as seeds by strongly attenuating a portion of our main laser with a series of attenuation filters. The power meter used for the calibration is not able to measure the low intensity of these quantum states, so we measured the

filters attenuation factor (τ) from the point A to the point B of Figure C.1 using an intense laser beam.
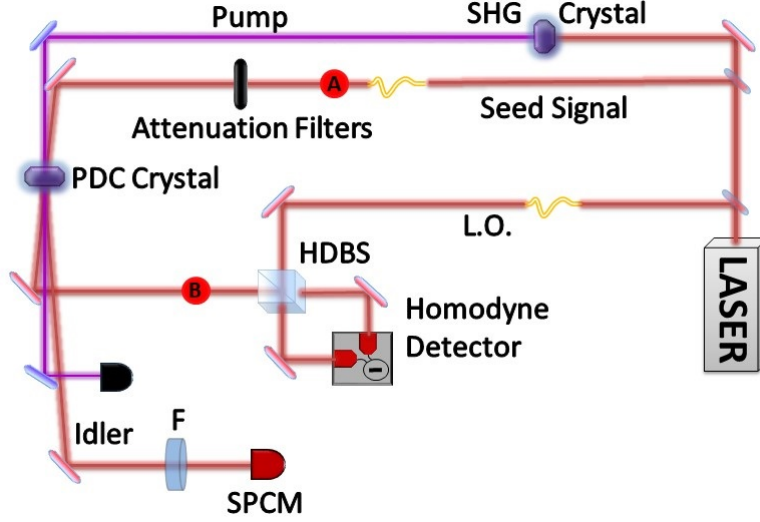

Figure C.1: Schematic view of the setup used for the calibration.

Knowing the attenuation factor allows us to infer the (low) power of the beam just before the HD by measuring the higher power of the initial beam (at the position A). We have to consider now that not all the measured power (P_m) lies in the signal mode due to the non perfect mode matching between the seed and the LO. Estimating the mode matching efficiency with the method described in Appendix B, we have:

$$P_s = (P_m - P_{dark})\tau\eta_{mm}, \tag{C.2}$$

where P_s is the power in the signal mode and P_{dark} is the dark power of our detector. Considering that the central wavelength of our laser (λ) is $780\,nm$, and that it works in a pulsed regime with a repetition rate (R) of $80\,MHz$, we can estimate the amplitude of the coherent states produced in the signal mode as:

$$|\alpha|_s = \sqrt{\frac{P_s\,\lambda}{R\,\hbar\,c}}. \tag{C.3}$$

If, during the alignment procedure before each experiment, we acquire a set of values $\{|\alpha|_s^i, |\alpha|_{PDC}^i\}$ we can obtain the factor of proportionality (m) of the relation

$$|\alpha|_s = m \cdot |\alpha|_{PDC}, \tag{C.4}$$

used to obtain the value of $|\alpha|_s$ by the measure, naturally implemented in our setup, of the ratio between the stimulated and spontaneous idler count rate. As example,
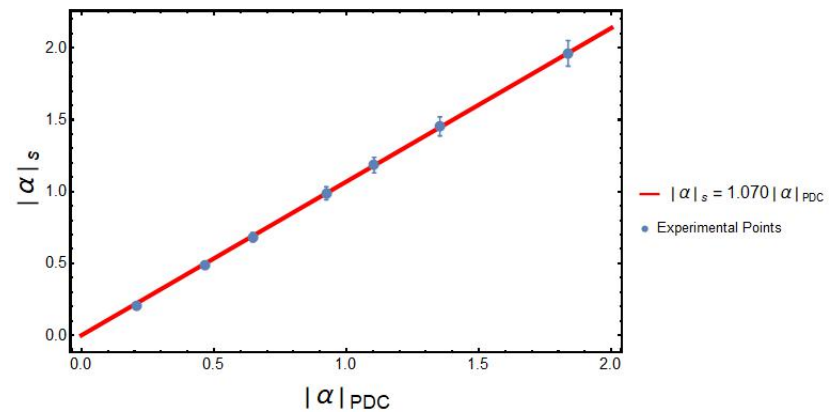
Figure C.2: Results of one run of the calibration just described.

the results of one of these calibrations is shown in Figure C.2. The fact that the experimental points (blue dots in figure) are well reproduced by a linear fit (red line) motivates our choice of the linear model in Equation (C.4).

Appendix D

Trigger Apparatus

For the experiment described in Section 2.4: As explained in Section 2.3, the trigger event that heralds the application of the transformation described in [34], is the coincidence between a "click" from the detectors D_A and D_S of Figure 2.5. They occupy different positions in the setup, so they "click" at different times also if they are triggering operations performed on the same mode. This delay, along with the one due to the difference in the cables and electronic circuits of the two detectors, can be compensated using an electronic delay line. Actually, a third level of trigger is used for this experiment. To reduce the contribution of the dark counts of the two SPCM to the generation efficiency (see Equation (2.33)) we used as trigger the coincidence between the signals produce by D_A and D_S and a signal synchronous with the pulses train emitted by the laser. Such a signal can be obtained by the laser mode-locker. In this way, only the small portion of dark counts that are synchronized with the laser emission affect the η_{gen} parameter.

As final step we have to compensate the delay between the trigger event and the arrival time of the homodyne signal corresponding to the mode on which we perform the Kerr transformation on the oscilloscope. We did this by using a RG8/U cable with length $10.8\,m$ to connect the HD with the oscilloscope, and finely tuning the electronic delay set by this instrument between the trigger event and the start of the acquisition.

For the experiment described in Section 3.2: For this experiment the application of the single photon delocalized addition is heralded by a "click" of the detector D_1 of Figure 3.5. Also in this case we reduced the contribution of the dark counts of the heralding SPCM by using as trigger only the clicks from D_1 that are synchronized with the laser pulses. To do this we make the SPCM clicks coincide with an electronic signal

synchronous with the laser emission. Unlike the previous case, we generate this signal using the DDS. This is advantageous because it ensures more precise delay adjustment.

Appendix E

Calibration of the EOM

Interference Fringe Visibility Technique   We developed a method to calibrate the *EOM* based on the interference of the modulated beam with a reference one. Studying the behavior of the fringe visibility with respect to the variation of the modulation depth, it is possible to retrieve the phase modulation imposed by the *EOM*.

A classical model can be used to explain this technique. The electric field at the output of a pulsed laser can be mathematically expressed like the sum of a large number of plane waves:

$$E_0(t) = \sum_n E_{\omega_0 \pm n\omega_{RR}} \cos[(\omega_0 \pm n\omega_{RR})t + \phi_0], \tag{E.1}$$

the carrier frequency $\frac{\omega_0}{2\pi}$ is the optical frequency determined by the properties of the laser active medium, all the other frequencies are spreaded around ω_0 with a relative distance ω_{RR} fixed by the laser cavity length. If we inject this electric field in an *EOM*, applying a sinusoidal voltage of amplitude V and frequency $\frac{\omega_{mod}}{2\pi}$ to the RF port, we have at its output an electric field of the form:

$$E_{mod}(t) = \sum_n E_{\omega_0 \pm n\omega_{RR}} \cos[(\omega_0 \pm n\omega_{RR})t + s_V \cos(\omega_{mod}t + \phi_{mod})], \tag{E.2}$$

where s_V is the modulation depth dependent on the amplitude of the modulation signal (V) and ϕ_{mod} is its phase respect to the optical pulse train. Interference fringes appear when we mix the modulated beam with a portion of the same laser in a 50:50 beam

splitter. The intensity at one of the output ports of the beam-splitter is:

$$
\begin{aligned}
I_{interf}(t) &= |E_0(t) + E_{mod}(t)|^2 \\
&= \sum_{n,m} \Big(|E_0(t)|^2 + |E_{mod}(t)|^2 + \\
&\quad + E_{\omega_0 \pm n\omega_{RR}} E_{\omega_0 \pm m\omega_{RR}} \{ \underbrace{\cos[2\omega_0 t \pm (n+m)\omega_{RR} t + \phi_0 + s_V \cos(\omega_{mod} t + \phi_{mod})]}_{\text{optical frequencies oscillations mediated to zero by the detector}} + \\
&\quad + \cos[\pm(n-m)\omega_{RR} t + \phi_0 - s_V \cos(\omega_{mod} t + \phi_{mod})] \} \Big).
\end{aligned}
\tag{E.3}
$$

We can measure this intensity with a slow power meter. This has two consequences: we can not see the $2\omega_0$ component, that will be mediated to 0, and also the difference frequency component will be mediated over a number of pulses determined by the bandwidth of the detector. Since we chose $\omega_{mod} = \frac{\omega_{RR}}{4}$, the average has to be done over 4 pulses.

$$
\begin{aligned}
\bar{I}_{interf} &= \frac{1}{4} \sum_{i=0}^{3} \sum_{n,m} \frac{E_{\omega_0 \pm n\omega_{RR}} E_{\omega_0 \pm m\omega_{RR}}}{2} + \frac{E_{\omega_0 \pm n\omega_{RR}} E_{\omega_0 \pm m\omega_{RR}}}{2} + \\
&\quad + E_{\omega_0 \pm n\omega_{RR}} E_{\omega_0 \pm m\omega_{RR}} \{ \cos[\underbrace{\pm(n-m)\omega_{RR} \frac{2\pi}{\omega_{RR}} i}_{\propto 2\pi} + \phi_0 - s_V \cos(\omega_{mod} \frac{2\pi}{\omega_{RR}} i + \phi_{mod})] \} \\
&= \sum_{n,m} E_{\omega_0 \pm n\omega_{RR}} E_{\omega_0 \pm m\omega_{RR}} \{ 1 + \frac{1}{2} \cos(\phi_0) \big(\cos[s_V \cos(\phi_{mod})] + \cos[s_V \sin(\phi_{mod})] \big) \}.
\end{aligned}
\tag{E.4}
$$

We can scan the relative phase between the reference signal an the Local Oscillator (ϕ_0) using a piezo. Measuring the maximum and the minimum of $\bar{I}_{interf}$ for various modulation depths (s_V) we can study the relation between the fringes visibility ($Vis = \frac{I_{max} - I_{min}}{I_{max} + I_{min}}$) and this parameter. From the calculation done before we find:

$$
Vis[s_V, \phi_{mod}] = \frac{1}{2} | \cos[s_V \cos(\phi_{mod})] + \cos[s_V \sin(\phi_{mod})] |.
\tag{E.5}
$$

Figure E.1 reports the behavior of the visibility varying the parameter s_V, for some values of the phase ϕ_{mod}.

The shape of these curves changes a lot with respect to this phase. We can scan ϕ_{mod} using the DDS to reduce the visibility curve to a pure cosine function, in order to set the condition $\phi_{mod} = 0$. To control the modulation depth s_V we use a voltage controlled amplifier placed between the DDS and the EOM. In this way we can gradually change the amplitude of the driving signal V varying the DC voltage applied to the amplifier
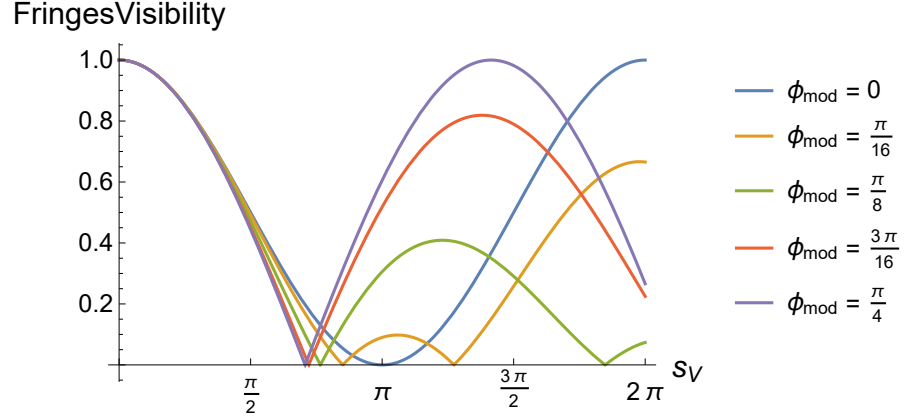
Figure E.1: Visibility v.s. Modulation depth for various phase delays (ϕ_{mod}) between the pulses train and the driving signal.

($V_{control}$). Now we have to find the relation connecting s_V to the control voltage. To do so, we fit the measured visibility with Equation (E.5), replacing s_V with a polynomial function of $V_{control}$:

$$s(V_{control}) = a + b \cdot V_{control} + c \cdot V_{control}^2 + d \cdot V_{control}^3 + e \cdot V_{control}^4, \qquad (E.6)$$

after setting the condition $\phi_{mod} = 0$ as explained before. In Figure E.2 I show the results of the calibration used in the experiment.
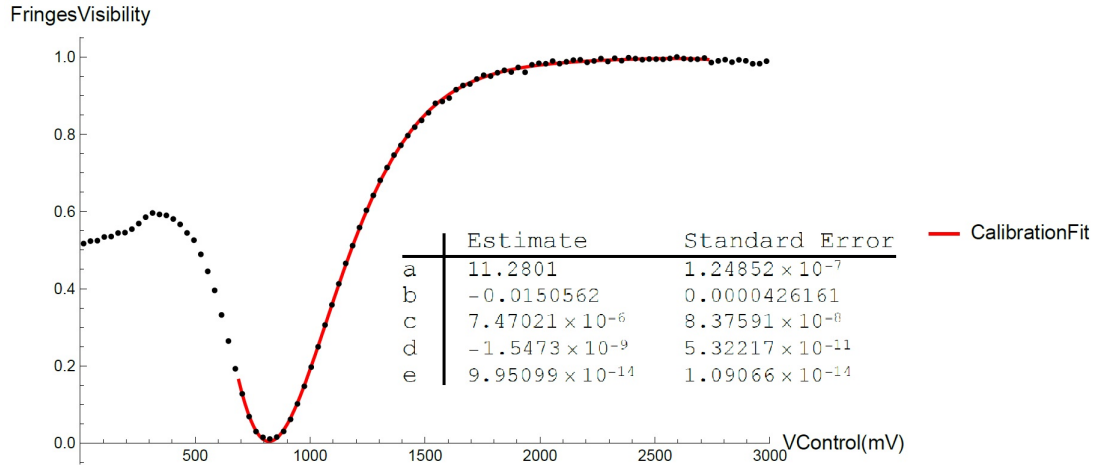

Figure E.2: Experimental visibility data obtained scanning the modulation depth, after we have set $\phi_{mod} = 0$. The red line is the fit with Eq. (E.5), using the polinomial expression of Eq. (E.6).

The relative phase between the two LO pulses corresponding to the signal temporal

modes A and B can be calculated as:

$$\theta^{LO}_{rel} = s - s\cos\left(\omega_{mod}\, 2\, T_p\right) = s - s\cos\left(\frac{\omega_{RR}}{4}\, 2\, \frac{2\pi}{\omega_{RR}}\right) = 2s. \tag{E.7}$$

Combining this result with Equation (E.5) we can obtain that the condition of zero visibility corresponds to a 2π phase shift between the first and the third pulse.

Validation of the Interference Fringe Visibility Technique To validate our method, we performed an *EOM* calibration using a standard technique that involves the use of an optical cavity. Applying a sinusoidal modulation of the phase of an optical beam will result in a modification of its frequency spectrum. As the amplitude of the RF signal increases a series of side bands appears on the top of a laser spectral profile. The behavior of the side bands can be used to calibrate the modulator.

Let's say, for example, we send a monochromatic laser in the EOM. Applying a sinusoidal phase modulation of amplitude s and frequency $\frac{\omega_{mod}}{2\pi}$, we have at the output of the modulator an electrical field of the form:

$$E_{mod}(t) = A\cos[\omega_0 t + s\cos(\omega_{mod}t)]. \tag{E.8}$$

If we measure the spectrum of this signal, changing the modulation depth s, it's possible to observe the uprising of the side bands. Each new frequency line is symmetrically spread around the fundamental with a separation equal to the frequency of the modulation signal $\left(\frac{\omega_{mod}}{2\pi}\right)$. The energy of the optical signal is redistributed among the side bands as shown in Figure E.3.
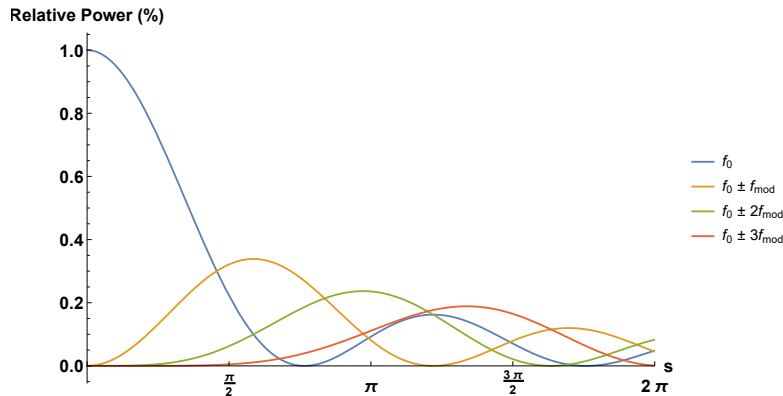

Figure E.3: Power of the first three side bands as function of the modulation depth.

Measuring the values of s at witch different side bands have the same power, it is possible to retrieve the relation connecting the amplitude of the modulation signal to

the induced phase shift. One of the easiest way to measure the spectrum of an optical signal involves the use of a Fabry-Pérot cavity as shown in Figure E.4.
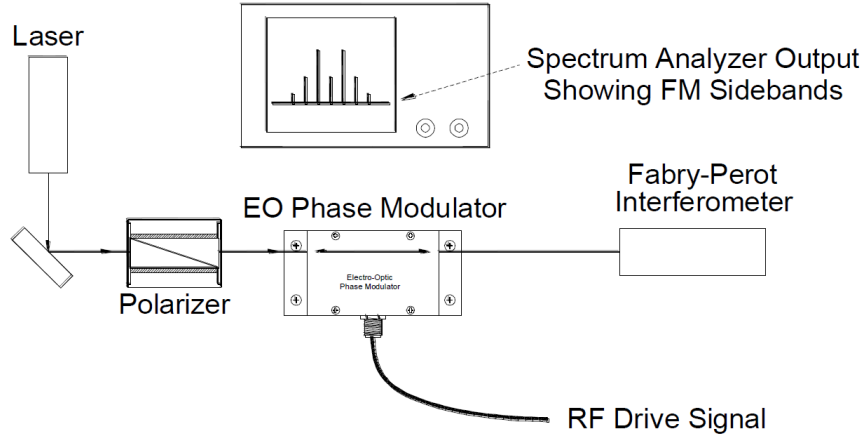

Figure E.4: Typical setup for the Phase Modulator calibration.

This setup is easy to use for CW lasers. Let's say for example we want to modulate the phase of the laser beam with a signal of frequency $20MHz$. To distinguish two consecutive sidebands, in order to measure their amplitude, we need the distance between them to be greater than the full width at half maximum ($FWHM$) of the resonance peaks of the cavity ($FWHM < 20\,MHz$). For this example a cavity with a $FWHM$ of $5\,MHz$ could be good. We can obtain this value using a Fabry-Pérot cavity $10\,cm$ long, with a *Finesse* ($F = \frac{FSR}{FWHM}$) of 300 [90], that it is not difficult to build and use. FSR is the *Free Spectral Range* of the cavity, the distance between two consecutive peaks, fixed by its length ($FSR = \frac{c}{2L}$).

As many times mentioned, in our lab we work with a mode-locked laser emitting $1.5\,ps$ long pulses with a repetition rate of $80\,MHz$. This fact drastically changes the situation compared to the previous example. First of all the energy of the modulated signal is redistributed among the sidebands in a different way respect to the CW case. The spectrum of our unmodulated laser is a frequency comb consisting of a series of spectral lines separated by $80\,MHz$, centered at the optical frequency of the laser. Looking at one of these lines, slowly increasing the modulation depth, we can first see two sidebands appearing to the left and to the right of it, $20\,MHz$ away from the central line (f_{mod}). Going further, increasing the amplitude of the modulation signal, two new sidebands will appear, $40\,MHz$ ($\pm 2f_{mod}$) away from each main peak. The left sideband ($-2f_{mod}$) of one of the laser lines will be superimposed to the right one ($+2f_{mod}$) of the previous line. Increasing even more the modulation depth also the

$\pm 3 f_{mod}$ sidebands will appear, but they won't be distinguishable from the first one ($\pm f_{mod}$). Their distance from an unmodulated peak will be equal to the distance of the first side bands $\pm f_{mod}$ grown around the next one. The resulting sidebands behavior is illustrated in Figure E.5.
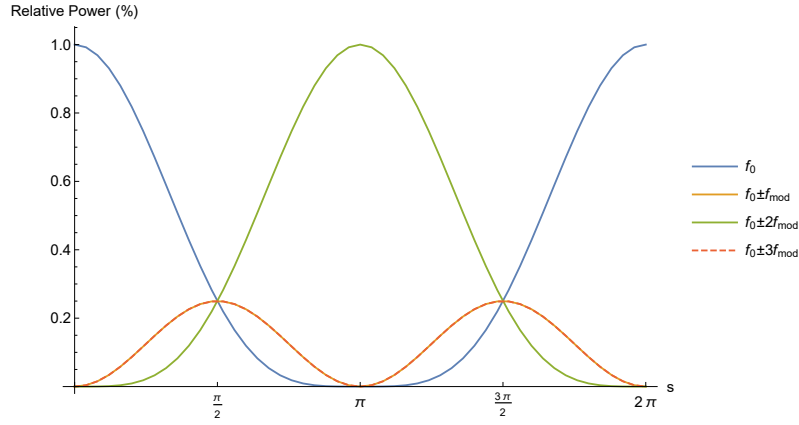

Figure E.5: Power of the first three side bands as function of the modulation depth for the pulsed laser case.

To observe these features we have to built a resonant cavity with a Finesse of $\frac{FSR}{FWHM} \approx \frac{80MHz}{5MHz} \approx 16$, smaller than the CW case. To obtain this result I imposed that the FSR of the cavity is equal to the FSR of our laser. This is a necessary condition that must be satisfied to reach the resonance condition for a pulsed laser in a cavity [90]. From a practical point of view, this means that we need a $3.7\,m$ long cavity. Dealing with a cavity like this is not easy, it requires frequent alignments, and the overall procedure for the EOM calibration is difficult to be automatized. From this point of view the technique explained in the previous section is faster and easier to implement. In Figure E.6 I report the results of the EOM calibration made with the resonance cavity.

The solid lines represent the theoretical behavior of Figure E.5. The colored dots represent the measured amplitudes of the first tree sidebands. We obtained these data varying the voltage applied to the voltage controlled amplifier ($V_{control}$). For the experimental data points the conversion of the x-axis of Figure E.6, from $V_{control}$ to radiant, was done using the calibration of Figure E.2. The excellent agreement between the experimental data and the theoretical curves is a proof of the validity of our method.
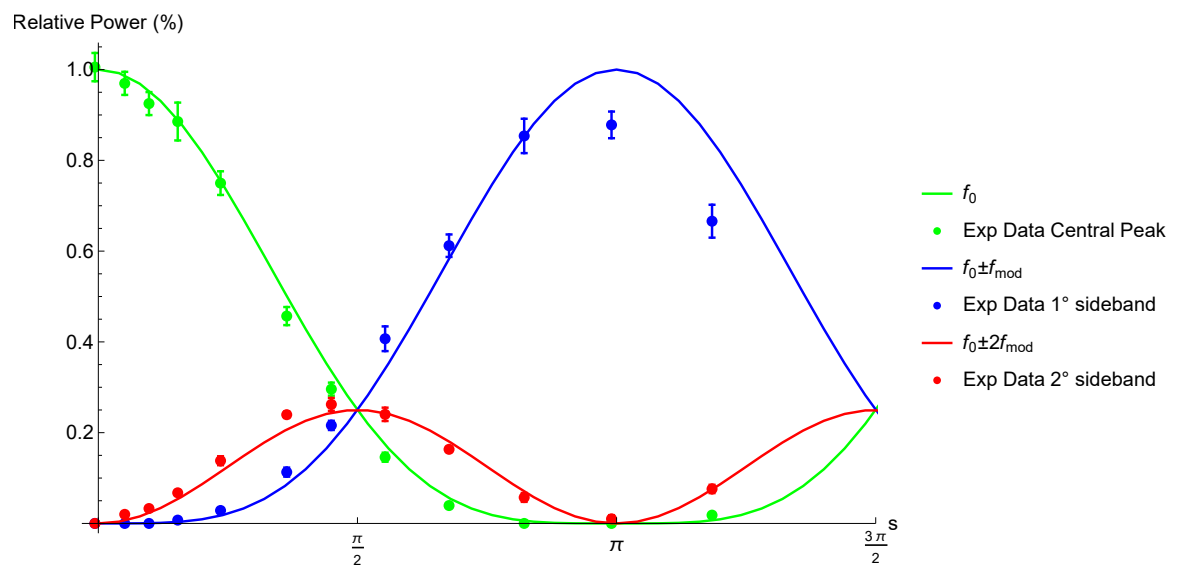
Figure E.6: Measured (dots) and theoretical (lines) behavior of the side bands produced on our laser spectrum by the EOM.

Bibliography

[1] Rodney Loudon. *The Quantum Theory of Light*. Oxford University Press, third edition.

[2] Bellini Marco and Zavatta Alessandro. *Manipulating light states by single-photon addition and subtraction*, volume 55. Elsevier B.V., 2010.

[3] M. S. Kim. Recent developments in photon-level operations on travelling light fields. *Journal of Physics B: Atomic, Molecular and Optical Physics*, 41(13), 2008.

[4] Alessandro Zavatta, Silvia Viciani, and Marco Bellini. Single-photon excitation of a coherent state: Catching the elementary step of stimulated light emission. *Physical Review A - Atomic, Molecular, and Optical Physics*, 72(2):1–9, 2005.

[5] Valentina Parigi, Alessandro Zavatta, Myungshik Kim, and Marco Bellini. Probing quantum commutation rules by addition and subtraction of single photons to/from a light field. *Science (New York, N.Y.)*, 317(5846):1890–1893, 2007.

[6] J. J. Sakurai. *Modern Quantum Mechanics*. Addison-Welsey Publishing Company, 1994.

[7] Adrien Dousse, Jan Suffczyński, Alexios Beveratos, Olivier Krebs, Aristide Lemaître, Isabelle Sagnes, Jacqueline Bloch, Paul Voisin, and Pascale Senellart. Ultrabright source of entangled photon pairs. *Nature*, 466(7303):217–220, 2010.

[8] Pascale Senellart, Glenn Solomon, and Andrew White. High-performance semiconductor quantum-dot single-photon sources. *Nature Nanotechnology*, 12(11):1026–1039, 2017.

[9] Pau Farrera, Georg Heinze, Boris Albrecht, Melvyn Ho, Matías Chávez, Colin Teo, Nicolas Sangouard, and Hugues De Riedmatten. Generation of single photons with

highly tunable wave shape from a cold atomic ensemble. *Nature Communications*, 7(May), 2016.

[10] D. B. Higginbottom, L. Slodička, G. Araneda, L. Lachman, R. Filip, M. Hennrich, and R. Blatt. Pure single photons from a trapped atom source. *New Journal of Physics*, 18(9), 2016.

[11] J. Hwang and E. A. Hinds. Dye molecules as single-photon sources and large optical nonlinearities on a chip. *New Journal of Physics*, 13, 2011.

[12] B. Lounis and W E Moerner. Single Photons on Demand from a Singlemolecule at Room Temperature. *Nature*, 407:491–493, 2000.

[13] Shen Li, Cui Hong Li, Bo Wen Zhao, Yang Dong, Cong Cong Li, Xiang Dong Chen, Ya Song Ge, and Fang Wen Sun. A Bright Single-Photon Source from Nitrogen-Vacancy Centers in Diamond Nanowires. *Chinese Physics Letters*, 34(9), 2017.

[14] Beatrice Rodiek, Marco Lopez, Helmuth Hofer, Geiland Porrovecchio, Marek Smid, Xiao-Liu Chu, Stephan Gotzinger, Vahid Sandoghdar, Sarah Lindner, Christoph Becher, and Stefan Kuck. Experimental realization of an absolute single-photon source based on a single nitrogen vacancy center in a nanodiamond. *Optica*, 4(1):71, 2017.

[15] Mark Fox. *Quantum Optics*, volume 1. 2015.

[16] Paul N Butcher and David Cotter. *The Elements of Nonlinear Optics*. Cambridge University Press, 1990.

[17] Roy J. Glauber. Coherent and incoherent states of the radiation field. *Physical Review*, 131(6):2766–2788, 1963.

[18] Howard M. Wiseman. *Quantum Measurement and Control*. Cambridge University Press, 2010.

[19] Alessandro Ferraro, Stefano Olivares, and Matteo G A Paris. *Gaussian states in continuous variable quantum information*. 2005.

[20] G. M. D'Ariano. Tomographic measurement of the density matrix of the radiation field. *Quantum Semiclass. Opt*, 7:693, 1995.

[21] Jürgen Appel, Dallas Hoffman, Eden Figueroa, and A. I. Lvovsky. Electronic noise in optical homodyne tomography. *Physical Review A - Atomic, Molecular, and Optical Physics*, 75(3):1–4, 2007.

[22] Z Hradil, J Summhammer, and H Rauch. Quantum tomography as normalization of incompatible observations. *Physics Letters A*, 261:20–24, 1999.

[23] A I Lvovsky. Iterative maximum-likelihood reconstruction in quantum homodyne tomography. *J. Opt. B: Quantum Semiclass. Opt*, 6:556–559, 2004.

[24] Alexei Ourjoumtsev, Rosa Tualle-Brouri, Julien Laurat, and Philippe Grangier. Generating optical Schrödinger kittens for quantum information processing. *Science*, 312(5770):83–86, 2006.

[25] Seyed Mohammad Hashemi Rafsanjani, Mohammad Mirhosseini, Omar S. Magana-Loaiza, Bryan T. Gard, Richard Birrittella, B. E. Koltenbah, C. G. Parazzoli, Barbara A. Capron, Christopher C. Gerry, Jonathan P. Dowling, and Robert W. Boyd. Interferometry with Photon-Subtracted Thermal Light. (1):1–8, 2016.

[26] Mihai D. Vidrighin, Oscar Dahlsten, Marco Barbieri, M. S. Kim, Vlatko Vedral, and Ian A. Walmsley. Photonic Maxwell's Demon. *Physical Review Letters*, 116(5):1–7, 2016.

[27] A. Zavatta, V. Parigi, M. S. Kim, and M. Bellini. Subtracting photons from arbitrary light fields: Experimental test of coherent state invariance by single-photon annihilation. *New Journal of Physics*, 10, 2008.

[28] Z.Y. Ou. Parametric down-conversion with coherent pulse pumping and quantum interference between independent fields. *Quantum and Semiclassical Optics : Journal of the European Optical Society Part B*, 9:599–614, 1997.

[29] T. Aichele, a. I. Lvovsky, and S. Schiller. Optical mode characterization of single photons prepared by means of conditional measurements on a biphoton state. *European Physical Journal D*, 18(2):237–245, 2002.

[30] Robert W. Boyd. *Nonlinear Optics*. Academic Press, third edition, 2008.

[31] V. Y. Shur, E. V. Pelegova, A. R. Akhmatkhanov, and I. S. Baturin. Periodically poled crystals of KTP family: A review. *Ferroelectrics*, 496(1):49–69, 2016.

[32] Marco Fiorentino, Sean M. Spillane, Raymond G. Beausoleil, Tony D. Roberts, Philip Battle, and Mark W. Munro. Spontaneous parametric down-conversion in periodically poled KTP waveguides and bulk crystals. *Optics Express*, 15(12):7479, 2007.

[33] Erwin Schrödinger. The Present Situation in Quantum Mechanics, 1935.

[34] Luca S. Costanzo, Antonio S. Coelho, Nicola Biagi, Jaromír Fiurášek, Marco Bellini, and Alessandro Zavatta. Measurement-Induced Strong Kerr Nonlinearity for Weak Quantum States of Light. *Physical Review Letters*, 119(1):1–6, 2017.

[35] S. Glancy, J. M. LoSecco, and C. E. Tanner. Implementation of a quantum phase gate by the optical Kerr effect. *https://arxiv.org/pdf/quant-ph/0009110.pdf*, pages 1–9, 2000.

[36] Hiroo Azuma. Quantum computation with Kerr-nonlinear photonic crystals. *https://arxiv.org/pdf/quant-ph/0604086.pdf*, (2):1–21, 2018.

[37] Julio Gea-Banacloche. Impossibility of large phase shifts via the giant Kerr effect with single-photon wave packets. *PHYSICAL REVIEW A*, 043823, 2010.

[38] Jeffrey H Shapiro. Single-photon Kerr nonlinearities do not help quantum computation. *PHYSICAL REVIEW A*, 062305, 2006.

[39] H Gorniaczyk, C Tresp, P Bienias, W Li, I Mirgorodskiy, H P Bu, I Lesanovsky, and S Hofferberth. Enhancement of Rydberg-mediated single-photon nonlinearities by electrically tuned Forster resonances. *NATURE COMMUNICATIONS*, 7:12480, 2016.

[40] Sumanta Das, Andrey Grankin, Ivan Iakoupov, Etienne Brion, Johannes Borregaard, Rajiv Boddeda, Imam Usmani, Alexei Ourjoumtsev, Philippe Grangier, and Anders S Sørensen. Photonic controlled- PHASE gates through Rydberg blockade in optical cavities. *PHYSICAL REVIEW A*, 040303(R):1–6, 2016.

[41] E Knill, R La, and G J Milburn. A scheme for efficient quantum computation with linear optics. *Nature*, 409(January):46–52, 2001.

[42] J D Franson, M M Donegan, M J Fitch, B C Jacobs, and T B Pittman. High-Fidelity Quantum Logic Operations Using Linear Optical Elements. *Physical Review Letters*, 89:1–4, 2002.

[43] A. Zavatta, J. Fiurásek, and M. Bellini. A high-fidelity noiseless amplifier for quantum light states. *Nature Photonics*, 5(November 2010):5, 2010.

[44] Michael A. Nielsen and Isaac L. Chuang. *Quantum Computaion and Quantum Information*. Cambridge University Press, 10th anniv edition, 2010.

[45] B. Yurke and D. Stoler. Generating quantum mechanical superpositions of macroscopically distinguishable states via amplitude dispersion. *Physical Review Letters*, 57(1):13–16, 1986.

[46] G. J. Milburn. Quantum optical Fredkin gate. *Physical Review Letters*, 62(18):2124–2127, 1989.

[47] M. G.A. Paris, M. B. Plenio, S. Bose, D. Jonathan, and G. M. D'Ariano. Optical Bell measurement by Fock filtering. *Physics Letters, Section A: General, Atomic and Solid State Physics*, 273(3):153–158, 2000.

[48] Jaromír Fiurášek. Engineering quantum operations on traveling light beams by multiple photon addition and subtraction. *Physical Review A - Atomic, Molecular, and Optical Physics*, 80(5):1–7, 2009.

[49] M. Mičuda, I. Straka, M. Miková, M. Dušek, N. J. Cerf, J. Fiurášek, and M. Ježek. Noiseless loss suppression in quantum optical communication. *Physical Review Letters*, 109(18):1–5, 2012.

[50] C. N. Gagatsos, J. Fiurášek, A. Zavatta, M. Bellini, and N. J. Cerf. Heralded noiseless amplification and attenuation of non-Gaussian states of light. *Physical Review A - Atomic, Molecular, and Optical Physics*, 89(6):1–8, 2014.

[51] Ryszard Horodecki, Paweł Horodecki, Michał Horodecki, and Karol Horodecki. Quantum entanglement. *Reviews of Modern Physics*, 81(2):865–942, 2009.

[52] Reinhard F Werner. Quantum states with EPR correlations admitting a hidden-variable model. *Phys*, 40(8):4277–4281, 1989.

[53] Albert Einstein, Noah S. Podolefsky, and N. Rosen. Can Quantum-Mechanical Description of Physical Reality Be Considered Complete? *Physical Review*, 47, 1935.

[54] J. S. Bell. On the Einstein Podolsky Rosen Paradox. *Physics*, 1(3):195–200, 1964.

[55] Alain Aspect, Philippe Grangier, and Gérard Roger. Experimental tests of realistic local theories via Bell's theorem. *Physical Review Letters*, 47(7):460–463, 1981.

[56] Alain Aspect, Jean Dalibard, and Gerard Roger. Experimental Test of Bell's Inequalities Using Time-Varying Analyzers. *Physical Review Letters*, 49(25), 1982.

[57] Z. Y. Ou and L. Mandel. Violation of Bell's Inequality and Classical Probability in a Two-Photon Correlation Experiment. *Phys. Rev. Lett.*, 61(1), 1988.

[58] Fabio Antonio Bovino, Giuseppe Castagnoli, Artur Ekert, Paweł Horodecki, Carolina Moura Alves, and Alexander Vladimir Sergienko. Direct Measurement of Nonlinear Properties of Bipartite Quantum States. *Physical Review Letters*, 240407(December), 2005.

[59] Paul G Kwiat, Klaus Mattle, Weinfurter Harald, and Anton Zeilinger. New High-Intensity Source of Polarization-Entangled Photon Pairs. *Physical Review Letters*, 75(24), 1995.

[60] Charles H Bennett and Gilles Brassard. Quantum cryptography : Public key distribution and coin tossing. *Theoretical Computer Science*, 560:7–11, 2014.

[61] Sheng-kai Liao, Wen-qi Cai, Wei-yue Liu, Liang Zhang, Yang Li, Ji-gang Ren, Juan Yin, Qi Shen, Yuan Cao, Zheng-ping Li, Feng-zhi Li, Xia-wei Chen, Li-hua Sun, Jian-jun Jia, Jin-cai Wu, Xiao-jun Jiang, Jian-feng Wang, Yong-mei Huang, Qiang Wang, Yi-lin Zhou, Lei Deng, Tao Xi, Lu Ma, Tai Hu, Qiang Zhang, Yu-ao Chen, Nai-le Liu, Xiang-bin Wang, Zhen-cai Zhu, Chao-yang Lu, Rong Shu, Cheng-zhi Peng, Jian-yu Wang, and Jian-wei Pan. Satellite-to-ground quantum key distribution. *Nature*, 549, 2017.

[62] Charles H Bennett and Stephen J Wiesner. Communication via One- and Two-Particle Operators on Einstein-Podolsky-Rosen States. *Physical Review Letters*, 69(20), 1992.

[63] Charles H Bennett, Gilles Brassard, Claude Crepeau, Richard Jozsa, Asher Peres, and William K Wootters. Teleporting an Unknown Quantum State via Dual Classical and Einstein-Podolsky-Rosen Channels. *Phys. Rev. Lett.*, 70(13), 1993.

[64] Asher Peres. Separability Criterion for Density Matrices. *Phys. Rev. Lett.*, 77, 1996.

[65] Michal Horodecki, Pawel Horodecki, and Ryszard Horodecki. Separability of mixed states: necessary and sufficient conditions. *Physics Letters A*, 9601(96), 1996.

[66] S. J. Van Enk. Single-particle entanglement. *Physical Review A - Atomic, Molecular, and Optical Physics*, 72(6):1–3, 2005.

[67] S. J. Van Enk. Reply to "comment on 'single-particle entanglement'". *Physical Review A - Atomic, Molecular, and Optical Physics*, 74(2):1–3, 2006.

[68] Aurélien Drezet. Comment on "single-particle entanglement". *Physical Review A - Atomic, Molecular, and Optical Physics*, 74(2):2005–2006, 2006.

[69] Charles H. Bennett, Gilles Brassard, Sandu Popescu, Benjamin Schumacher, John a. Smolin, and William K. Wootters. Purification of noisy entanglement and faithful teleportation via noisy channels. *Phys. Rev. Lett.*, 76(5), 1996.

[70] O. Morin, V. D'Auria, C. Fabre, J. Laurat, J. D. Bancal, M. Ho, P. Sekatski, N. Gisin, and N. Sangouard. Witnessing trustworthy single-photon entanglement with local homodyne measurements. *Phys. Rev. Lett.*, (1):1–6, 2013.

[71] S. Giacomini, F. Sciarrino, E. Lombardi, and F. De Martini. Active teleportation of a quantum bit. *Physical Review A - Atomic, Molecular, and Optical Physics*, 66(3):4, 2002.

[72] Hyunseok Jeong, Alessandro Zavatta, Minsu Kang, Seung-woo Lee, Luca S Costanzo, Samuele Grandi, Timothy C Ralph, and Marco Bellini. Generation of hybrid entanglement of light. *Nature Photonics*, 8:564–569, 2014.

[73] Alessandro Zavatta, Silvia Viciani, and Marco Bellini. Quantum-to-classical transition with single-photon-added coherent states of light. *Science*, 306(5696):660–662, 2004.

[74] Evan Meyer-Scott, Johannes Tiedau, Georg Harder, Lynden K. Shalm, and Tim J. Bartley. Discorrelated quantum states. *Nature Scientific Reports*, (December 2016):1–7, 2016.

[75] Alessandro Zavatta, Milena D'Angelo, Valentina Parigi, and Marco Bellini. Remote preparation of arbitrary time-encoded single-photon ebits. *Physical Review Letters*, 96(2):1–4, 2006.

[76] M. R. Dietrich and B. B. Blinov. Use of a Microcontroller for Fast Feedback Control of a Fiber Laser. pages 1–3, 2009.

[77] Jaroslav Řeháček, Zdeněk Hradil, E. Knill, and A. I. Lvovsky. Diluted maximum-likelihood algorithm for quantum tomography. *Physical Review A - Atomic, Molecular, and Optical Physics*, 75(4):1–5, 2007.

[78] Thorlabs. EO-PM-NR-Cx Electro-Optic Phase Modulator Operating Manual, 2012.

[79] Analog Devices. AD9959, 4-Channel, 500 MSPS DDS with 10-Bit DACs, 2008.

[80] Pavel Sekatski, Nicolas Sangouard, Magdalena Stobińska, Félix Bussières, Mikael Afzelius, and Nicolas Gisin. Proposal for exploring macroscopic entanglement with a single photon and coherent states. *Physical Review A - Atomic, Molecular, and Optical Physics*, 86(6):1–5, 2012.

[81] N. Bruno, A. Martin, P. Sekatski, N. Sangouard, R. T. Thew, and N. Gisin. Displacement of entanglement back and forth between the micro and macro domains. *Nature Physics*, 9(9):545–548, 2013.

[82] Barbara M. Terhal. A family of indecomposable positive linear maps based on entangled quantum states. *Linear Algebra and Its Applications*, 323(1-3):61–73, 2001.

[83] Fernando G.S.L. Brandão and Reinaldo O. Vianna. Separable multipartite mixed states: Operational asymptotically necessary and sufficient conditions. *Physical Review Letters*, 93(22):1–4, 2004.

[84] Ruben Quesada and Anna Sanpera. Best separable approximation of multipartite diagonal symmetric states. *Physical Review A - Atomic, Molecular, and Optical Physics*, 89(5):1–7, 2014.

[85] Andrew C. Doherty, Pablo A. Parrilo, and Federico M. Spedalieri. Complete family of separability criteria. *Physical Review A - Atomic, Molecular, and Optical Physics*, 69(2):20, 2004.

[86] Nicola Biagi, Luca S Costanzo, Marco Bellini, and Alessandro Zavatta. Entangling macroscopic light states by delocalized photon addition. *https://arxiv.org/pdf/1811.10466.pdf*, 2(1):1–5, 2018.

[87] Marco Bellini, Nicola Biagi, Luca Salvatore Costanzo, and Alessandro Zavatta. Quantum Light State Engineering and Entanglement Generation by Multimode Photon Addition. *2018 IEEE Photonics Society Summer Topical Meeting Series (SUM)*, pages 197–198, 2018.

[88] D N Klyshko. Use of two-photon light for absolute calibration of photoelectric detectors. *Soviet Journal of Quantum Electronics*, 10(9):1112–1117, 1980.

[89] Alan Migdall. Correlated-photon metrology without absolute standards. *Physics Today*, 52(1):41–46, 1999.

[90] W. Demtroder. *Laser Spectroscopy - Basic Concepts and Instrumentation.* Springer, 2003.